



National Technical University of Athens
School of Civil Engineering
Laboratory of Earthquake Engineering

VULNERABILITY OF RC SHEAR WALL STRUCTURES UNDER NEAR FIELD SEISMIC LOADING

A Postgraduate Thesis By
Khalil Mostafa
Ghanem Mostafa

(Analysis and Design of Earthquake Resistant Structures) **ADERS** Program

Under the supervision of
Prof. M. Fragiadakis,
Dr. Taflampas Ioannis

Submitted in partial fulfillment of the requirements
For the degree of Master of Science in structural Engineering
March 2018



The undersigned have examined the thesis entitled “vulnerability of RC shear wall structures under near field seismic loading” presented by **Khalil Mostafa and Ghanem Mostafa**, two candidates for the degree of **Master degree of Science in structural Engineering** and hereby certify that it is worthy of acceptance.



Table of Contents

ABSTRACT	1
CHAPTER 1 INTRODUCTION	2
CHAPTER 2 NEAR-FAULT GROUND MOTIONS	4
2.1. Statement of Problem	4
2.2. Near-Fault effects	5
2.3. Directional effects	7
2.4. Parameterization of Near-Fault Ground Motion	9
2.5. Pulse characteristics	12
2.6. Effect of the pulse on the acceleration response spectrum	13
CHAPTER 3 BUILDING DESCRIPTION	15
3.1. Building Layout	15
3.2. Modelling of the building using Seismostruct:	17
3.3. Materials:	19
3.3.1. Concrete	19
3.3.2. Steel Reinforcement	19
3.4. Modeling Elements	20
3.4.1. Beams	20
3.4.2. Columns	21
3.4.3. Walls	21
3.5. Loading	22
3.6. Seismic Characteristics :	24
3.7. Eigenvalues Analysis	24
3.8. Static Pushover Analysis	26
3.8.1. Theory and purpose	26
3.8.2. Static pushover in seismostruct	26
CHAPTER 4 GROUND MOTIONS RECORDS	31
4.1. L'Aquila earthquake 2009:	31
4.2. Norcia earthquake 2016:	35
CHAPTER 5 SEISMIC DESIGN OF RC SHEAR WALL STRUCTURES IN CHILE	42
5.1. Introduction	42
5.2. Building code provisions in Chile	43
5.3. Typical Construction Method and Assumptions	45
5.4. Implementation of Chilean code assumptions in the case study	49
5.4.1. Strengthened building layout	50
5.4.2. Eigen value analysis	50



5.4.3. Pushover analysis	52
CHAPTER 6 DATA ANALYSIS AND RESULTS	53
6.1. Identification of damage limit states for RC buildings	53
6.2. Methodology	54
6.3. Dynamic time history Results for the original building	55
6.3.1. Aquila earthquake in X-Direction	55
6.3.2. Norcia earthquake in X-Direction	63
6.3.3. Aquila earthquake in Y-direction	71
6.3.4. Norcia earthquake in Y-Direction	79
6.4. Dynamic time history results of strengthened building	87
6.4.1. Aquila Earthquake in Y-Direction	87
6.4.2. Norcia Earthquake in Y-Direction	95
CHAPTER 7 SUMMARY AND CONCLUSIONS	103
7.1. Summary	103
7.2. Conclusions	107
REFERENCES	114



ABSTRACT

In this paper the seismic risk of an eight storey reinforced concrete building in Athens is investigated.

The structure is exposed to a near field ground motions from Italian Aquila and Norcia earthquakes, due to the similarity in the geotectonic environment between Greece and Italy.

The purpose of this investigation is to estimate the damage occurred to the building and the effect of the seismological parameters such as, moment magnitude, forward directivity, acceleration time history density and amplitude.

As a first step, a sample of 16 near fault ground motion records from Aquila and Norcia earthquakes in Italy is exposed to the building, to obtain the displacement time history of each record, which will be used to determine the damage limit states achieved according to “T. Rossetto, A. Elnashai” vulnerability relationships.

Then suggesting a solution to improve the seismic response of the building, and an appropriate solution is found and applied according to the new Chilean seismic code provisions which states that typical buildings include a large number of shear walls, with ratios of wall cross-sectional area to floor plan area of roughly 3% in each principal direction, with light reinforcement.

After implementing the Chilean code provisions and investigating the building in Y-direction only, the results have shown a significant improvement in the building response and a reduction in the damage limit states reached for most of the records.

After reviewing all the results, it was found that the moment magnitude value isn't the predominant affecting factor, and the acceleration time history density is more effective in the damage caused by the near field records.

Eventually, it is concluded that estimation of damage intensity is mostly affected by the energy contained in the ground motion which is introduced as the “energy flux” index.



CHAPTER 1 INTRODUCTION

Near-field ground motions have caused much damage in the vicinity of seismic sources during recent earthquakes.

It is found that ground shaking near a fault rupture is characterized by a short-duration impulsive motion which is clearly obvious in the velocity time history record. This impulsive motion exposes the structure to high input energy at the beginning of the record unlike what happens in ground shakings far from the fault rupture.

In the near-fault region, which is usually assumed to extend about 20 to 60 km from the seismic source, the short travel distance of the seismic waves does not allow enough time for the high frequency content to be damped out of the record as is normally observed in far field records.

The effect of this pulse type motion on the response is important in the design of structures for near-fault events.

This phenomenon requires consideration in the design process for structures that are located in the near-field region, unfortunately the seismic design codes are based on “far-fault” ground motion data only without taking into consideration the characteristics of the near fault ground motion therefore the design of structures for near-fault events is inappropriate according to the seismic design code provisions, except for the American seismic design code “ASCE” which recently this phenomenon is taken into consideration.

In this study the effect of near-fault ground motions are investigated, along with other seismological parameters such as earthquake magnitude and distance from the fault, to evaluate the seismic response of an eight-story RC combined structural system building (MRF and Shear walls), and perform a damage assessment for that building under certain earthquake events.

Furthermore, suggesting appropriate solution to mitigate the damage reached in practically applicable and economic approach.

Using Seismostruct software, a static non-linear pushover analysis is performed, in order to calculate the yield acceleration of the building (a_y) which is used later in picking up the suitable ground motion records expected to cause considerable damage.

Subsequently, a nonlinear inelastic dynamic time history analysis is performed, using a sample of 16 near fault ground motion records from Aquila and Norcia earthquakes in Italy, to obtain the displacement time history of each record, which will be used to determine the damage limit states achieved according to “T. Rossetto, A. Elnashai” vulnerability relationships.

This thesis consists of seven chapters, the first chapter is an introduction to the procedures used in the thesis, and a summary for each chapter.



In Chapter 2, identification of near fault ground motion phenomenon, characteristics, and parameters is discussed with mentioning the difference between near and far fault, followed by the pulse characteristics and its effect on the elastic response spectrum.

In Chapter 3, A description of the building, and its modelling in Seismostruct are provided, including the building layout, material characteristics, typical reinforcement detailing of the structural elements, applied loads, seismic characteristics, and additionally eigenvalue and pushover analyses are performed.

In Chapter 4, a brief description of the ground motion records used, including maps and figures showing the projection of the rupture surface, each station distance from the epicenter, and the criterion of picking up pulse like records (Pulse Indicator).

In Chapter 5, a description of the new Chilean seismic code provisions, which are used to mitigate the damage reached is provided, the mitigation is in form of strengthening the building with the required number of shear walls in Y-direction only, and additionally eigenvalue and pushover analyses are performed.

In Chapter 6, the results from subjecting the building to the near fault ground motion records are obtained, these results are the maximum top floor displacement that the building undergoes due to a certain ground motion record.

The displacement value indicates the structural damage state of the building, the results are illustrated in plots and tabulated forms for each earthquake showing the inter-storey drift (maximum roof displacement/building height) and the corresponding predefined limit damage state.

In Chapter 7, the conclusions upon reviewing the results obtained are summed up in the form of figures and tables representing the damage limit states reached by the original and strengthened buildings, and showing the improvement percentage.



CHAPTER 2 NEAR-FAULT GROUND MOTIONS

2.1. Statement of Problem

Near-field ground motions have caused much damage in the vicinity of seismic sources during recent earthquakes (Northridge 1994, Kobe 1995). There is evidence indicating that ground shaking near a fault rupture is characterized by a short-duration impulsive motion that exposes the structure to high input energy at the beginning of the record. This pulse-type motion is particularly prevalent in the "forward" direction, where the fault rupture propagates towards the site at a velocity close to the shear wave velocity.

The effect of this pulse type motion on the response is important in the design of structures for near-fault events. In the near-fault region, the short travel distance of the seismic waves does not allow enough time for the high frequency content to be damped out of the record as is normally observed in far field records.

This phenomenon requires consideration in the design process for structures that are located in the near-field region, which is usually assumed to extend about 20 to 60 km from the seismic source (1996 SEAOC Bluebook).

Near-field ground motions exhibit special response characteristics that are different from the response characteristics of "ordinary" ground motions. This is shown in Fig. 2.1, which compares velocity response spectra of near-field and ordinary ground motions. The solid line (denoted as 15-D*) represents the mean velocity spectrum of a set of ordinary ground motions whose individual spectra resemble the 97 UBC soil type SD spectrum. The other lines correspond to the velocity spectra of individual near-field ground motions from different events.

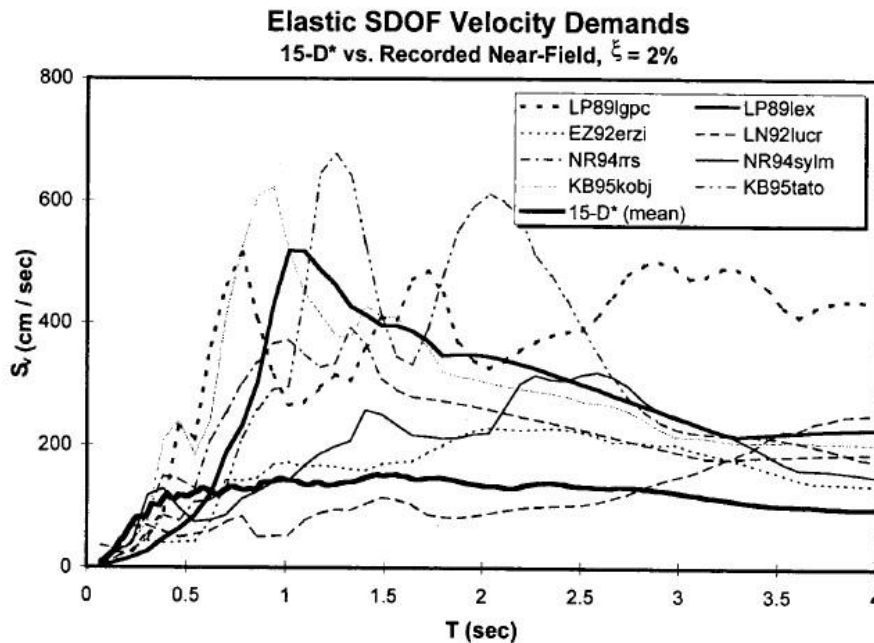


Fig. 2.1 Velocity Response Spectra of Near-Field and Ordinary Ground Motions

2.2. Near-Fault effects

Within this near-fault zone, ground motions are significantly influenced by the rupture mechanism, the direction of rupture propagation relative to the site, and possible permanent ground displacements resulting from the fault slip. These factors result in effects termed herein as “rupture-directivity” and “fling step.” The estimation of ground motions close to an active fault should account for these characteristics of near-fault ground motions.

Forward directivity occurs when the rupture propagates toward a site and the direction of slip on the fault is also toward the site. This occurs because the velocity of fault rupture is close to (generally slightly less than) the shear wave velocity of the rock near the source. As shown in Figure 2.2 for a strike-slip focal mechanism, as the rupture front propagates away from the hypocenter and toward a site, energy is accumulated near the rupture front from each successive zone of slip along the fault. The wave front arrives as a large pulse of motion (a shock wave effect) that occurs at the beginning of the record (Somerville et al. 1997a) and is polarized in the strike-normal direction. The pulse of motion is typically characterized by large amplitude at intermediate to long periods and short duration.

If a site is located near the epicenter, i.e., rupture propagates away from the site, the arrival of seismic waves is distributed in time. This condition, referred to as backward directivity, is characterized by motions with relatively long duration and low amplitude.

Neutral directivity occurs for sites located off to the side of the fault rupture surface (i.e., rupture is neither predominantly toward nor away from the site).

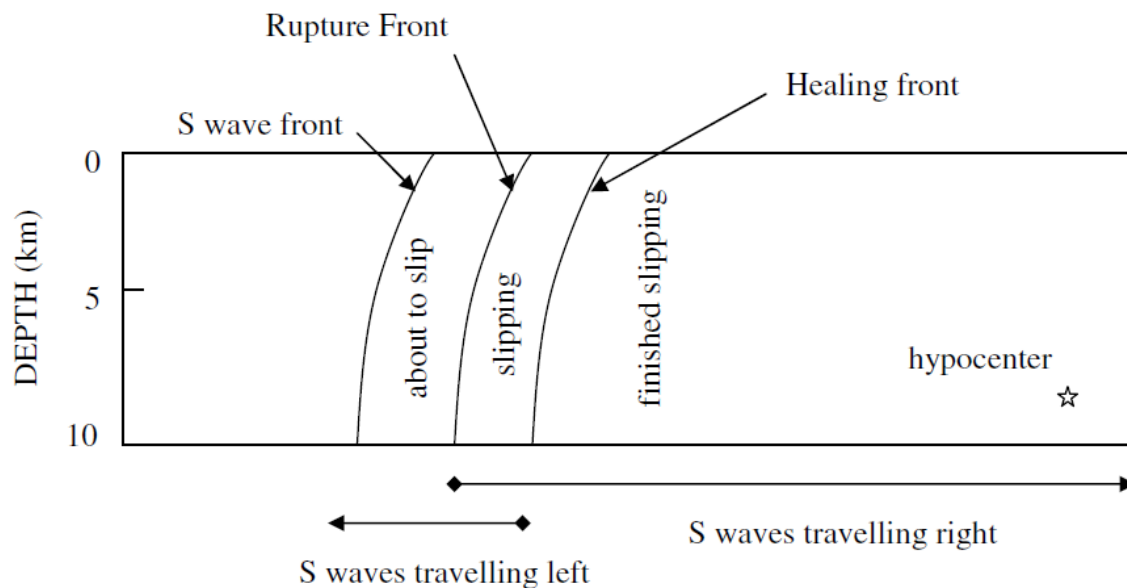


Fig. 2.2 Schematic diagram of rupture-directivity effects for a vertical strike-slip fault. The rupture begins at the hypocenter and spreads at a speed that is about 80% of the shear wave velocity. The figure shows a snapshot of the rupture front at a given instant (from Somerville et al. 1997a).

The effects of rupture-directivity on ground displacements recorded during the 1989 Loma Prieta earthquake are shown in Figure 2.3. The epicenter of the earthquake is near Corralitos and Branciforte Drive, where the horizontal ground displacements are moderate on both fault-normal and fault-parallel components. This is attributed to backward directivity.

At the ends of the fault, however, at Lexington Dam and Hollister, forward directivity causes the horizontal ground motions in the fault-normal direction to be impulsive and much larger than the fault-parallel motions, which are similar to those near the epicenter. The large impulsive motions occur only in the fault-normal direction and only away from the epicenter.

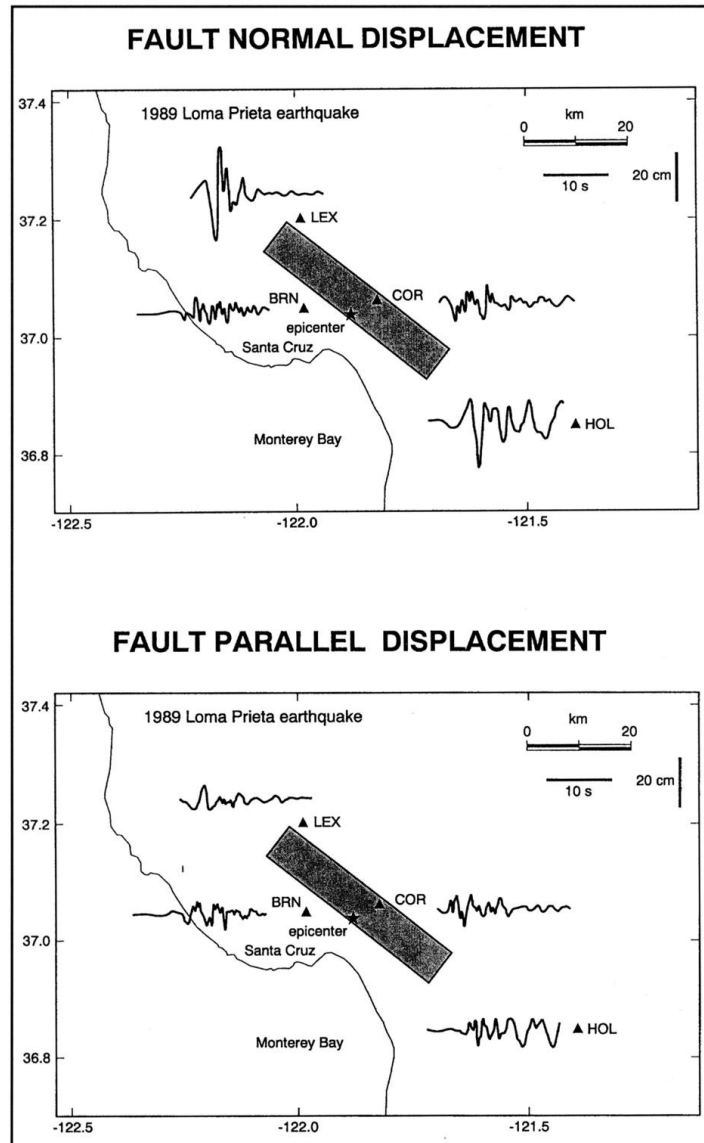


Fig. 2.3 Rupture-directivity effects in the recorded displacement time histories of the 1989 Loma Prieta earthquake, for the fault-normal (top) and fault-parallel (bottom) components. Source: EERI, 1995.

2.3. Directional effects

In the case of an earthquake, ground motion recorded at near-source sites may be subjected to rupture directivity effects which result in a low frequency full cycle velocity pulse at the beginning of the signal. The occurrence of this effect depends on the rupture process and on the geometrical configuration of the fault and the site. More specifically, according to Somerville, the seismic energy radiated from the source arrives almost in single large pulse of motion if the rupture propagates toward the site, the direction of slip on the fault is aligned with the site, and the propagation velocity of rupture is almost as large as the shear wave velocity.

Figure 2.4 (a) sketches rupture directivity effect in the simple case of a unilateral strike-slip fault. As the rupture, which may be seen as a point source moving along the fault, goes away from the epicenter, it radiates energy in seismic waves originated at different instants. Roughly speaking, the wave fronts tend to all arrive at the same time in site 2, this may be seen as constructive interference of waves.

Conversely, in site 1, with respect to which the rupture moves away, waves radiated in different instants tend also to arrive in different moments. Therefore, in the former case the energy is concentrated in a high amplitude and short duration (impulsive) motion, whereas in the latter the energy is spread over a larger amount of time and in a lower amplitude signal.

Because of the radiation pattern, in the case of strike-slip ruptures, directivity pulses are oriented in the rupture-normal (RN) direction that corresponds to the strike-normal direction, while in the rupture-parallel direction (RP), which coincides with the strike-parallel direction, minor directivity effects, if any, are expected. In dip-slip earthquakes, the rupture directivity pulse is expected in the direction normal to the fault dip, which in the horizontal plane reflects on the strike-normal direction. Hereinafter, referring to the horizontal ground-motion components, strike-normal and strike-parallel directions will be referred to as fault-normal (FN) and fault parallel (FP) (Figure 2.4 (b)).

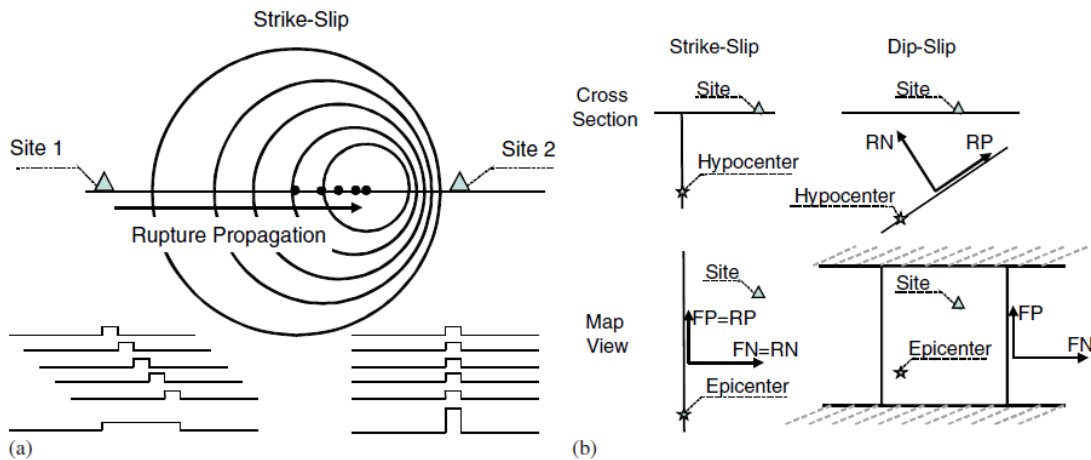


Fig. 2.4 (a) Directivity of seismic energy: snapshot of wave fronts (adapted from Singh) and (b) directions of effects' observation for strike-slip and dip-slip cases (adapted from Somerville).

Rupture-directivity effects can be present both for strike-slip and dip-slip events. In dip-slip events, forward-directivity conditions occur for sites located near the up-dip projection of the fault plane. As with strike-slip focal mechanisms.

The radiation pattern of the shear dislocation of the fault causes the pulse to be mostly oriented perpendicular to the fault, causing the fault normal component of the motion to be more severe than the fault-parallel component (Somerville, 1998).

Modern digital recordings of near-fault ground motions, for example from the 1999 Turkey and Taiwan earthquakes, contain permanent ground displacements due to the static deformation field of the earthquake.

These static displacements, termed “fling step,” occur over a discrete time interval of several seconds as the fault slip is developed. Fling step displacements occur in the direction of fault slip, and therefore are not strongly coupled with the aforementioned dynamic displacements referred to as the “rupture-directivity pulse.”

In strike-slip faulting, the directivity pulse occurs on the strike-normal component while the fling step occurs on the strike parallel component.

In dip-slip faulting, both the fling step and the directivity pulse occur on the strike-normal component. The orientations of fling step and directivity pulse for strike-slip and dip-slip faulting are shown schematically in Figure 2.5, and time histories in which these contributions are shown together and separately are shown schematically in Figure 2.6.

The available strong motion data that can be used to quantify these effects are limited, although the recent earthquakes in Turkey and Taiwan have significantly supplemented the near-fault ground motion database.

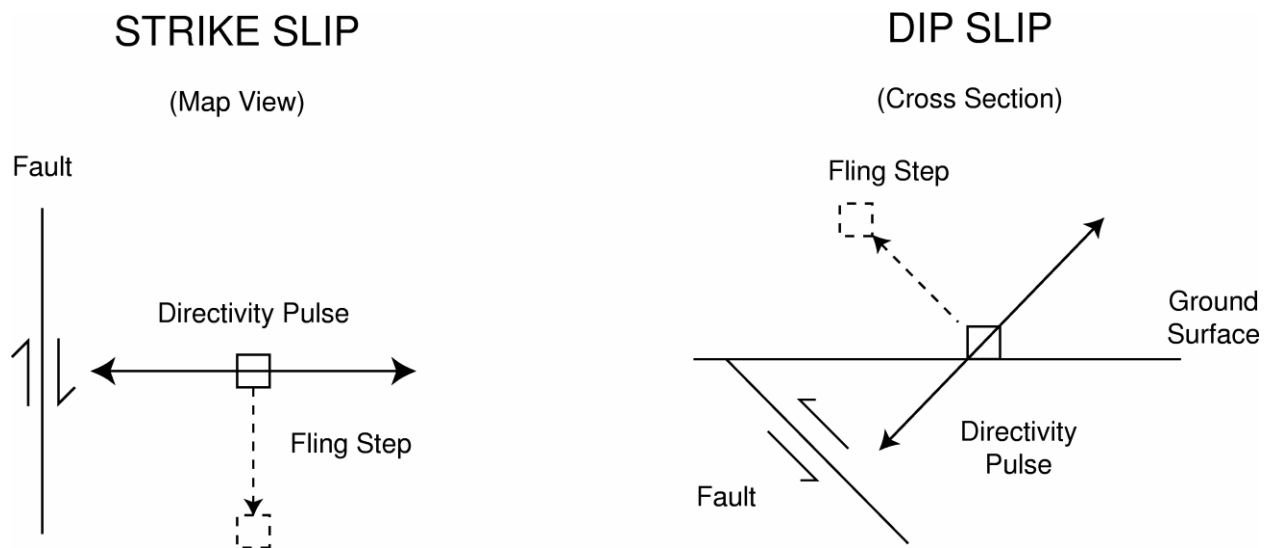


Fig. 2.5 Schematic diagram showing the orientations of fling step and directivity pulse for strike-slip and dip-slip faulting.

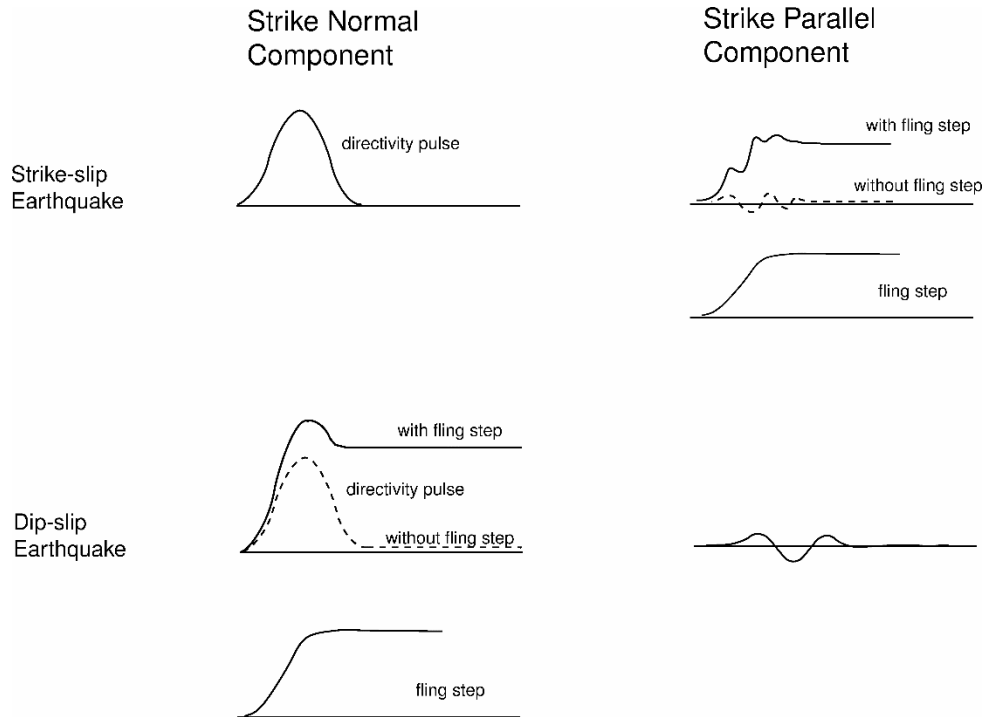


Fig. 2.6 Schematic diagram of time histories for strike-slip and dip-slip faulting in which the fling step and directivity pulse are shown together and separately.

2.4. Parameterization of Near-Fault Ground Motion

Somerville et al. (1997a) parameterized the conditions that lead to forward and backward-directivity.

As shown in Figure 2.7, the spatial variation of directivity effects depends on the angle between the direction of rupture propagation and the direction of waves traveling from the fault to the site (θ for strike-slip faults, and ϕ for dip-slip faults), and on the fraction of the fault rupture surface that lies between the hypocenter and the site (X for strike-slip faults and Y for dip-slip faults). More significant forward-directivity results from smaller angles between the site and fault and for larger fractions of ruptured fault between the site and hypocenter. It should be noted that even when the geometric conditions for forward directivity are satisfied, the effects of forward directivity may not occur. This could happen if a station is at the end of a fault and rupture occurs toward the station but slip is concentrated near the end of the fault where the station is located.

To account for directivity effects, Somerville et al. (1997a) correlated the residuals of response spectral ordinates (at 5% damping) to the geometric parameters defined in Figure 2.7, with the results shown in Figure 2.8. The ground motion parameters that are modified are the average horizontal response spectra and the ratios of fault-normal to fault-parallel response spectra. Details of the model are presented in Section 4.2.1. The 1997 UBC accounts for near-fault effects by means of near-source factors, N_a and N_v , applied to the low period (acceleration) and

intermediate period (velocity) parts of the acceleration response spectrum, respectively. The near-source factors are specified for distances less than 15 km and for three different fault types (Table 4.1). The near-source factors in the UBC are compatible with the average of the fault-normal and fault-parallel components in the Somerville et al. (1997a) model, and hence, the code provisions do not address the larger fault-normal component of motion (Somerville, 1998).

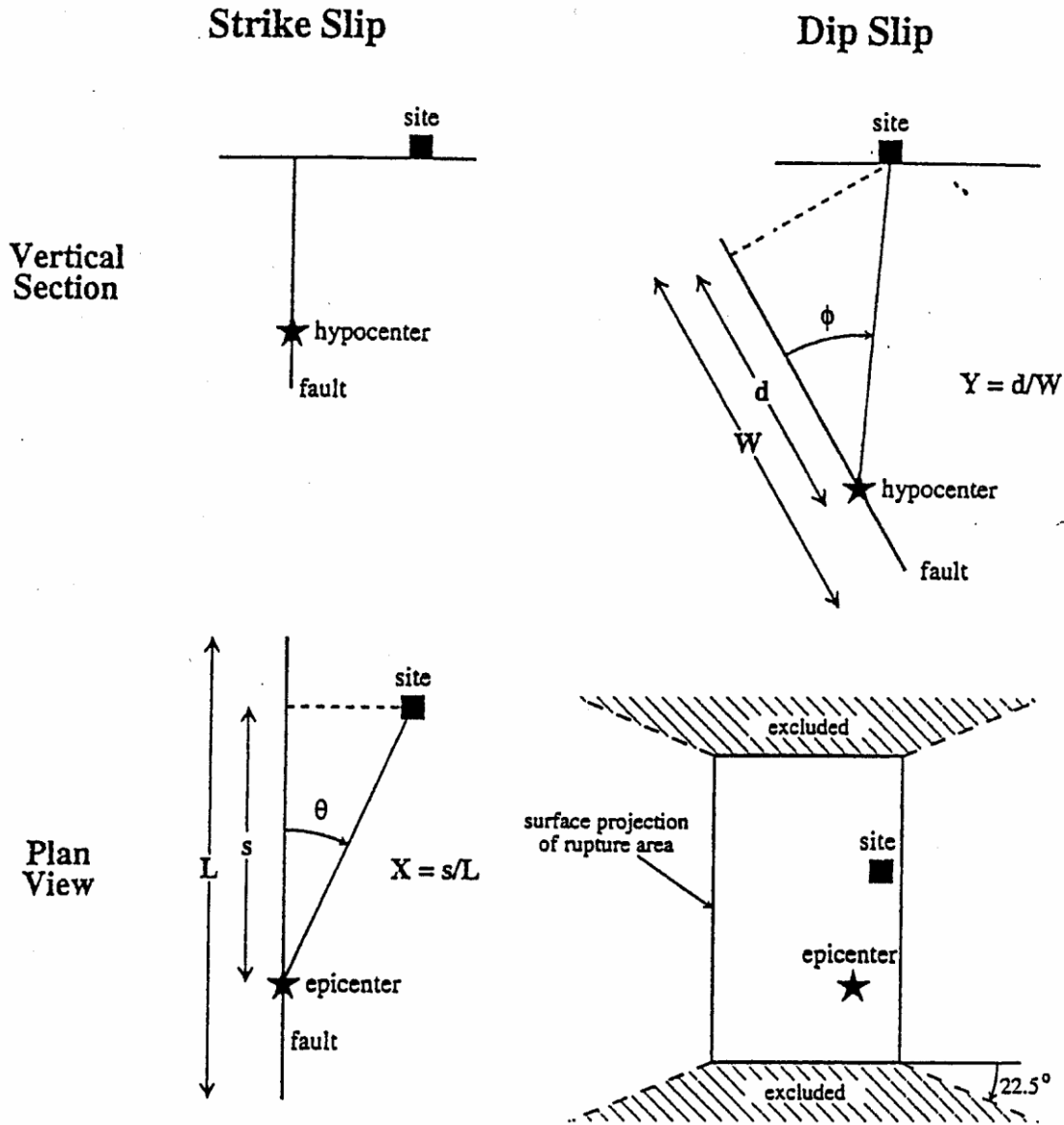
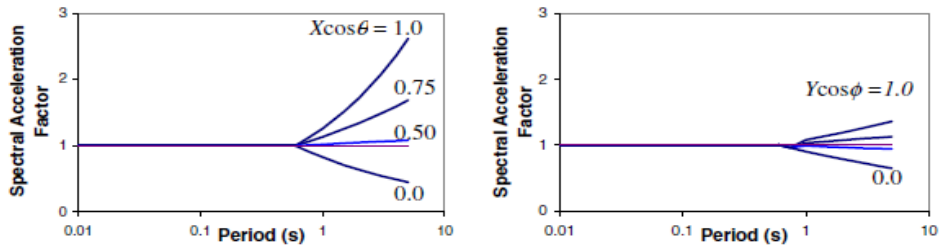
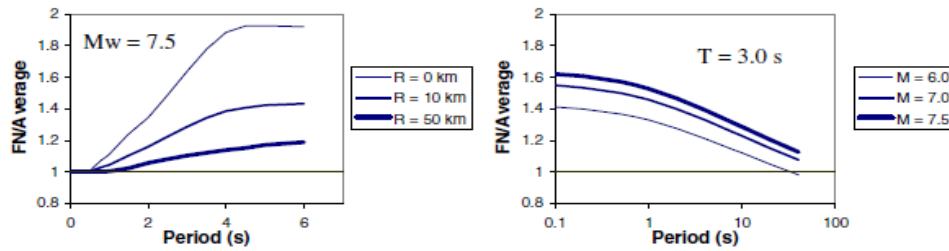


Fig. 2.7. Parameters used to define rupture-directivity conditions (adapted from Somerville et al. 1997a).



(a) Average response spectra ratio, showing dependence on period and on directivity parameters



(b) Strike-normal to average horizontal response spectral ratio for maximum forward-directivity conditions ($X\cos\theta = 1$)

Fig. 2.8. Predictions from the Somerville et al. (1997a) relationship for varying directivity conditions.

(a) Short-period factor (N_d)

Seismic Source Type	Closest Distance to Known Seismic Source ¹		
	≤ 2 km	5 km	≥ 10 km
A	1.5	1.2	1.0
B	1.3	1.0	1.0
C	1.0	1.0	1.0

(b) Intermediate-period factor (N_v)

Seismic Source Type	Closest Distance to Known Seismic Source ¹			
	≤ 2 km	5 km	10 km	≥ 15 km
A	2.0	1.6	1.2	1.0
B	1.6	1.2	1.0	1.0
C	1.0	1.0	1.0	1.0

Table 2.1. Near-source factors from the 1997 Uniform Building Code.

2.5. Pulse characteristics

Research on the response of structures to near-fault motions has found a time history representation of the motions to be preferable to a response spectrum representation (e.g. Somerville, 1998; Alavi and Krawinkler, 2000; Sasani and Bertero, 2000; Rodriguez-Marek, 2000). A time history representation is preferable because the frequency-domain characterization of ground motion (i.e. through a response spectrum) implies a stochastic process having a relatively uniform distribution of energy throughout the duration of the motion. When the energy is concentrated in a few pulses of motion, the resonance phenomenon that the response spectrum was conceived to represent may have insufficient time to build up (Somerville, 1998).

Krawinkler and Alavi (1998) identify the velocity pulse by a clear and global peak in the velocity response spectrum of the ground motion which is illustrated in Figure 2.9.

Some simplified pulses are shown in Figure 2.10. The simplified sine-pulse representations of velocity time histories are defined by the number of equivalent half-cycles, the period of each half-cycle, and the corresponding amplitudes. To represent bidirectional shaking, a sine-pulse representation of the fault-parallel component is needed along with the time lag between initiation of the fault-normal and fault-parallel components.

A simple characterization is possible with the use of peak horizontal velocity (PHV), approximate period of the dominant pulse (T_v), and the number of significant half-cycles of motion in the (larger) fault-normal direction.

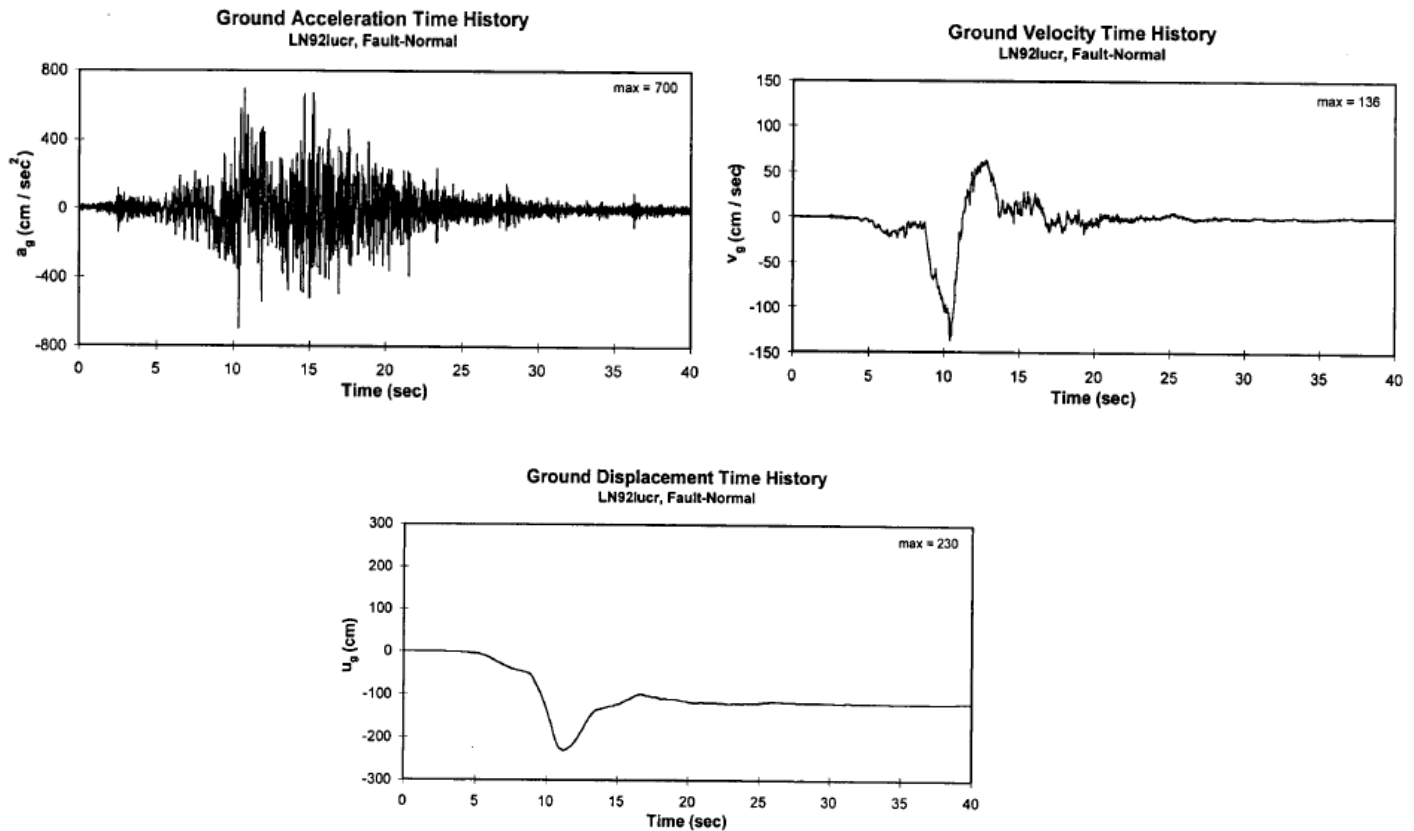


Fig. 2.9. Ground Acceleration, Velocity, and Displacement Time Histories of Fault-Normal Component of Record LN921ucr with Forward Directivity

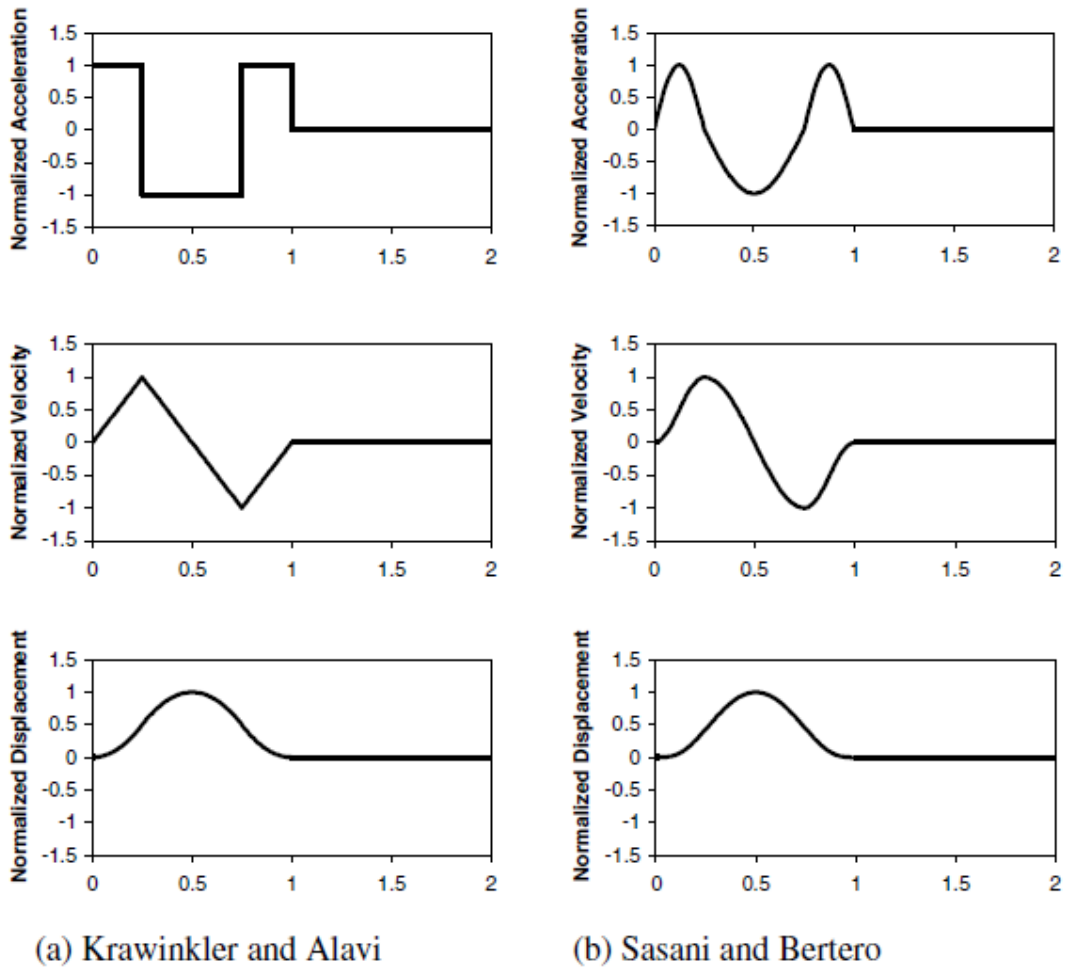


Fig 2.10. Simplified pulses that have been used by some researchers.

2.6. Effect of the pulse on the acceleration response spectrum

It is observed that in near field ground motion, there is a bell shaped curve in the declining part of the acceleration response spectrum which is due to the constructive pulse of the forward directivity as shown in figure (2.11a).

This bell shaped curve lies around the predominant period of the pulse (T_v) which affects buildings have elastic period close or equal to half the pulse period, hence it should be taken into consideration while designing such buildings in order to avoid response amplification as shown in figure (2.11b).

Usually it is taken into account in the design process that the ductility demand is equal to the behavior factor, but in reality the ductility demand is much bigger than the behavior factor due to the near fault effect (existence of a constructive pulse), and this is illustrated in figure 2.12.

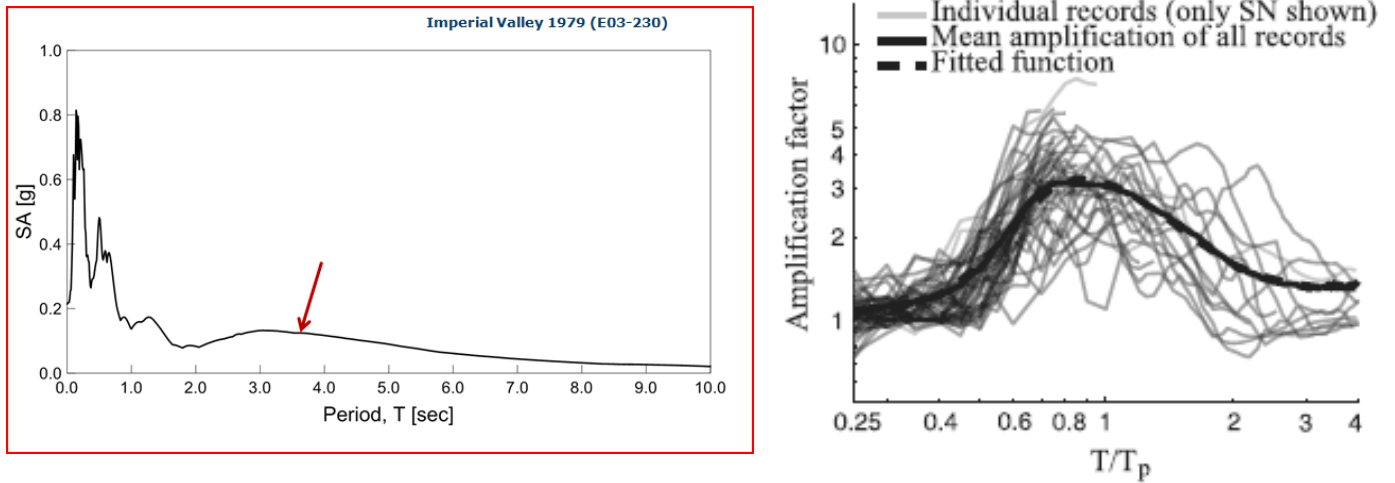


Fig. 2.11. Bell shaped amplification around T_p .

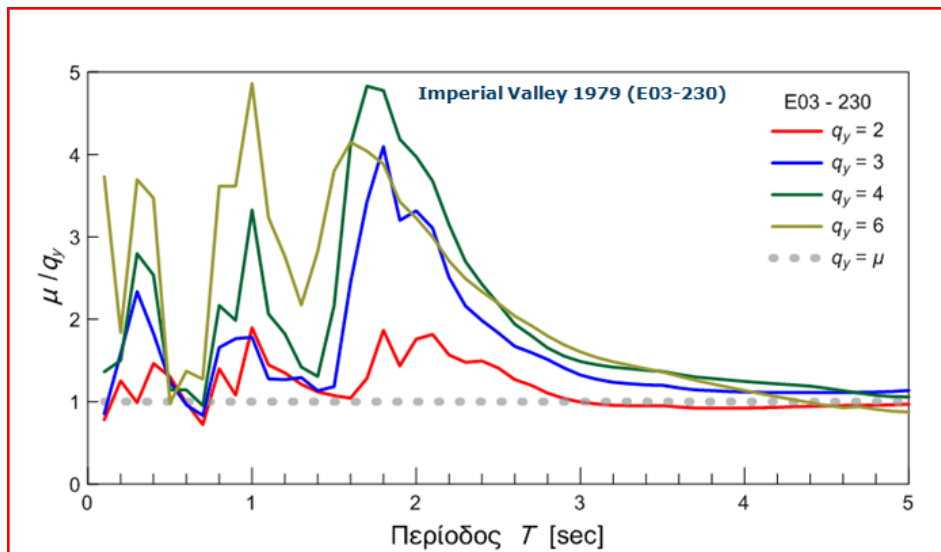


Fig. 2.12. Ductility demand to behavior factor ratio (μ/q_y) for different behavior factor (q_y) curves.

CHAPTER 3 BUILDING DESCRIPTION

The building used for the study of seismic near field response is an eight-storey building of reinforced concrete. The building is located in the municipality of Athens, Geroulanou Street 3, Palaio Faliro. It has a total height of 23.8 m and the dimensions of the floor plan is 25.65x10.77 m². The ground floor and the rest of the floors have a height of 2.98 m. Here are the top view (Figure 3.1) and the section of the building (Figure 3.2).

3.1. Building Layout

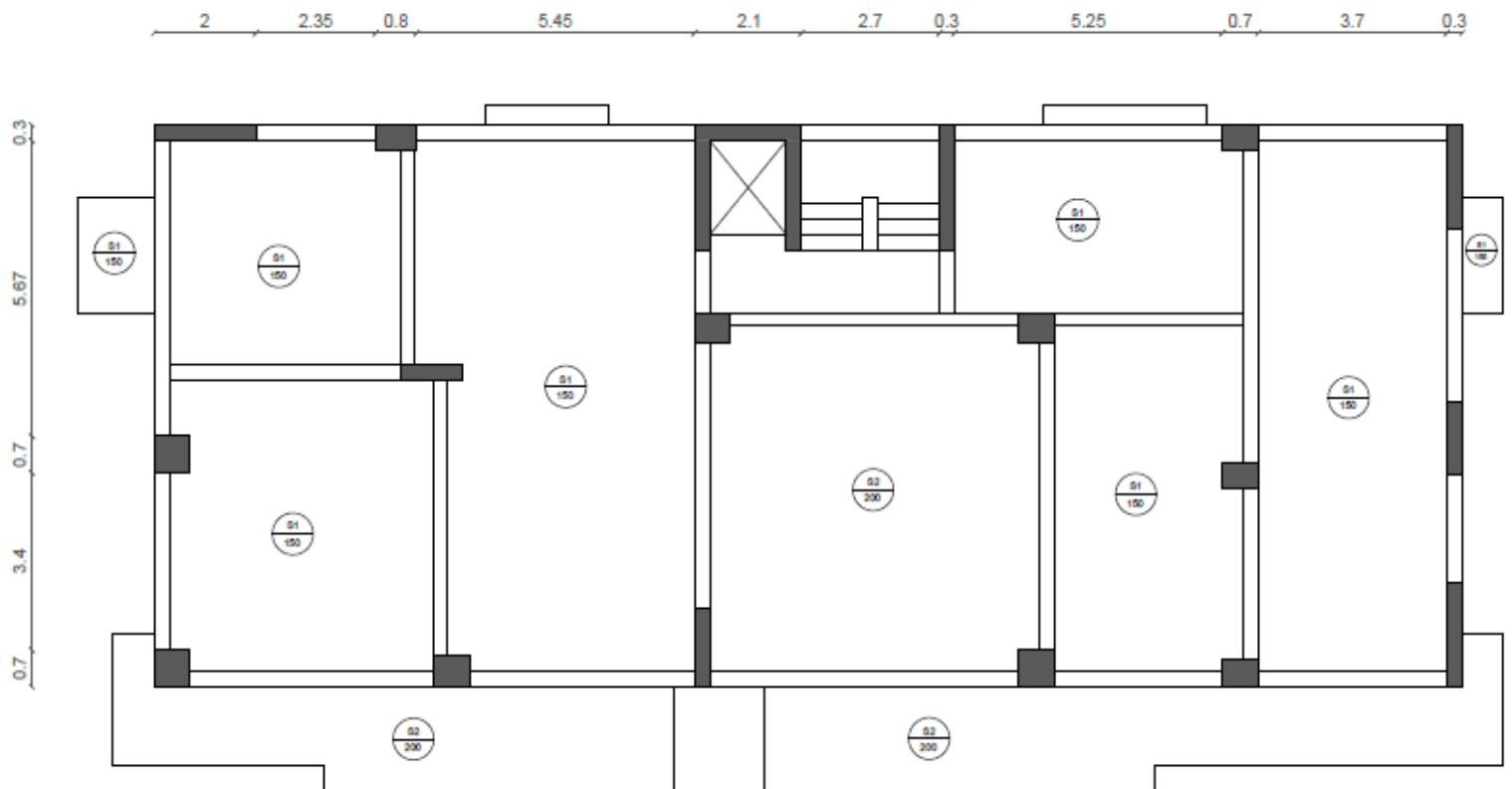
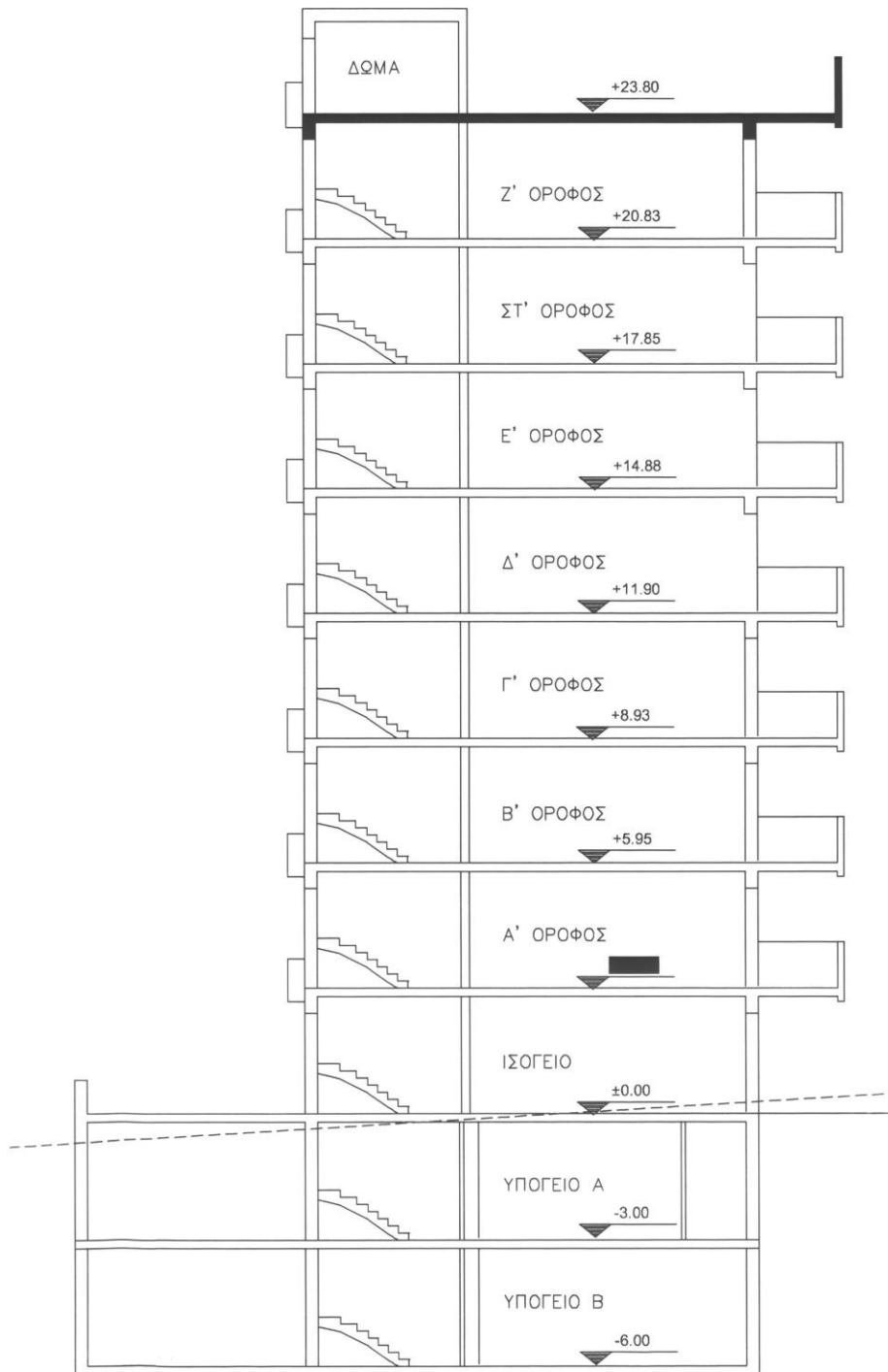


Figure 3.1. Plan View of the Building



ΕΝΔΕΙΚΤΙΚΗ ΤΟΜΗ

Figure 3.2. Section Side View of the Building

3.2. Modelling of the building using Seismostruct:

The Reinforced concrete building consists of beams which are simulated as T-sections at the interior spans while are considered as L-sections on the perimeter of the building. Shear walls, Beams and Columns are modeled as inelastic forced based plastic hinge elements (infrmFBPH), while the slabs are considered as rigid diaphragms as illustrated in figures 3.4 and 3.5 respectively.

The structure was modelled using the building modeller of seismostruct program, the height of each floor was taken approximately 3m. The modelling procedures will be illustrated in the following subdivisions.

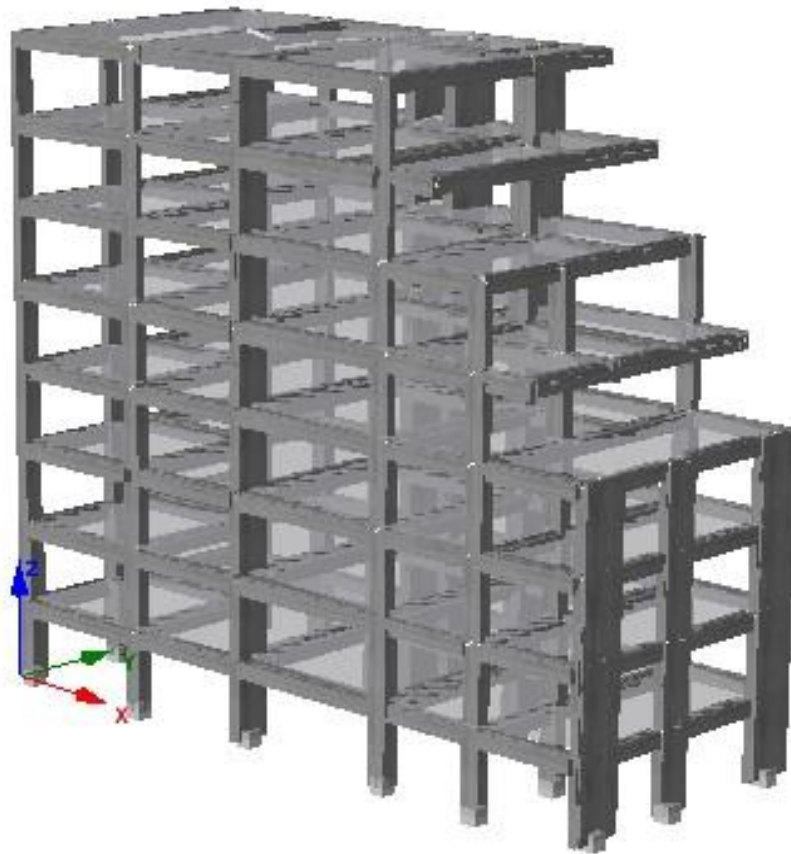


Figure 3.3. 3D Model of the Building in Seismostruct

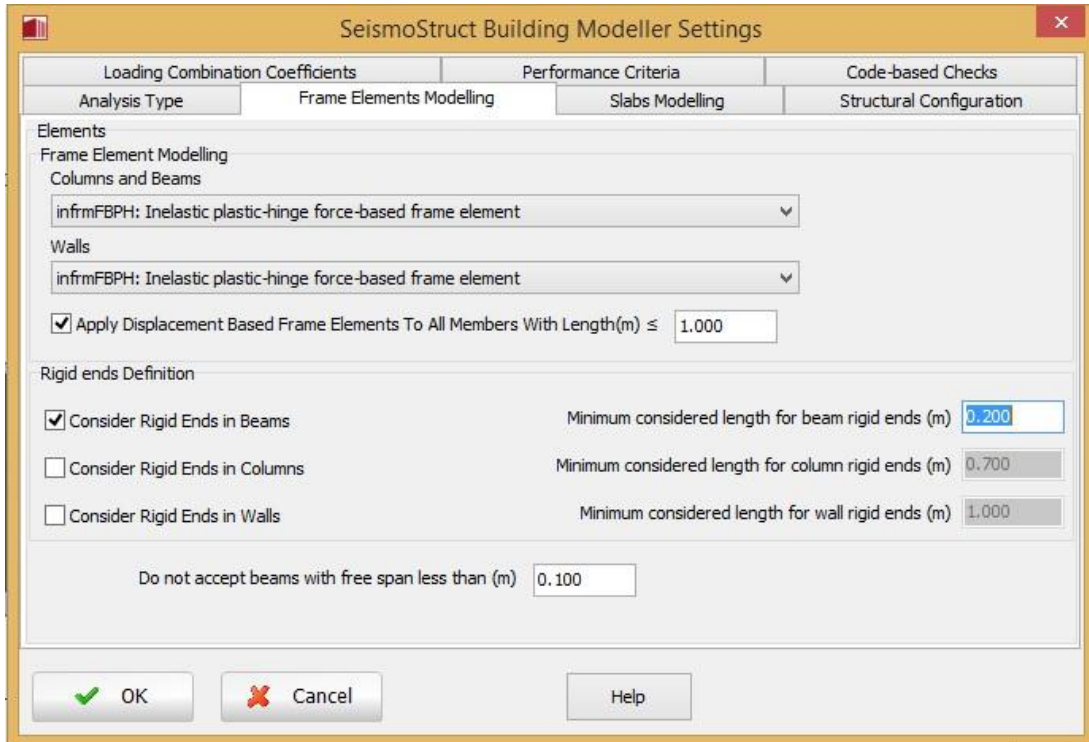


Figure 3.4. Frame elements modelling types in Seismostruct.

Constraint type	Master Nodes	Restrained DOFs	Slave Node(s)
Rigid Diaphragm	n6_C9up	X-Y plane	n6_W15up n6_C16up n6_C10up n6_B21...
Rigid Diaphragm	n6_C11up	X-Y plane	n6_C13up n6_C14up n6_C8up n6_B5_B...
Rigid Diaphragm	n5_W5up	X-Y plane	n5_W6up n5_W3up
Rigid Diaphragm	n5_C9up	X-Y plane	n5_W15up n5_C16up n5_C10up n5_B10...
Rigid Diaphragm	n5_C2up	X-Y plane	n5_C8up n5_C14up n5_W15up n5_C9up...
Rigid Diaphragm	n6_C10up	X-Y plane	n6_C16up n6_C17up n6_C12up n6_B23...
Rigid Diaphragm	n6_W1up	X-Y plane	n6_C2up n6_C8up n6_B5_B15_B14
Rigid Diaphragm	n6_W5up	X-Y plane	n6_W6up n6_W3up
Rigid Diaphragm	n7_C9up	X-Y plane	n7_C14up n7_B21_B22_B6_B7 n7_B21_B...
Rigid Diaphragm	n8_C8up	X-Y plane	n8_W13up n8_C14up n8_C9up n8_B6_B...
Rigid Diaphragm	n8_C7up	X-Y plane	n8_C12up n8_W13up n8_C8up n8_W4u...
Rigid Diaphragm	n8_W1up	X-Y plane	n8_C10up n8_C11up n8_C12up n8_C7u...
Rigid Diaphragm	n8_W5up	X-Y plane	n8_W6up n8_W3up
Rigid Diaphragm	n8_W5up	X-Y plane	n8_W4up n8_C8up n8_W6up n8_B6_B7...
Rigid Diaphragm	n8_W6up	X-Y plane	n8_C9up n8_B6_B7_B17 n8_B5_B19
Rigid Diaphragm	n7_C8up	X-Y plane	n7_W13up n7_B21_B11_B12 n7_B21_B22...

Figure 3.5. Rigid diaphragms modelled in Seismostruct.

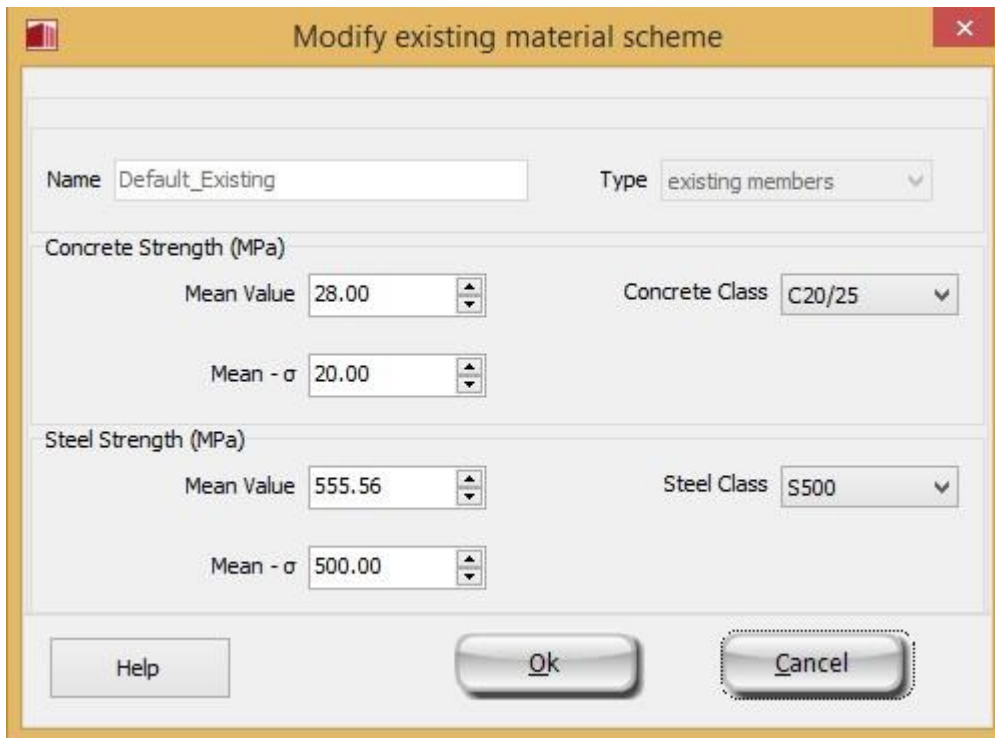
3.3. Materials:

3.3.1. Concrete

The concrete used for construction of the building is C20/25 (with $f_{ck} = 20$ MPa).

3.3.2. Steel Reinforcement

The steel used in reinforcement is grade S500 ($f_{yk}=500$ Mpa).



Property	Value
Name	Default_Existing
Type	existing members
Concrete Strength (MPa)	
Mean Value	28.00
Mean - σ	20.00
Concrete Class	C20/25
Steel Strength (MPa)	
Mean Value	555.56
Mean - σ	500.00
Steel Class	S500

Figure 3.6. Material characteristics in Seismostruct

3.4. Modeling Elements

3.4.1. Beams

The cross section of the typical beam is shown in Figure 3.7 and the side view in Figure 3.8. In these figures the layout of the main reinforcement satisfies all the requirements of the codes, including the requirement that the compression reinforcement of a section to be at least 50 percent of the tension.

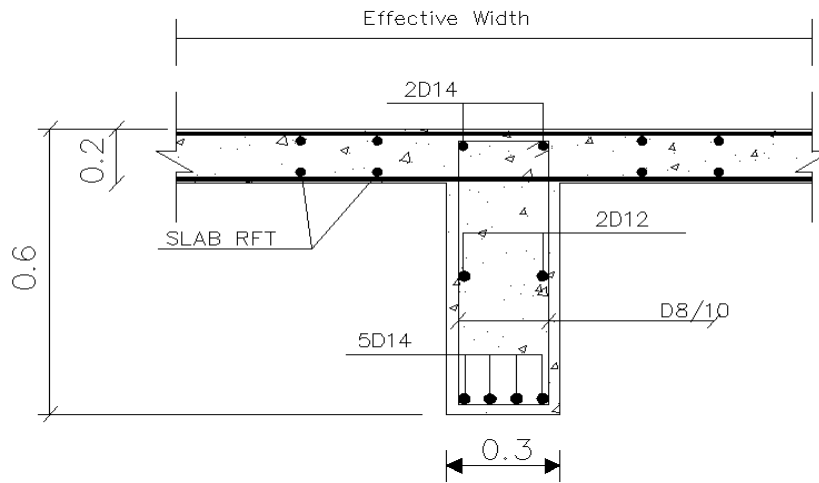


Figure 3.7. Cross section of the Beam

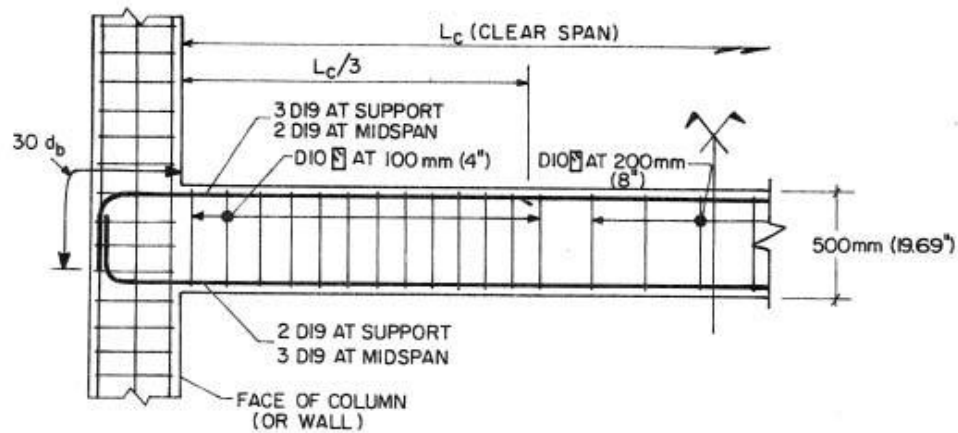


Figure 3.8. Side View of the Beam

3.4.2. Columns

The cross section of the typical column is shown in the figure below. This section with the exception of the stirrups is the same for all columns of the structure.

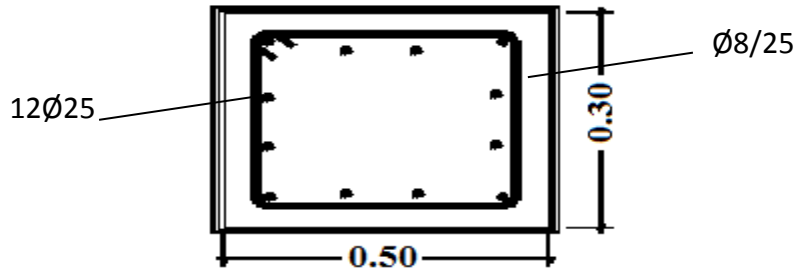


Figure 3.9. Typical column Section

3.4.3. Walls

The cross section of the wall in the structure is shown in figure 3.10. The details of stirrups for shear walls vary between members of the construction. Also the longitudinal reinforcement varies with respect to each floor.

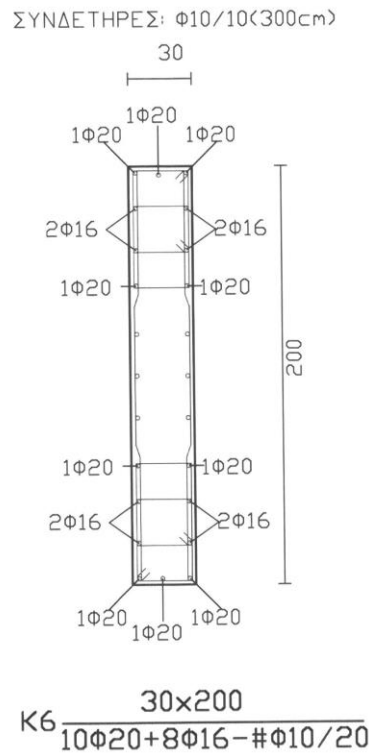


Figure 3.10. Wall Section

3.5. Loading

Loads of the building consists of live loads and dead loads. Dead loads are the own weight of the members, floor covering and wall loads. Since the walls are divided into exterior and interior walls, the interior wall loads are distributed on the slabs while the exterior wall loads are uniformly distributed on the beams. All dead and live loads are transferred to the beams as distributed loads according to the following figures.

Beam-Column Element Types

Element Class	Section Name	Section Fibres	Plastic-hinge length Lp/L (%)	Damping	Additional Mass
class_B13_1	sec_BL13_1 sec_BR13_1	150	16.67	None	1.43261
class_B14_1	sec_BL14_1 sec_BR14_1	150	16.67	None	1.4743
class_B16_1	sec_BL16_1 sec_BR16_1	150	16.67	None	0.91743119
class_B17_1	sec_BL17_1 sec_BR17_1	150	16.67	None	1.63922
class_B19_1	sec_BL19_1 sec_BR19_1	150	16.67	None	0.81321159
class_B18_1	sec_BL18_1 sec_BR18_1	150	16.67	None	4.45276
class_B20_1	sec_BL20_1 sec_BR20_1	150	16.67	None	1.65042
class_B21_1	sec_B21_1	150	16.67	None	13.70591
class_B22_1	sec_BL22_1 sec_BR22_1	150	16.67	None	2.83192
class_B24_1	sec_BL24_1 sec_BR24_1	150	16.67	None	1.88947
class_B23_1	sec_B23_1	150	16.67	None	2.26799
class_B8_1	sec_B8_1 sec_BR8_1	150	16.67	None	1.35004

Figure 3.11. Loads transferred to the beams in the form of additional mass by the software.

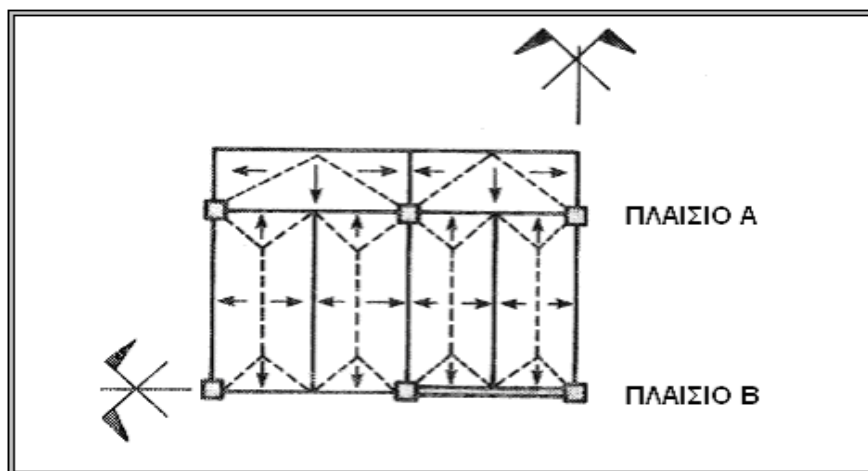


Figure 3.12. Description of how the loads are being transferred to the beams.

Loads

Additional Permanent Loads (G') & Live Loads (Q) :

G' (kN/m²)

Q (kN/m²)

Slab Inclination

Inclined or elevated slab (defined by 3 points)

Fig. 3.13. Uniformly distributed loads “including interior walls” on the slabs.

Loads

Additional Permanent Loads (G') & Live Loads (Q) :

G' (kN/m²)

Q (kN/m²)

Slab Inclination

Inclined or elevated slab (defined by 3 points)

Fig. 3.14. Uniformly distributed loads for the stairs slab.

B 1 Display/Modify Effective Width

Additional Permanent Load (G') :

G' (kN/m)

Fig. 3.15. Uniformly distributed wall loads on exterior beams

Loading Combination Coefficients Perf

Gravity & Live Loads

Gravity Loads Coefficient C_g

Live Loads Coefficient C_q

Fig. 3.16. Loading Combination coefficients.

3.6. Seismic Characteristics :

The building is located in an area with seismic hazard zone I, which has ground acceleration $a = 0.16 \text{ g}$. The building's importance class is II, which has importance factor is $\gamma_1 = 1.00$. The construction is based on soil class B. The building is made of reinforced concrete when the seismic behavior factor is $q_d = 3.5$. The damping of the building is $\delta = 5\%$.

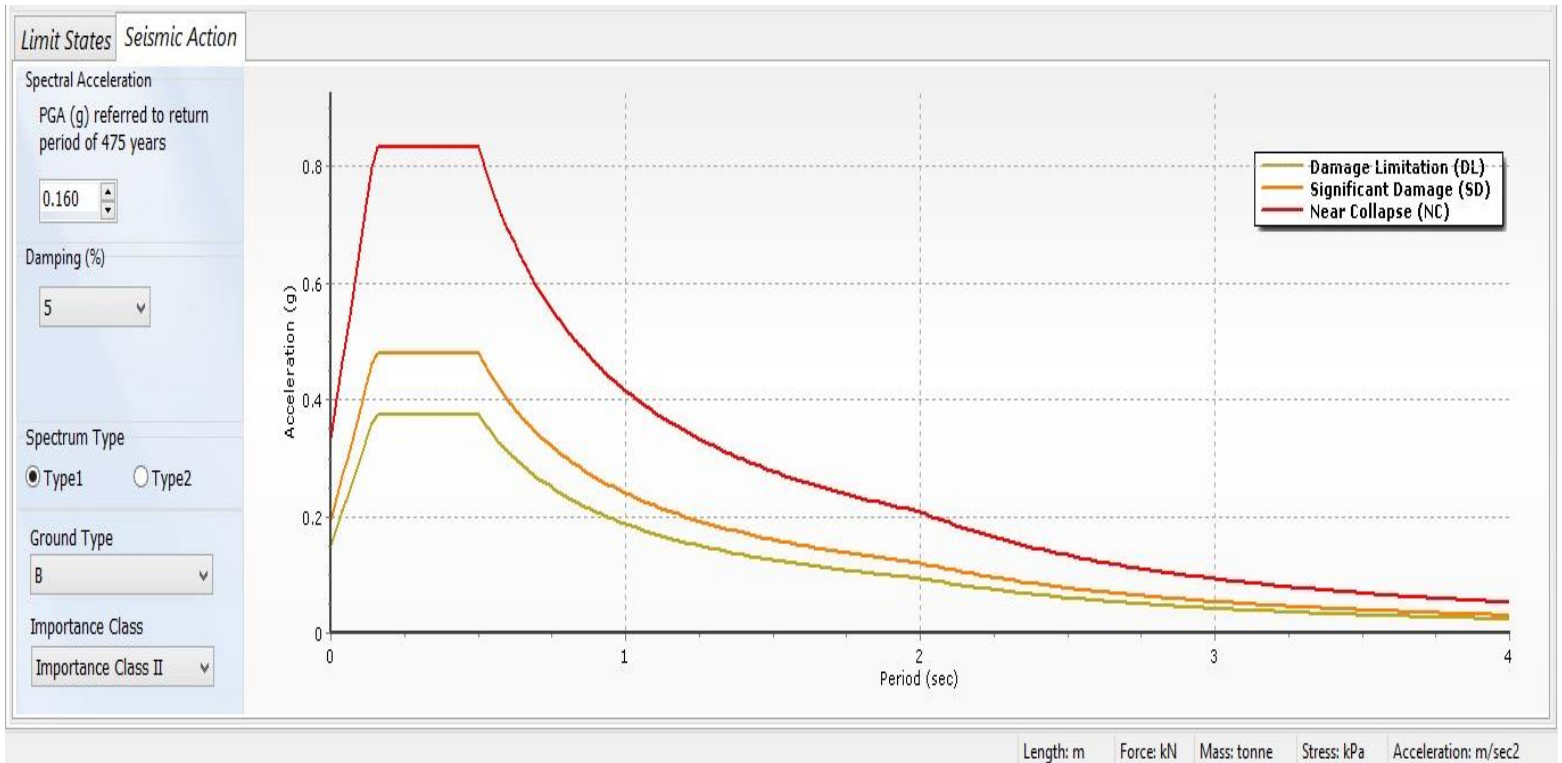
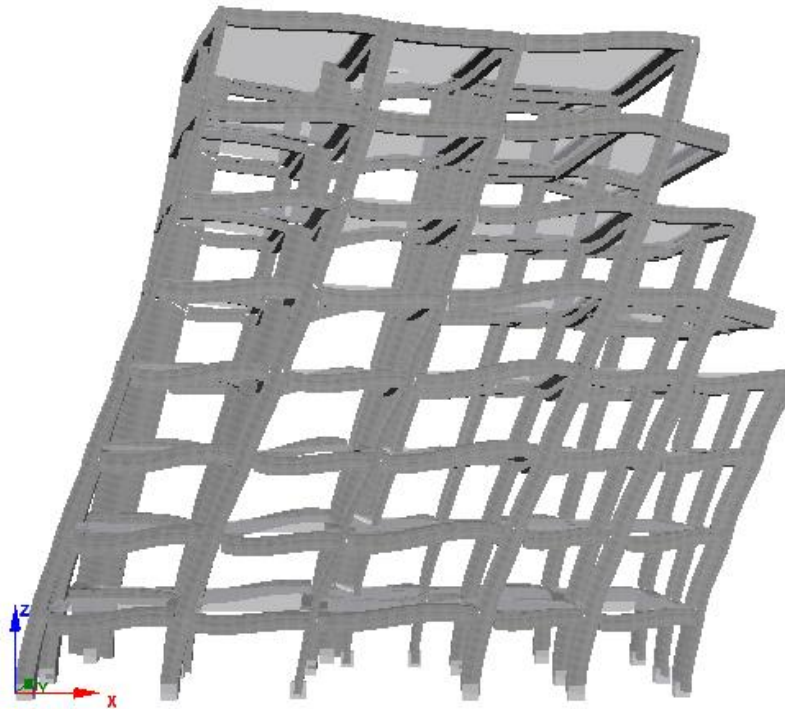


Figure 3.17. Seismic action parameters in seismostruct.

3.7. Eigenvalues Analysis

In the calculation of eigenvalues analysis the efficient Lanczos algorithm [Hughes, 1987] is used for the evaluation of the structural natural frequencies and mode shapes.

The number of Eigenvalues used is 10 as shown in table 3.1.



**Figure 3.18. Deformed shape of the building at the fundamental period (0.608 secs)
From Eigen-value analysis.**

MODAL PERIODS AND FREQUENCIES		
Mode	Period	Frequency
	(sec)	(Hertz)
1	0.608451	1.6435186
2	0.543294	1.8406233
3	0.326389	3.0638289
4	0.207094	4.8287288
5	0.165007	6.0603497
6	0.137798	7.2569797
7	0.132294	7.5589308
8	0.116973	8.5489587
9	0.113052	8.8454568
10	0.090094	11.099492

Table 3.1. Modal periods and frequencies.

3.8. Static Pushover Analysis

3.8.1. Theory and purpose

The pushover analysis of a structure is a static non-linear analysis under permanent vertical loads and gradually increasing lateral loads. The equivalent static lateral loads approximately represent earthquake induced forces.

A plot of the total base shear versus top displacement in a structure is obtained by this analysis that would indicate any premature failure or weakness. The analysis is carried out up to failure, thus it enables determination of collapse load and ductility capacity. On a building frame, and plastic rotation is monitored, and lateral inelastic forces versus displacement response for the complete structure is analytically computed.

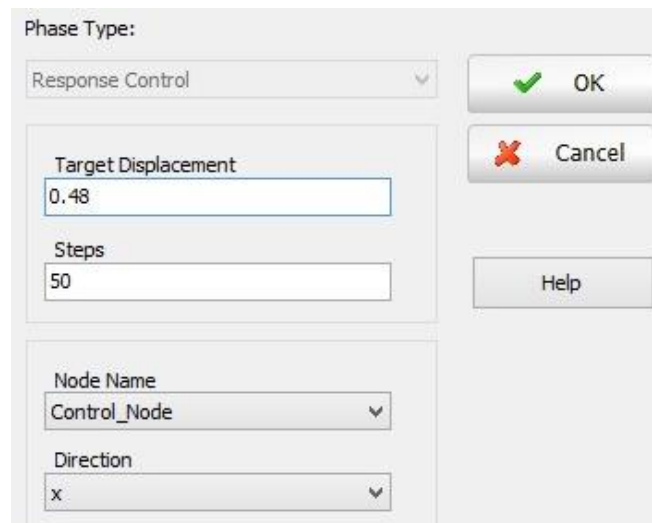
This type of analysis enables weakness in the structure to be identified. The decision to retrofit can be taken in such studies.

The purpose of pushover analysis is to evaluate the expected performance of structural systems by estimating its strength and deformation demands in design earthquakes by means of static inelastic analysis, and comparing these demands to available capacities at the performance levels of interest.

3.8.2. Static pushover in seismostruct

The applied incremental load P is kept proportional to the pattern of nominal loads (P_0) initially defined by the user: $P=\lambda P_0$. The load factor λ is automatically increased by the program until a user-defined limit, or numerical failure is reached.

For the incrementation of the loading factor, response control strategy is employed which refers to direct incrementation of the global displacement of one node “control node” and the calculation of the loading factor that corresponds to this displacement as shown in figure 3.20.



The screenshot shows a dialog box with the following fields and controls:

- Phase Type:** A dropdown menu set to "Response Control".
- Target Displacement:** A text input field containing "0.48".
- Steps:** A text input field containing "50".
- Node Name:** A dropdown menu set to "Control_Node".
- Direction:** A dropdown menu set to "x".
- Buttons:** "OK" (with a green checkmark), "Cancel" (with a red X), and "Help".

Figure 3.20. Phase type and control node target displacement.

The pushover loading type, and the performance criteria taken into consideration are illustrated in the figures below.

Loading Combination Coefficients		Performance Criteria		Code-based Checks	
Analysis Type		Frame Elements Modelling		Slabs Modelling	
		Structural Configuration			
Loading					
Analysis Type:					
Static pushover analysis					
Loading Type:					
Triangular distribution					
Control Node Definition					
<input checked="" type="checkbox"/> Do not define control node in floors with mass less than 10% of lower floor's mass					

Figure 3.21. Pushover analysis and loading type.

Criterion Name RFT_yield	Criterion Type Reinforcement Strain [RC/Composite sections] [User-defined limit]	Strength Degradation Keep Strength																																																				
Value 0.0025	Type of Notification <input type="radio"/> Stop <input type="radio"/> Pause <input checked="" type="radio"/> Notify <input type="radio"/> Inactive	Description (Reinforcement Strain [RC/Composite sections]) > 0.0025																																																				
Material All Steel Materials	Visual Display Color Identifier 																																																					
<table border="1"> <thead> <tr> <th colspan="4">Elements</th> </tr> </thead> <tbody> <tr><td><input checked="" type="checkbox"/> B10_1</td><td><input checked="" type="checkbox"/> B11_5</td><td><input checked="" type="checkbox"/> B13_1</td><td><input checked="" type="checkbox"/> B14_5</td></tr> <tr><td><input checked="" type="checkbox"/> B10_2</td><td><input checked="" type="checkbox"/> B11_6</td><td><input checked="" type="checkbox"/> B13_2</td><td><input checked="" type="checkbox"/> B14_6</td></tr> <tr><td><input checked="" type="checkbox"/> B10_3</td><td><input checked="" type="checkbox"/> B11_7</td><td><input checked="" type="checkbox"/> B13_3</td><td><input checked="" type="checkbox"/> B14_7</td></tr> <tr><td><input checked="" type="checkbox"/> B10_4</td><td><input checked="" type="checkbox"/> B11_8</td><td><input checked="" type="checkbox"/> B13_4</td><td><input checked="" type="checkbox"/> B14_8</td></tr> <tr><td><input checked="" type="checkbox"/> B10_5</td><td><input checked="" type="checkbox"/> B12_1</td><td><input checked="" type="checkbox"/> B13_5</td><td><input checked="" type="checkbox"/> B15_1</td></tr> <tr><td><input checked="" type="checkbox"/> B10_6</td><td><input checked="" type="checkbox"/> B12_2</td><td><input checked="" type="checkbox"/> B13_6</td><td><input checked="" type="checkbox"/> B15_2</td></tr> <tr><td><input checked="" type="checkbox"/> B10_7</td><td><input checked="" type="checkbox"/> B12_3</td><td><input checked="" type="checkbox"/> B13_7</td><td><input checked="" type="checkbox"/> B15_3</td></tr> <tr><td><input checked="" type="checkbox"/> B10_8</td><td><input checked="" type="checkbox"/> B12_4</td><td><input checked="" type="checkbox"/> B13_8</td><td><input checked="" type="checkbox"/> B15_4</td></tr> <tr><td><input checked="" type="checkbox"/> B11_1</td><td><input checked="" type="checkbox"/> B12_5</td><td><input checked="" type="checkbox"/> B14_1</td><td><input checked="" type="checkbox"/> B15_5</td></tr> <tr><td><input checked="" type="checkbox"/> B11_2</td><td><input checked="" type="checkbox"/> B12_6</td><td><input checked="" type="checkbox"/> B14_2</td><td><input checked="" type="checkbox"/> B15_6</td></tr> <tr><td><input checked="" type="checkbox"/> B11_3</td><td><input checked="" type="checkbox"/> B12_7</td><td><input checked="" type="checkbox"/> B14_3</td><td><input checked="" type="checkbox"/> B15_7</td></tr> <tr><td><input checked="" type="checkbox"/> B11_4</td><td><input checked="" type="checkbox"/> B12_8</td><td><input checked="" type="checkbox"/> B14_4</td><td><input checked="" type="checkbox"/> B15_8</td></tr> </tbody> </table>		Elements				<input checked="" type="checkbox"/> B10_1	<input checked="" type="checkbox"/> B11_5	<input checked="" type="checkbox"/> B13_1	<input checked="" type="checkbox"/> B14_5	<input checked="" type="checkbox"/> B10_2	<input checked="" type="checkbox"/> B11_6	<input checked="" type="checkbox"/> B13_2	<input checked="" type="checkbox"/> B14_6	<input checked="" type="checkbox"/> B10_3	<input checked="" type="checkbox"/> B11_7	<input checked="" type="checkbox"/> B13_3	<input checked="" type="checkbox"/> B14_7	<input checked="" type="checkbox"/> B10_4	<input checked="" type="checkbox"/> B11_8	<input checked="" type="checkbox"/> B13_4	<input checked="" type="checkbox"/> B14_8	<input checked="" type="checkbox"/> B10_5	<input checked="" type="checkbox"/> B12_1	<input checked="" type="checkbox"/> B13_5	<input checked="" type="checkbox"/> B15_1	<input checked="" type="checkbox"/> B10_6	<input checked="" type="checkbox"/> B12_2	<input checked="" type="checkbox"/> B13_6	<input checked="" type="checkbox"/> B15_2	<input checked="" type="checkbox"/> B10_7	<input checked="" type="checkbox"/> B12_3	<input checked="" type="checkbox"/> B13_7	<input checked="" type="checkbox"/> B15_3	<input checked="" type="checkbox"/> B10_8	<input checked="" type="checkbox"/> B12_4	<input checked="" type="checkbox"/> B13_8	<input checked="" type="checkbox"/> B15_4	<input checked="" type="checkbox"/> B11_1	<input checked="" type="checkbox"/> B12_5	<input checked="" type="checkbox"/> B14_1	<input checked="" type="checkbox"/> B15_5	<input checked="" type="checkbox"/> B11_2	<input checked="" type="checkbox"/> B12_6	<input checked="" type="checkbox"/> B14_2	<input checked="" type="checkbox"/> B15_6	<input checked="" type="checkbox"/> B11_3	<input checked="" type="checkbox"/> B12_7	<input checked="" type="checkbox"/> B14_3	<input checked="" type="checkbox"/> B15_7	<input checked="" type="checkbox"/> B11_4	<input checked="" type="checkbox"/> B12_8	<input checked="" type="checkbox"/> B14_4	<input checked="" type="checkbox"/> B15_8	Damage Visual Effects <input type="radio"/> None <input checked="" type="radio"/> Slight damage <input type="radio"/> Moderate damage <input type="radio"/> Serious damage <input type="radio"/> Very serious damage <input type="radio"/> Serious diagonal cracking <input type="radio"/> Delete element
Elements																																																						
<input checked="" type="checkbox"/> B10_1	<input checked="" type="checkbox"/> B11_5	<input checked="" type="checkbox"/> B13_1	<input checked="" type="checkbox"/> B14_5																																																			
<input checked="" type="checkbox"/> B10_2	<input checked="" type="checkbox"/> B11_6	<input checked="" type="checkbox"/> B13_2	<input checked="" type="checkbox"/> B14_6																																																			
<input checked="" type="checkbox"/> B10_3	<input checked="" type="checkbox"/> B11_7	<input checked="" type="checkbox"/> B13_3	<input checked="" type="checkbox"/> B14_7																																																			
<input checked="" type="checkbox"/> B10_4	<input checked="" type="checkbox"/> B11_8	<input checked="" type="checkbox"/> B13_4	<input checked="" type="checkbox"/> B14_8																																																			
<input checked="" type="checkbox"/> B10_5	<input checked="" type="checkbox"/> B12_1	<input checked="" type="checkbox"/> B13_5	<input checked="" type="checkbox"/> B15_1																																																			
<input checked="" type="checkbox"/> B10_6	<input checked="" type="checkbox"/> B12_2	<input checked="" type="checkbox"/> B13_6	<input checked="" type="checkbox"/> B15_2																																																			
<input checked="" type="checkbox"/> B10_7	<input checked="" type="checkbox"/> B12_3	<input checked="" type="checkbox"/> B13_7	<input checked="" type="checkbox"/> B15_3																																																			
<input checked="" type="checkbox"/> B10_8	<input checked="" type="checkbox"/> B12_4	<input checked="" type="checkbox"/> B13_8	<input checked="" type="checkbox"/> B15_4																																																			
<input checked="" type="checkbox"/> B11_1	<input checked="" type="checkbox"/> B12_5	<input checked="" type="checkbox"/> B14_1	<input checked="" type="checkbox"/> B15_5																																																			
<input checked="" type="checkbox"/> B11_2	<input checked="" type="checkbox"/> B12_6	<input checked="" type="checkbox"/> B14_2	<input checked="" type="checkbox"/> B15_6																																																			
<input checked="" type="checkbox"/> B11_3	<input checked="" type="checkbox"/> B12_7	<input checked="" type="checkbox"/> B14_3	<input checked="" type="checkbox"/> B15_7																																																			
<input checked="" type="checkbox"/> B11_4	<input checked="" type="checkbox"/> B12_8	<input checked="" type="checkbox"/> B14_4	<input checked="" type="checkbox"/> B15_8																																																			

infrmFB, infrmFBPH and infrmDB elements only...

Figure 3.22. Yield reinforcement performance criterion



Criterion Name:

Criterion Type: Frame Element Chord Rotation Capacity [Automatically-defined limit]

Value:

Equation: EC8, Part3, A.3.2.2: equation (A.1)

NOTE: **Mean material values** and **no safety or confidence factors** will be used in the calculations

Strength Degradation: Keep Strength

Type of Notification: Stop Pause Notify Inactive

Description: (Frame Element Chord Rotation) < Calculated mean value

Elements

<input checked="" type="checkbox"/> B10_1	<input checked="" type="checkbox"/> B11_5	<input checked="" type="checkbox"/> B13_1	<input checked="" type="checkbox"/> B14_5
<input checked="" type="checkbox"/> B10_2	<input checked="" type="checkbox"/> B11_6	<input checked="" type="checkbox"/> B13_2	<input checked="" type="checkbox"/> B14_6
<input checked="" type="checkbox"/> B10_3	<input checked="" type="checkbox"/> B11_7	<input checked="" type="checkbox"/> B13_3	<input checked="" type="checkbox"/> B14_7
<input checked="" type="checkbox"/> B10_4	<input checked="" type="checkbox"/> B11_8	<input checked="" type="checkbox"/> B13_4	<input checked="" type="checkbox"/> B14_8
<input checked="" type="checkbox"/> B10_5	<input checked="" type="checkbox"/> B12_1	<input checked="" type="checkbox"/> B13_5	<input checked="" type="checkbox"/> B15_1
<input checked="" type="checkbox"/> B10_6	<input checked="" type="checkbox"/> B12_2	<input checked="" type="checkbox"/> B13_6	<input checked="" type="checkbox"/> B15_2
<input checked="" type="checkbox"/> B10_7	<input checked="" type="checkbox"/> B12_3	<input checked="" type="checkbox"/> B13_7	<input checked="" type="checkbox"/> B15_3
<input checked="" type="checkbox"/> B10_8	<input checked="" type="checkbox"/> B12_4	<input checked="" type="checkbox"/> B13_8	<input checked="" type="checkbox"/> B15_4
<input checked="" type="checkbox"/> B11_1	<input checked="" type="checkbox"/> B12_5	<input checked="" type="checkbox"/> B14_1	<input checked="" type="checkbox"/> B15_5
<input checked="" type="checkbox"/> B11_2	<input checked="" type="checkbox"/> B12_6	<input checked="" type="checkbox"/> B14_2	<input checked="" type="checkbox"/> B15_6
<input checked="" type="checkbox"/> B11_3	<input checked="" type="checkbox"/> B12_7	<input checked="" type="checkbox"/> B14_3	<input checked="" type="checkbox"/> B15_7
<input checked="" type="checkbox"/> B11_4	<input checked="" type="checkbox"/> B12_8	<input checked="" type="checkbox"/> B14_4	<input checked="" type="checkbox"/> B15_8

Visual Display

Color Identifier:

Damage Visual Effects

- None
- Slight damage
- Moderate damage
- Serious damage
- Very serious damage
- Serious diagonal cracking
- Delete element

nfrmFB, nfrmFBPH, nfrmDB and nfrmDBPH elements with the rcrs, rccs, rlcbs, rctcs, rcts, rcars, rcrrs, rcrlcs, rcrtcs, rcjcs, rcjts and rcjars section types...

Figure 3.23. Chord rotation capacity performance criterion.

Criterion Name:

Criterion Type: Frame Element Shear Capacity [Automatically-defined limit]

Value:

Equation: EC8, Part3, A.3.3.1: equation (A.12)

NOTE: **Mean material values** and **no safety or confidence factors** will be used in the calculations

Strength Degradation: Keep Strength

Type of Notification: Stop Pause Notify Inactive

Description: (Frame Element Shear force) < Calculated mean value

Elements

<input checked="" type="checkbox"/> B10_1	<input checked="" type="checkbox"/> B11_5	<input checked="" type="checkbox"/> B13_1	<input checked="" type="checkbox"/> B14_5
<input checked="" type="checkbox"/> B10_2	<input checked="" type="checkbox"/> B11_6	<input checked="" type="checkbox"/> B13_2	<input checked="" type="checkbox"/> B14_6
<input checked="" type="checkbox"/> B10_3	<input checked="" type="checkbox"/> B11_7	<input checked="" type="checkbox"/> B13_3	<input checked="" type="checkbox"/> B14_7
<input checked="" type="checkbox"/> B10_4	<input checked="" type="checkbox"/> B11_8	<input checked="" type="checkbox"/> B13_4	<input checked="" type="checkbox"/> B14_8
<input checked="" type="checkbox"/> B10_5	<input checked="" type="checkbox"/> B12_1	<input checked="" type="checkbox"/> B13_5	<input checked="" type="checkbox"/> B15_1
<input checked="" type="checkbox"/> B10_6	<input checked="" type="checkbox"/> B12_2	<input checked="" type="checkbox"/> B13_6	<input checked="" type="checkbox"/> B15_2
<input checked="" type="checkbox"/> B10_7	<input checked="" type="checkbox"/> B12_3	<input checked="" type="checkbox"/> B13_7	<input checked="" type="checkbox"/> B15_3
<input checked="" type="checkbox"/> B10_8	<input checked="" type="checkbox"/> B12_4	<input checked="" type="checkbox"/> B13_8	<input checked="" type="checkbox"/> B15_4
<input checked="" type="checkbox"/> B11_1	<input checked="" type="checkbox"/> B12_5	<input checked="" type="checkbox"/> B14_1	<input checked="" type="checkbox"/> B15_5
<input checked="" type="checkbox"/> B11_2	<input checked="" type="checkbox"/> B12_6	<input checked="" type="checkbox"/> B14_2	<input checked="" type="checkbox"/> B15_6
<input checked="" type="checkbox"/> B11_3	<input checked="" type="checkbox"/> B12_7	<input checked="" type="checkbox"/> B14_3	<input checked="" type="checkbox"/> B15_7
<input checked="" type="checkbox"/> B11_4	<input checked="" type="checkbox"/> B12_8	<input checked="" type="checkbox"/> B14_4	<input checked="" type="checkbox"/> B15_8

Visual Display

Color Identifier:

Damage Visual Effects

- None
- Slight damage
- Moderate damage
- Serious damage
- Very serious damage
- Serious diagonal cracking
- Delete element

nfrmFB, nfrmFBPH, nfrmDB and nfrmDBPH elements - only the sections that allow shear capacity checks (see Sections module).

Figure 3.24. Shear capacity performance criterion.

Criterion Name:

OK

Cancel

Help

Criterion Type:

Value:

Equation:

NOTE: Mean material values and no safety or confidence factors will be used in the calculations

Strength Degradation:

Type of Notification: Stop Pause Notify Inactive

Description: (Frame Element Chord Rotation) < Calculated mean value

Elements

<input checked="" type="checkbox"/> B10_1	<input checked="" type="checkbox"/> B11_5	<input checked="" type="checkbox"/> B13_1	<input checked="" type="checkbox"/> B14_5
<input checked="" type="checkbox"/> B10_2	<input checked="" type="checkbox"/> B11_6	<input checked="" type="checkbox"/> B13_2	<input checked="" type="checkbox"/> B14_6
<input checked="" type="checkbox"/> B10_3	<input checked="" type="checkbox"/> B11_7	<input checked="" type="checkbox"/> B13_3	<input checked="" type="checkbox"/> B14_7
<input checked="" type="checkbox"/> B10_4	<input checked="" type="checkbox"/> B11_8	<input checked="" type="checkbox"/> B13_4	<input checked="" type="checkbox"/> B14_8
<input checked="" type="checkbox"/> B10_5	<input checked="" type="checkbox"/> B12_1	<input checked="" type="checkbox"/> B13_5	<input checked="" type="checkbox"/> B15_1
<input checked="" type="checkbox"/> B10_6	<input checked="" type="checkbox"/> B12_2	<input checked="" type="checkbox"/> B13_6	<input checked="" type="checkbox"/> B15_2
<input checked="" type="checkbox"/> B10_7	<input checked="" type="checkbox"/> B12_3	<input checked="" type="checkbox"/> B13_7	<input checked="" type="checkbox"/> B15_3
<input checked="" type="checkbox"/> B10_8	<input checked="" type="checkbox"/> B12_4	<input checked="" type="checkbox"/> B13_8	<input checked="" type="checkbox"/> B15_4
<input checked="" type="checkbox"/> B11_1	<input checked="" type="checkbox"/> B12_5	<input checked="" type="checkbox"/> B14_1	<input checked="" type="checkbox"/> B15_5
<input checked="" type="checkbox"/> B11_2	<input checked="" type="checkbox"/> B12_6	<input checked="" type="checkbox"/> B14_2	<input checked="" type="checkbox"/> B15_6
<input checked="" type="checkbox"/> B11_3	<input checked="" type="checkbox"/> B12_7	<input checked="" type="checkbox"/> B14_3	<input checked="" type="checkbox"/> B15_7
<input checked="" type="checkbox"/> B11_4	<input checked="" type="checkbox"/> B12_8	<input checked="" type="checkbox"/> B14_4	<input checked="" type="checkbox"/> B15_8

Visual Display

Color Identifier:

Damage Visual Effects:

None

Slight damage

Moderate damage

Serious damage

Very serious damage

Serious diagonal cracking

Delete element

nfrmFB, nfrmFBPH, nfrmDB and nfrmDBPH elements with the rcrs, rccs, rclcs, rctcs, rcts, rcars, rcrrs, rcjrs, rcjclcs, rcjctcs, rcjcs, rcjts and rcjars section types...

Figure 3.25. Chord rotation yielding performance criterion.

The resulting pushover curves in X and Y directions, in terms of Base Shear vs. Roof Displacement (V-Δ), are shown in Figures 3.26 and 3.27 respectively. The slope of the pushover curves is gradually reduced with the increase of the lateral displacement of the building.

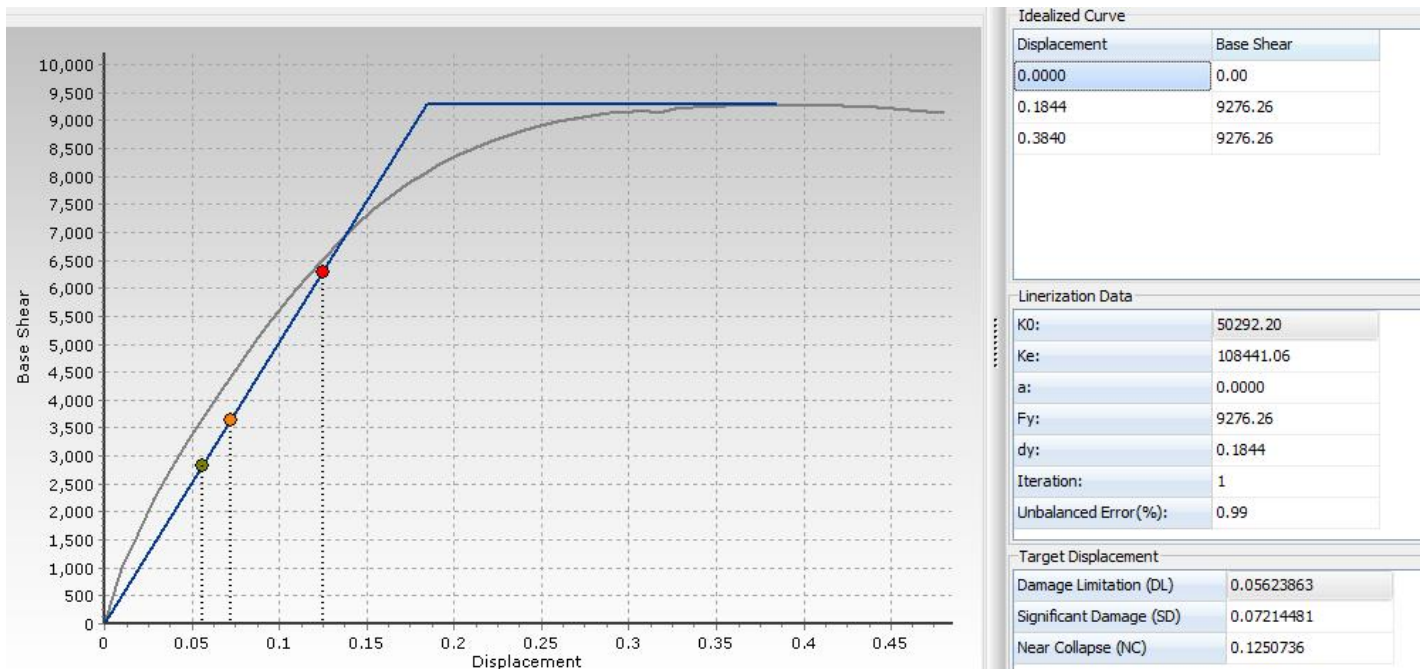


Figure 3.26. Pushover capacity curve in X-direction.

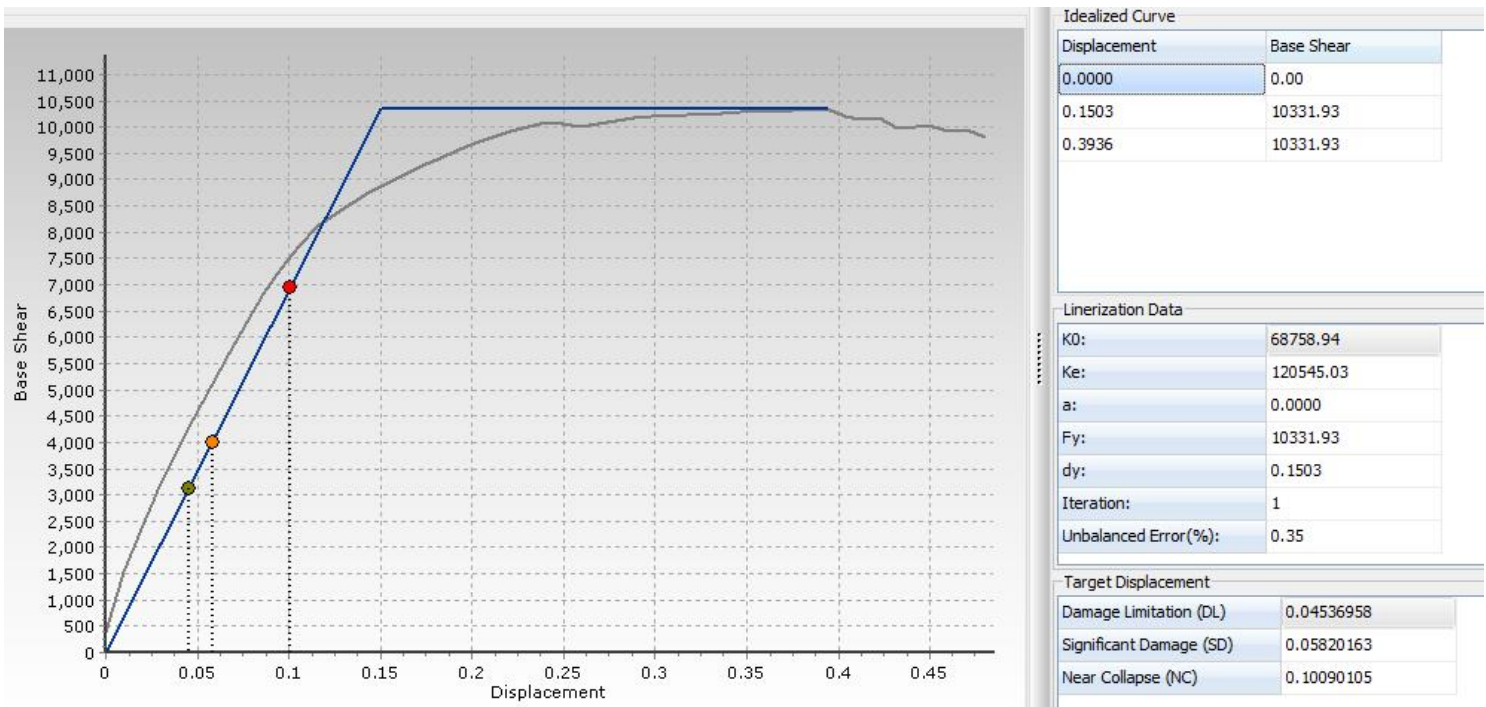


Figure 3.27. Pushover capacity curve in Y-direction.

CHAPTER 4 GROUND MOTIONS RECORDS

In this study, two seismic regions including near-fault phenomenon were examined which are:

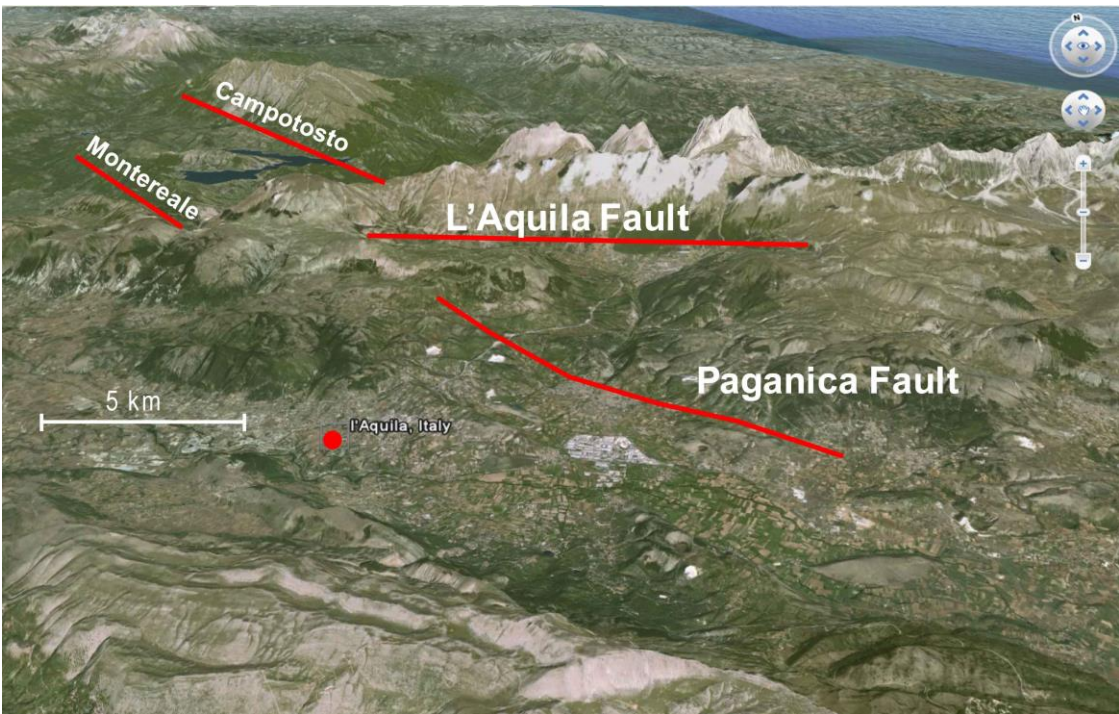
- 1) L'Aquila Earthquake 2009
- 2) Norcia Earthquake 2016

4.1. L'Aquila earthquake 2009:

L'Aquila earthquake of 2009, severe earthquake that occurred on April 6, 2009, near the city of L'Aquila in the Abruzzi region of central Italy.

The magnitude-6.3 on moment magnitude scale earthquake struck at 3:32 am local time, extensively damaging the 13th-century city of L'Aquila, located only about 60 miles (100 km) northeast of Rome. The earthquake resulted from normal faulting on the northwest-southeast-trending Paganica Fault. It and several neighboring faults are related to extensional tectonic forces associated with the opening of the Tyrrhenian Basin to the west. For more than three months after the main earthquake, the National Institute of Geophysics and Volcanology, using a portable network of seismometers, continued to detect thousands of aftershocks. The aftershocks from the country's worst earthquake in 30 years rippled through central Italy, fraying both public and political nerves. In all, more than 300 people died, and an estimated 60,000 were left homeless.





Pictures representing the damage after the L'Aquila earthquake and the geography of the region

Near Source Features

Results of seismological studies have shown that the Abruzzi event was a *normal* faulting earthquake (or *dip-slip*), with a rectangular rupture plane of about 17×14km² and located at a depth between 12 and 0.6 km from the surface. The rupture plan has a strike of 142°, a dip of 50° and a rake of 90°.

Coordinates of the vertices of the rupture plane and of the hypocenter are reported in Table 4.1. These data are not uniquely identified by all seismologists, but the various available estimates are not very different each other. The main shock was recorded by the stations of the National Accelerometric Network (RAN) of the Italian Civil Protection, Figure 4.1 shows the projection of rupture surface with the epicentral location, the code of RAN Stations, their Eurocode 8 (EC8) site class, and some severely damaged towns and villages.

	Fault plane vertices				Hypocenter
Longitude	13.424°	13.552°	13.465°	13.336°	13.353°
Latitude	42.405°	42.293°	42.238°	42.351°	42.340°
Depth (km)	0.600	0.600	11.800	11.800	11.800

Table 4.1. Hypocenter and rupture plane coordinates.

NEAR-SOURCE SEISMIC DEMAND AND PULSE-LIKE RECORDS

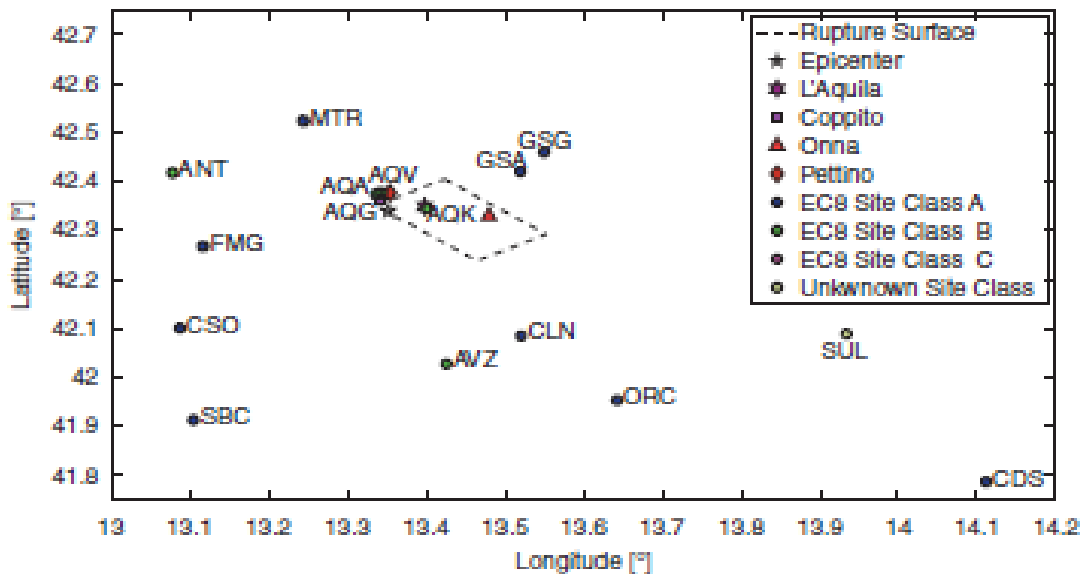


Figure 4.1. Map view of rupture surface and RAN Accelerometric stations within about 60 km from the fault projection.



The algorithm developed by Baker calculates, for each record, a score called *pulse indicator*. Records with score above 0.85 and below 0.15 are classified as pulses and non-pulses, respectively, while signals with a score between these limits are considered ambiguous. The procedure to identify pulses has been implemented by J.W. Baker was used to analyze L'Aquila records; Table VII shows the results of pulse identification for the records of Table VI; identified pulse-like records are reported in bold. Thirteen stations were analyzed and seven of them have a horizontal component classified as pulse-like: six of them in the FN direction and only one in the FP direction, AQV.

	Record	PGA (cm/s ²)	PGV (cm/s)	PGD* (cm)	A _I (cm/s)	I _D (-)	S _D (s)	B _D (s)
1	AQV_FN	725.37	37.63	5.53	228.76	5.24	7.69	25.14
	AQV_FP	474.42	31.41	7.07	253.90	10.64	7.61	66.41
2	AQG_FN	357.16	34.08	8.19	114.47	5.88	8.16	18.23
	AQG_FP	391.79	26.60	5.45	144.91	8.68	8.45	25.17
3	AQA_FN	425.86	28.67	7.11	132.60	6.79	6.91	14.78
	AQA_FP	404.55	19.91	3.32	198.89	15.50	7.72	67.33
4	AQK_FN	413.57	45.01	13.22	138.10	4.63	10.55	66.06
	AQK_FP	261.99	16.66	5.32	81.96	11.73	15.37	66.51
5	GSA_FN	153.52	10.91	3.35	37.13	13.86	9.38	25.53
	GSA_FP	197.58	6.02	1.37	46.50	24.48	8.02	24.10
6	CLN_FN	99.54	5.48	1.76	3.87	4.43	8.00	20.05
	CLN_FP	63.29	5.82	2.26	3.75	6.37	6.53	19.13
7	AVZ_FN	61.91	13.06	3.40	8.43	6.51	21.56	51.28
	AVZ_FP	63.41	9.89	3.54	9.14	9.10	18.25	49.76
8	MTR_FN	51.04	4.08	0.93	4.02	12.04	14.84	45.93
	MTR_FP	57.19	3.04	0.88	5.17	18.59	11.39	34.84
9	GSG_FN	20.31	3.66	2.14	0.81	6.81	10.65	33.28
	GSG_FP	25.52	2.31	0.71	0.69	7.33	10.97	25.59
10	FMG_FN	21.87	2.12	0.98	1.34	18.12	22.76	60.38
	FMG_FP	24.43	1.90	0.92	0.88	11.87	20.58	41.78
11	ANT_FN	26.66	2.25	0.47	1.67	17.33	21.68	54.48
	ANT_FP	19.19	1.99	0.43	0.96	15.74	22.87	64.52
12	CSO_FN	18.91	2.24	1.00	0.89	13.11	21.38	58.06
	CSO_FP	13.74	1.48	0.43	0.48	14.74	27.23	65.69
13	ORC_FN	72.64	6.88	1.11	4.77	5.97	10.24	30.10
	ORC_FP	31.85	2.86	0.99	1.83	12.60	14.00	50.95

Table 4.2. Peak and integral IMs of L'Aquila near-source records.

Component	Pulse indicator	Late pulse indicator	PGV (cm/s)	Classified as pulse	T _p (s)
AQV_FN	0.70	0.00	37.63	No	0.53
AQV_FP	0.85	0.00	31.41	Yes	1.06
AQG_FN	1.00	0.00	34.08	Yes	1.02
AQG_FP	0.71	0.00	26.60	No	1.11
AQA_FN	0.93	0.00	28.67	Yes	0.74
AQA_FP	0.00	0.00	19.91	No	0.62
AQK_FN	1.00	0.00	45.01	Yes	1.99
AQK_FP	0.00	1.00	16.66	No	1.26

Table 4.3. Results of pulse identification for horizontal components.

4.2. Norcia earthquake 2016:

Norcia Earthquake was the most powerful earthquake to hit Italy since 1980, striking a blow to the regions of Marche and Umbria just days after they were hit by two other earthquakes. It was even more powerful than the April 2009 earthquake that hit L'Aquila, killing more than 300 people, and worse than the August 2016 earthquake that killed hundreds in Amatrice. It also frightened and displaced thousands of already-jittery residents who have seen the ancient structures and walls in their towns, including the San Benedetto basilica in Norcia, which is considered a sacred site, crumble into heaps on the street. The epicenter of the latest earthquake was about 40 miles (68km) south-west of Perugia and close to the town of Norcia, which had also been hit by previous earthquakes.





Pictures representing the damage after the Norcia earthquake and the geography of the region

About 650 Accelerometric signals, manually processed using the procedure by Paolucci et al (2011), are used to evaluate the peak ground motion, acceleration and displacement spectral ordinates, integral parameters and measures of duration.

The first strong earthquake of the sequence (Mw 6.0) struck central Italy on 24-08-2016 at 01:36:32 GMT, in the vicinity of Amatrice, causing diffuse building collapse and about 300 casualties. After 2 months, on 26-10-2016 two events of moment magnitude 5.4 (17:10:36 UTC) and 5.9 (19:18:06 UTC) extended to the NW the seismogenic volume. After 4 days, on 30-10-2016 at 06:40:18 UTC an event of Mw 6.5, struck the area corresponding to the Sibillini Mountains with epicenter located in the vicinity of Norcia.

The four events have been caused by normal faulting, the prevalent style of faulting in the area, all of them having NW-SE or NNW-SSE strike and dip towards SW. The location of the three epicenters together with events having magnitude larger than 4.0 is shown in Fig 4.2.

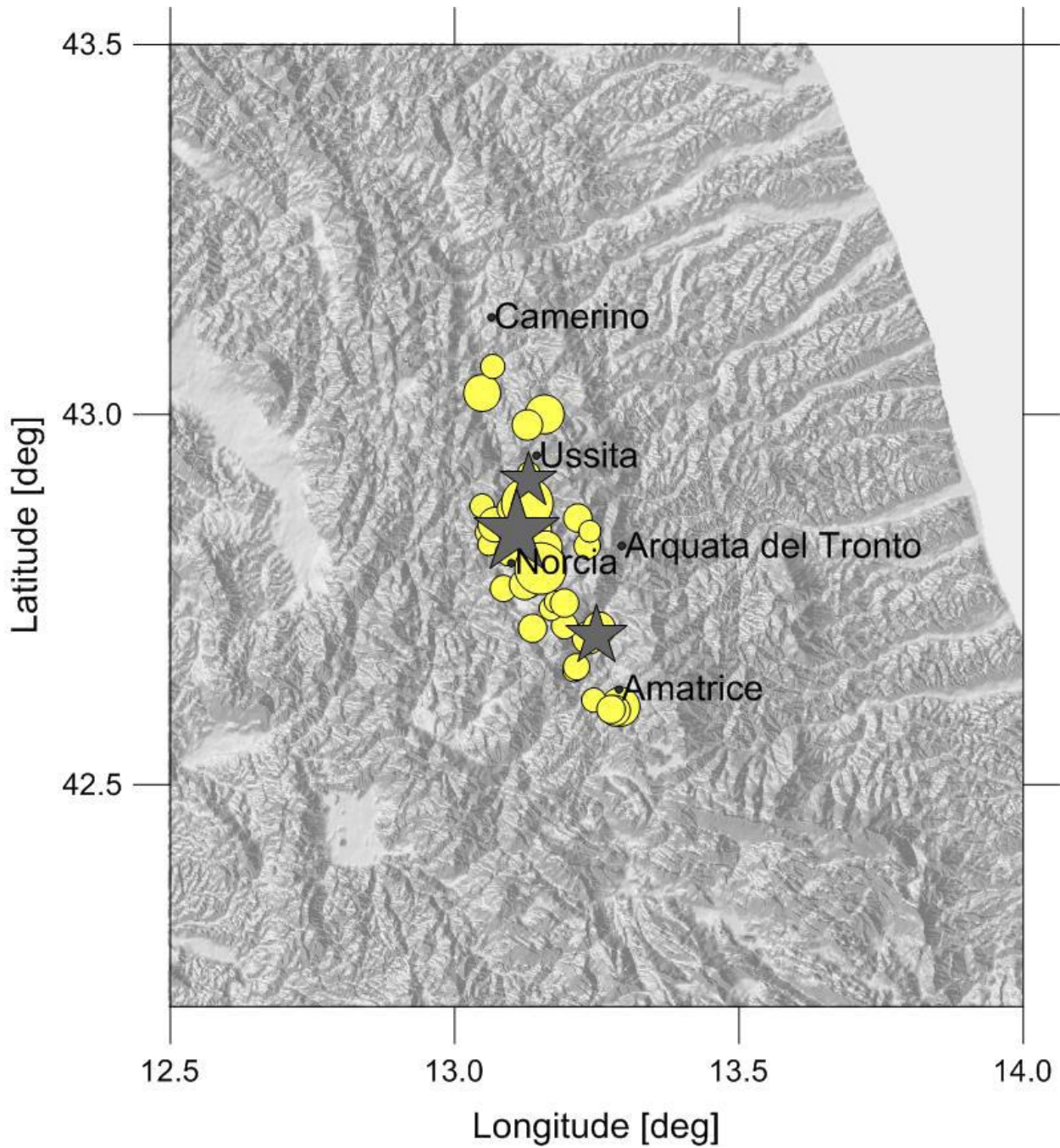


Figure 4.2: Epicenters of the events with $M \geq 4.0$ in period time from 24-08-2016 to 3-11-2016. The size of the symbols is proportional to the magnitude. The grey stars represent the three main-shocks: Amatrice, 24-08-2016, Mw 6.0; Ussita, 28-10-2016, Mw 5.9 and Norcia, 30-10-2016, Mw 6.5 (coordinates from <http://cnt.rm.ingv.it/>).

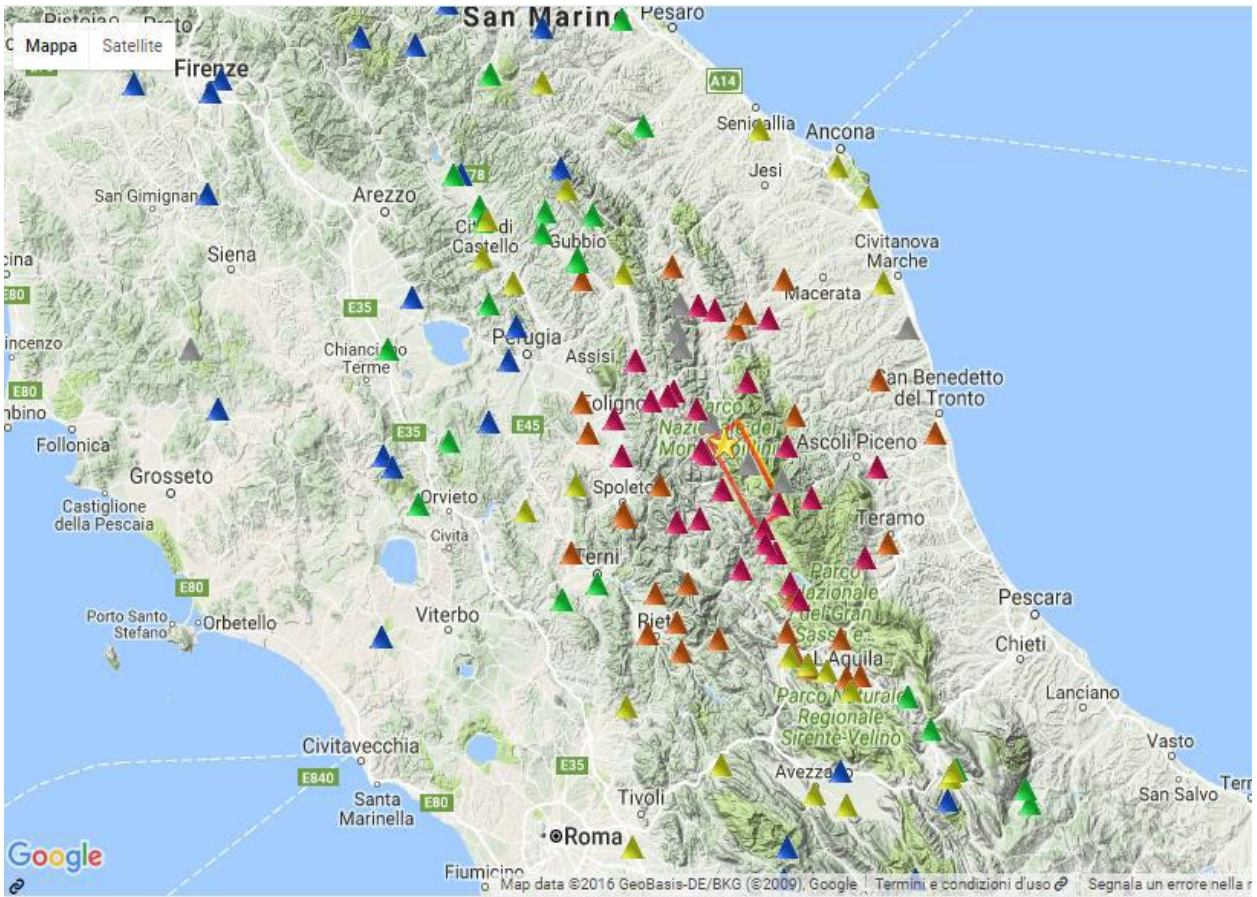


Figure 4.3. Location of the epicenters (yellow star) and strong motion stations within 150 km from the epicenter of a) 2016-08-24 Mw 6.0; b) 2016-10-26 Mw 5.9; c) 2016-10-30 Mw 6.5. The triangles indicate strong-motion stations and the colors correspond to the PGA values (gal). The red boxes are the surface fault projections: the fault geometries are preliminary for the Ussita and Norcia events.

A map of the various epicenters along with the stations for which notable pulses we detected in the strike-normal (fault-normal, FN) component, can be seen in Figure 4.4 (note that no impulsive ground motions were detected in the case of the 26/10/2016 Mw5.9 shock).

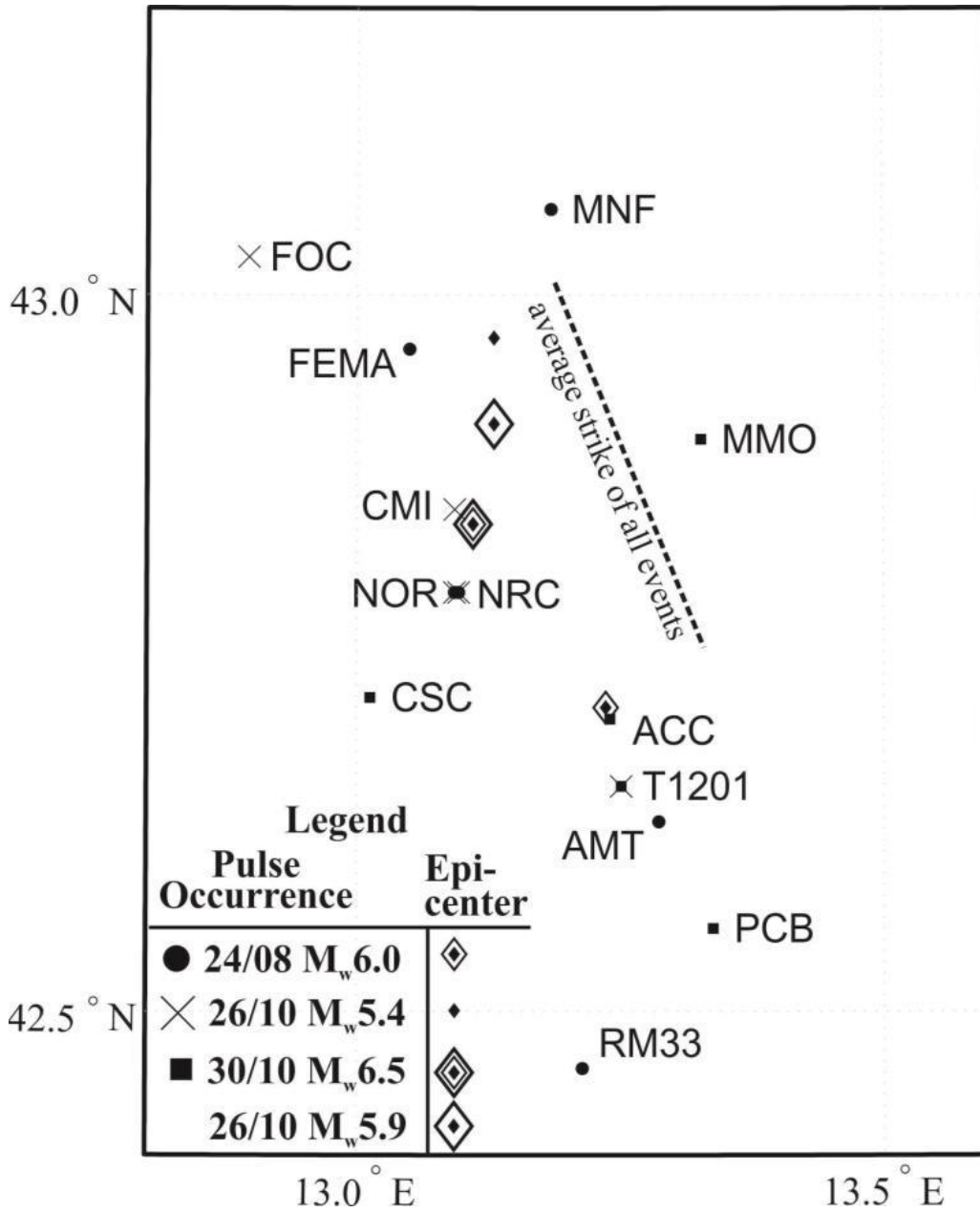


Figure 4.4. Surface projection of rupture plane; province borders and some NS stations shown on the map.

Out of all the records investigated belonging to the 24/08/2016 Mw6.0 shock, the six ground motions recorded at Amatrice (AMT), Norcia (NRC), Norcia Le Castellina (NOR), Montreal (RM33), Monte Fema (FEMA) and Fiastra (MNF) exhibited impulsive characteristics over a multitude of orientations, as expressed by a Pulse Indicator (PI) score in excess of 0.85 (see Baker, 2007). The record at Amatrice revealed two distinct pulses, one being predominant in the fault-normal (FN) and the other longer pulse in the fault-parallel (FP) direction. The FN pulse has a pulse period T_p of 0.40s while the FP 0.98s. The Norcia record on the other hand was found to contain a 2.09s period pulse mostly towards orientations that lie between the FN and FP without being decidedly prevalent in any of the perpendicular/parallel directions to the strike. Note that some deviation of directivity pulses from the strictly FN orientation is not unheard of in dip-slip faulting. Finally, the ground motions recorded at the stations of Fiastra and Montreal were found to contain pulses in the FN direction with T_p of 1.4s and 1.2s respectively, also hinting at rupture directivity effects, despite the lower velocity amplitude due to the greater distance from the fault and consequent attenuation.

In the following Figures, a polar plot is presented for each station displaying the PI score per azimuth as well as the velocity time histories at the most relevant directions (original signal and extracted pulse superimposed).

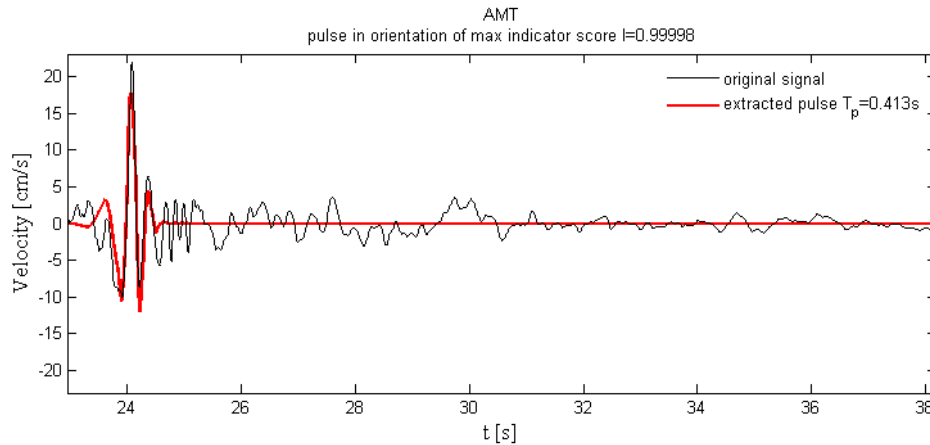


Figure 4.5 Original velocity time-history and CWT extracted pulse and residual signal for the fault-normal component of the Amatrice record - 24/08/2016 Mw6.0 event.

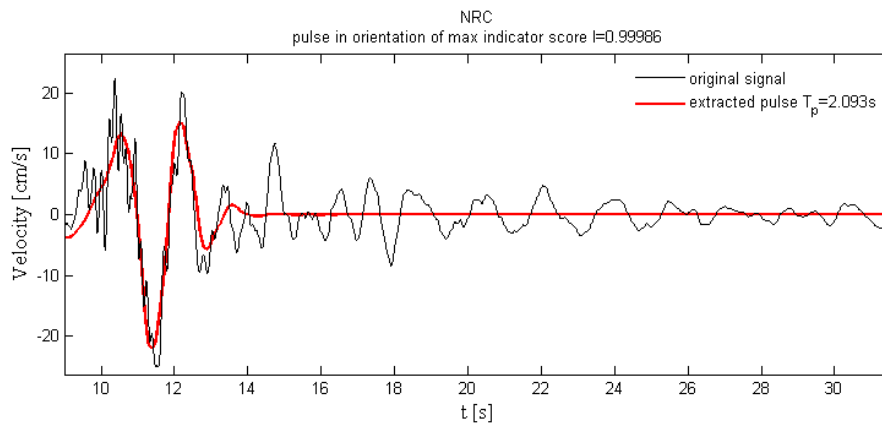


Figure 4.6 Original velocity time-history and CWT extracted pulse and residual signal for the fault-normal component of the Norcia (NRC) record - 24/08/2016 Mw6.0 event.

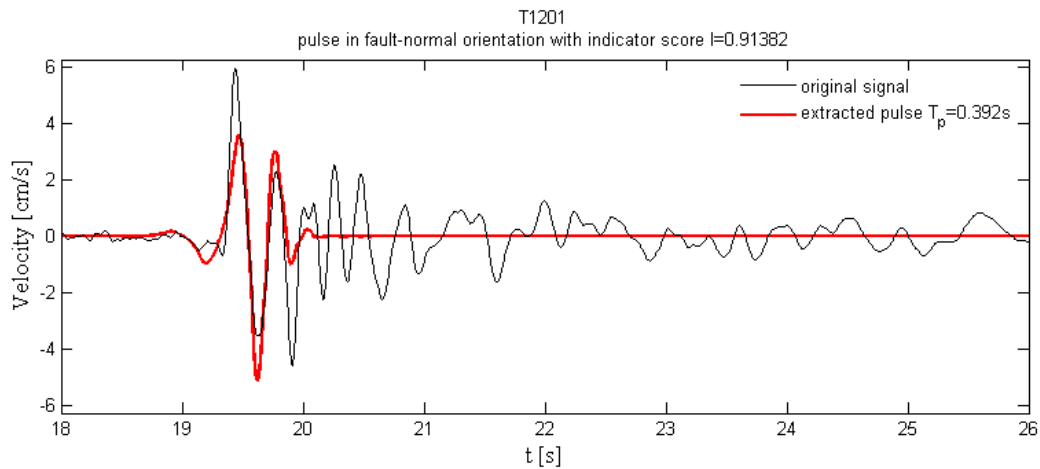


Figure 4.7 Original velocity time-history and CWT extracted pulse and residual signal for the fault-normal component of the mobile station T1201 record - 26/10/2016 Mw5.4 event.

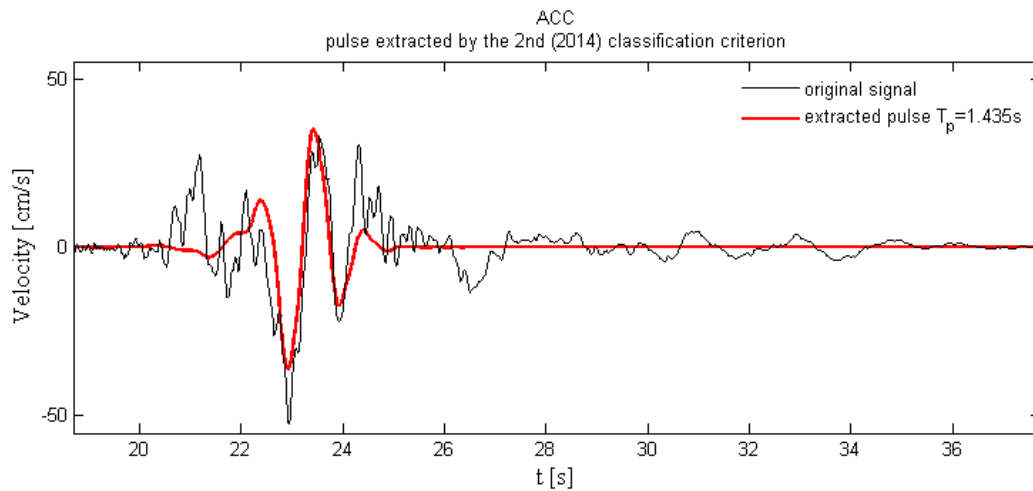


Figure 4.8 Original velocity time-history and CWT extracted pulse and residual signal for the quasi-fault-normal component of the Accumoli record - 30/10/2016 Mw6.5 event.



CHAPTER 5 SEISMIC DESIGN OF RC SHEAR WALL STRUCTURES IN CHILE

5.1. Introduction

Reinforced concrete buildings utilizing structural walls for lateral load resistance are the predominant form of construction in Chile for buildings over four stories. Typical buildings include a large number of walls, with ratios of wall cross-sectional area to floor plan area of roughly 3% in each principal direction.

Based on the good performance of RC buildings in the March 1985 earthquake, requirements for closely spaced transverse reinforcement at wall boundaries were excluded when Chile adopted a new concrete code in 1996 based on ACI 318-95.

In recent years, use of three-dimensional linear models along with modal response spectrum analysis has become common. Since 1985, nearly 10,000 new buildings have been permitted. Although the newer buildings have similar wall area to floor plan areas as older buildings, newer walls are thinner and buildings are taller, leading to significantly higher wall axial load ratios.

The 3 March 1985 Ms 7.8 earthquake in Chile, which subjected approximately 400 modern reinforced concrete (RC) buildings to strong shaking, led to important changes in U.S. code provisions for reinforced concrete buildings. Reconnaissance reports (EERI 1986) and subsequent studies (Wallace and Moehle 1989) indicated that the stiff, shear wall structures constructed in Chile performed extremely well, with little to no apparent damage in the majority of buildings. Later investigations (Wallace and Moehle 1992, 1993) revealed that although the seismic code requirements (design forces) in Chile were similar to those used for high seismic regions in the United States, detailing requirements were less stringent due to the large number of structural walls used.

Building codes in Chile also changed following the 1985 earthquake with the adoption of a new code in 1996 (NCh433.Of96; INN 1996). Analysis procedures for earthquake loads in NCh433 are the same as used in other modern codes, that is, the equivalent static lateral force and modal response spectrum procedures used in ASCE 7-10 (2010). As well, design requirements for RC shear wall buildings, the predominant form of construction in Chile for buildings over four stories, were updated by reference to ACI 318-95 in NCh433.Of96 (INN 1996), with only minor exceptions. Prior codes used for design of RC buildings, NCh429.Of57 and NCh430.Of61, were not updated. The code provisions for shear walls are essentially the same as those in ACI 318-95; however, based on the good performance of wall buildings in Viña del Mar in the 1985 earthquake, ACI 318-95 requirements for special transverse reinforcement at wall boundaries to confine the concrete and restrain rebar bucking were eliminated. The most recent code for RC buildings, NCh430.Of2008 (INN 2008), refers to ACI 318-05, but does not exclude the provisions that require special boundary elements. Given the lag in release of a new code and its use in practice, few, if any, of the buildings impacted by the earthquake were designed to the new code.



The area impacted by the Mw 8.8 2010 earthquake is the most densely populated region of Chile and includes the cities of Viña del Mar, Santiago, and Concepción. Between 1985 and 2009, construction permits were issued for 9,974 residential buildings with three or more floors (CChC 2010); 65% of permits were issued within the Metropolitan Region of Chile (Santiago). A total of 1,939 construction permits were issued for reinforced concrete buildings with nine or more floors during the same period, with 68% issued within the Metropolitan Region. In general, prior to 1985, a majority of taller RC buildings were less than 15 stories, whereas since 1990 construction of residential buildings greater than 15 stories became more common. Damage observed following the earthquake was generally concentrated in newer and taller buildings, with one complete collapse (Alto Río Building), several partial collapses, and about 40 severely damaged buildings that were either repaired, or in rare cases, demolished. Therefore, severely damaged reinforced concrete buildings correspond to about 2% (40/1,939) of the newer building stock with 9 or more floors in south-central Chile. If older and/or shorter buildings are included, the percentage of severely damaged buildings drops substantially.

Given this history, the 27 February 2010 Mw 8.8 Chile earthquake provides a unique opportunity to assess the performance of reinforced concrete buildings designed using modern codes. Preliminary observations (EERI 2010) indicate relatively few people lost their lives in modern reinforced concrete buildings; however, the degree of damage exceeded that reported following the 1985 earthquake. In the following, we review building code provisions and construction practices used in Chile and briefly compare earthquake demands relative to the design requirements.

5.2. Building code provisions in Chile

Service-level design lateral forces and analysis procedures for buildings are defined in NCh433.0f96 (INN 1996). Similar to ASCE 7-10 (2010), design spectra are defined based on proximity to the fault zone, soil conditions, and structural system behavior. The pseudo-spectral acceleration is defined as:

$$S_a = \frac{IA_0\alpha}{R^*} \quad (1)$$

$$\alpha = \frac{1 + 4.5 \left(\frac{T_n}{T_0}\right)^p}{1 + \left(\frac{T_n}{T_0}\right)^3} \quad (2)$$

$$R^* = 1 + \frac{T^*}{0.1T_0 + \frac{T^*}{R_0}} \quad (3)$$



Where I is an importance factor (equal to 1.0 for common structures), A_0 is the maximum effective acceleration, T_n is the natural period, T^* is the period with the largest translational equivalent mass, and R^* is a period dependent reduction factor which can be calculated for shear wall buildings using the relation in Equation 3. Alternatively, R^* can be estimated as $R^* = 1 + NR_0 / (4T_0R_0 + N)$, where N is the number of stories and $R_0 = 11$ for reinforced shear wall buildings; however, the effective R^* is considerably lower due to minimum strength requirements, as discussed below. Values for other parameters in Equation 2 depend on soil conditions, of which there are four defined in NCh433.Of96 (INN 1996). The most common soil conditions are II and III, with the following values for Type II: $S = 1.0$, $T_0 = 0.3$, and $p = 1.5$ and Type III: $S = 1.20$, $T_0 = 0.75$, and $p = 1.0$. Zone 3, along the coast, has the highest maximum effective acceleration A_0 of 0.4 g, whereas values for Zones 2 and 1 are 0.3 g and 0.2 g, respectively. Viña del Mar and Concepción are in Zone 3, whereas Santiago is in Zone 2. Code displacement spectra are plotted later and compared with spectra for various recorded ground motions.

Four soil types are defined using soil test data, such as soil shear wave velocity (v_s), rock quality designation (RQD), standard penetration test (SPT), uniaxial compression capacity (q_u), and undrained shear strength (S_u), among other considerations. However, various alternative approaches exist to characterize soil; for example, for Soil Types II and III, four alternatives exist, and soils may be classified based on values achieved in only one of the test approaches. Given variation among the various testing approaches, different soil classifications are possible depending on the approach used. Design level forces are quite sensitive to soil type classification, providing some incentive to use a soil classification approach that would produce a lower soil classification number.

Design of most RC buildings over five stories is accomplished using the modal spectral procedure of NCh433.Of96 (INN 1996). Limits are placed on base shear (Section 6.3.7), which cannot be less than $IA_0P/6g$, and need not exceed $IC_{max}P$, where C_{max} is $0.35SA_0/g$ for RC wall buildings, and P is the total seismic weight of the building (total dead load and a minimum of 25% of live load for typical buildings and a minimum of 50% for places of assembly). If the base shear is less than the lower limit, forces are scaled (amplified) to reach the minimum value and displacement values also are amplified. If the base shear is more than the upper limit, forces can be reduced, but displacements cannot. The minimum base shear requirement, along with the load factor of 1.4 on service lateral forces, results in an effective force reduction factor R^*_{eff} that typically varies from a maximum value of about 5.0 for a period of 0.5 s to a value of about 3.0 for a period of 1.0 s (Lagos and Kupfer 2012).

NCh433.Of96, Section 5.9 limits relative displacements between two consecutive floors, measured at the center of the mass in each direction, to $0.002h_s$, where h_s is the story height. The relative displacements at other locations on the floor plan cannot exceed the value at the center of mass by more than $0.001h_s$. These limits are not expected displacements, but displacements that have been reduced by R^* . For structural wall buildings with 15 to 20 stories, parameter R^* is generally about 6 to 9; however, as noted above, the effective value much lower ($R^*_{eff} = 2$ to 5), since in many cases, forces (and displacements) are amplified to reach the minimum base shear.

5.3. Typical Construction Method and Assumptions

A floor plan view of a typical pre-1985 Chile building is shown in Figure 5.1a. The ratio of wall cross-sectional area to building floor plan area (A_w/A_f) is approximately 3% in each direction for pre-1985 buildings (Wood et al. 1987, Riddell et al. 1987, Sozen 1989, Wallace and Moehle 1993). It is also noted that typical wall thicknesses over the first four stories are 20 cm to 30 cm, with more prominent walls being 30 cm.

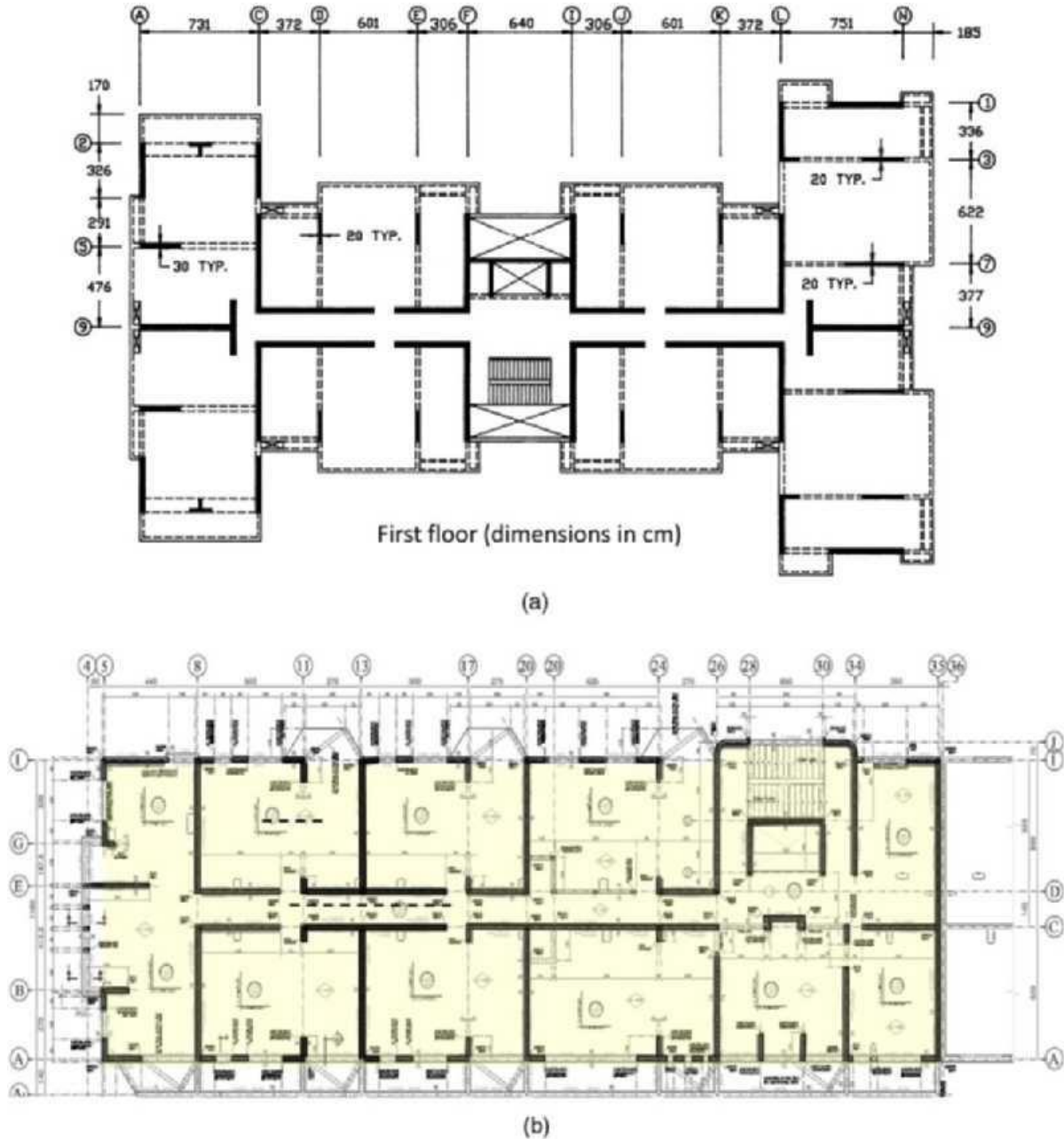


Figure 5.1. (a) Festival Building in Viña Del Mar (1978 construction). (b) Alto Río Building in Concepción (2007 construction).

The relatively large ratios of A_w/A_f were identified as a primary reason for the excellent performance of buildings in the March 1985 earthquake (Wallace and Moehle 1992, 1993; Wallace 1994). Information from 378 RC wall buildings constructed between 1939 and 2000 in Santiago (Gómez 2001), updated to include 76 buildings constructed in the Ñuñoa neighborhood (Santiago) between 2001 and 2006 (Calderón 2007), indicate that about 78% of the construction have ratios of A_w/A_f between 1.5% and 3.5% (Figure 5.2a), with relatively little variation over the years. However, it is noted that although this ratio has remained essentially constant, the number of stories has increased since 1990 to 15 to 25 stories. To consider the impact of the increasing building height Calderón (2007) used parameter $d_{np} = A_w/W$, where W is the number of stories multiplied by the floor weight. The value d_{np} has decreased between 1939 and 2006, starting from an average value of about 0.003 m²/tf (typical for pre-1985 buildings, Figure 5.2b) and reducing to an average value of about 0.002 m²/tf (typical for post-1985 buildings). Pre-1965 construction presents the largest value for d_{np} , reaching an average value close to 0.004 m²/tf.

For preliminary design, some engineers select the wall area in each of the principal directions of the building to limit the average wall shear stress to about 6 kgf/cm². (Riddell et al. 1987). However, for a building seismic weight of 1 tf/m², designed for the maximum base shear ($C_{max} = 0.17W$), this implies a constant d_{np} value of 0.0028 m²/tf, which is consistent with values of d_{np} used prior to 1985 (Figure 5.2b).

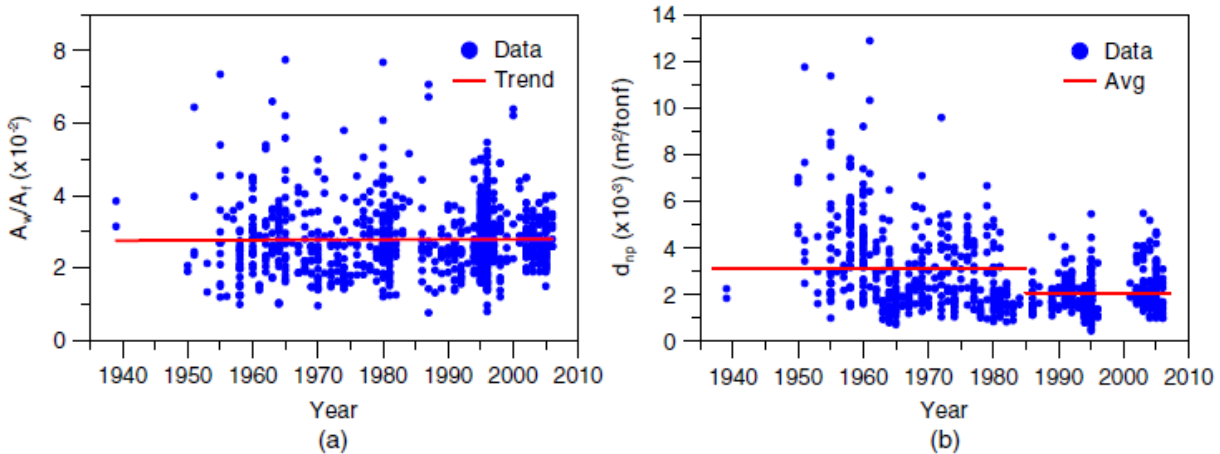


Figure 5.2 (a) A_w/A_f and (b) $d_{np} = A_w/W$ variation over the years (after Calderón 2007).

For newer buildings (Figure 5.1b), walls are typically arranged along a central corridor in the long direction of the building with multiple perpendicular walls in the short building direction. In general, newer buildings have higher aspect ratio, building height to floor plan dimension in the short direction, and thinner walls, in many cases 15 cm to 20 cm, even for buildings up to 20 stories (Estay 2008). In the 1985 earthquake (and in older buildings in the 2010 earthquake), extensive damage was observed in relatively shallow coupling beams used over doors; therefore, in many newer buildings, these beams were often replaced with nonstructural materials, reducing coupling and energy dissipation capacity of newer buildings relatively to pre-1985 buildings.

Modeling of buildings according to NCh433.Of96 is commonly based on the use of gross concrete section stiffness. The impact of stiffness modeling assumptions on fundamental building and the ratio H/T was studied by Calderón (2007), where H represents the height of the building to the ground level and T the natural period of the structure. Results presented in Figure 5.3 indicated that the mean value of H/T has remained essentially constant since 1950 at a value of approximately 70 m/s, with most buildings having H/T ratios between 40 and 140 m/s. It is noted that the variation in H/T is greater for buildings constructed following 1985. For a typical story height of 2.7 m, a ratio of $H/T = 70$ m/s corresponds to a period of $T = N/26$, which is lower than previously noted for measured natural periods in low-level ($N/20$) and ambient vibrations ($N/23$).

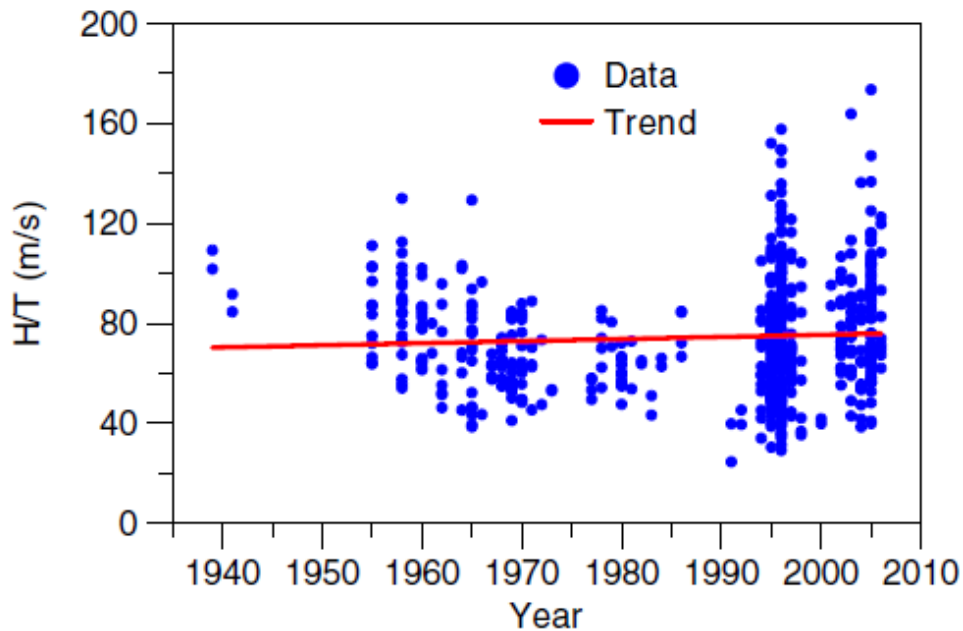


Figure 5.3. H/T values after Calderón (2007).

Neither the Chilean code (NCh433.Of96) nor the ACI code (ACI 318-08) put a limit on the level of axial stress allowed for gravity load or combined gravity and lateral loads, although a limit of $P_u < 0.35 P_0$ was incorporated into UBC-97 (1997). For buildings in Chile, as previously noted, the ratio of wall area to floor plan area has not significantly changed since 1985; however, building heights have increased, resulting in higher levels of axial stress. This trend was captured by Calderón (2007) using the parameter d_{np} , (ratio of wall area in one building direction to building weight), where the median value of d_{np} , decreased from roughly 0.004 m²/tf (pre-1965) to 0.002 m²/tf for post-1985 construction (Figure 5.2b). These ratios indicate that the median axial wall stress has increased from about $0.09Agfc'$ for pre-1965 construction to $0.18Agfc'$ for post-1985 construction, for a typical fc' value of 25 MPa. For post-1985 construction, the ratio of d_{np} , is between 0.001 and 0.003 m²/tf for most buildings, indicating that axial stress levels, on average, vary between approximately 0.10 to $0.30Agfc'$.

A simple study was conducted to further assess the likely level of axial stress in Chilean buildings using two approaches, one based on ratios of A_w/A_f and the other based on wall tributary areas (Figure 5.4). Ratios of A_w/A_f of 1%, 2%, and 3% in each principal building direction were considered whereas tributary areas were estimated for fairly typical walls in the transverse (short) direction of the building based on a review of structural drawings for several damaged buildings constructed around 2005. A unit floor weight of 1.0 tf/m² is used (Riddell et al. 1987). The results based on total wall area to floor area for $(A_w/A_f)_{total}=0.06$, which gives an average value for all walls within a building, are consistent with results presented in the prior paragraph, that is, axial stress ratios of roughly 0.10 $A_g f_0 c$ for pre-1965 buildings (10 to 15 stories) and about double that for 20 to 25 story buildings. The results for the tributary area indicate that individual walls could have much higher axial stress ratios, in the range of 0.20 to 0.40 $A_g f_0 c$ for 15 to 20 stories. This finding is supported by design information for ten different buildings designed between 2000 and 2006 where axial stress ratios for combined gravity and lateral earthquake load were between 20% and 50% with a mean value about 35% (Estay 2008).

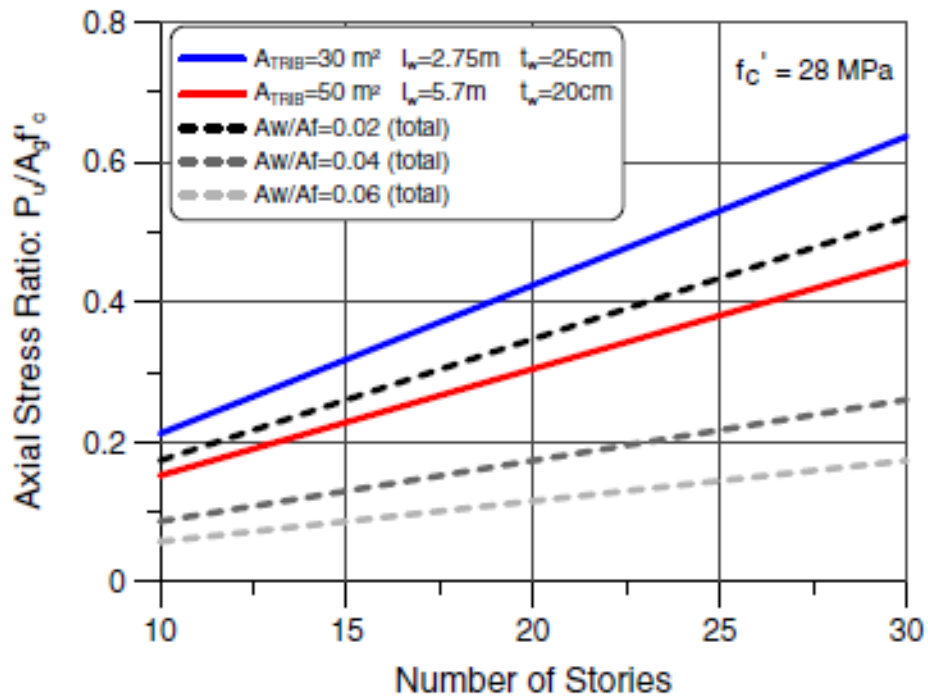


Figure 5.4. H/T Estimated wall axial stress ratios.

Hoops with 90-degree hooks, typically spaced at 20cm vertically, are commonly around boundary longitudinal reinforcement (Figure 5.5). Because of the large number of walls used in typical buildings, the quantity of boundary longitudinal reinforcement is light relative to typical U.S. construction. Typical web vertical and horizontal reinforcement in newer buildings consists of 10mm diameter bars spaced at 20 cm ($\rho_v = 0.39\%$) and 8mm diameter bars spaced at 20 cm ($\rho_t = 0.25\%$), respectively. Horizontal web bars are typically placed outside of vertical bars and anchored at the wall edge with 90-degree hooks.

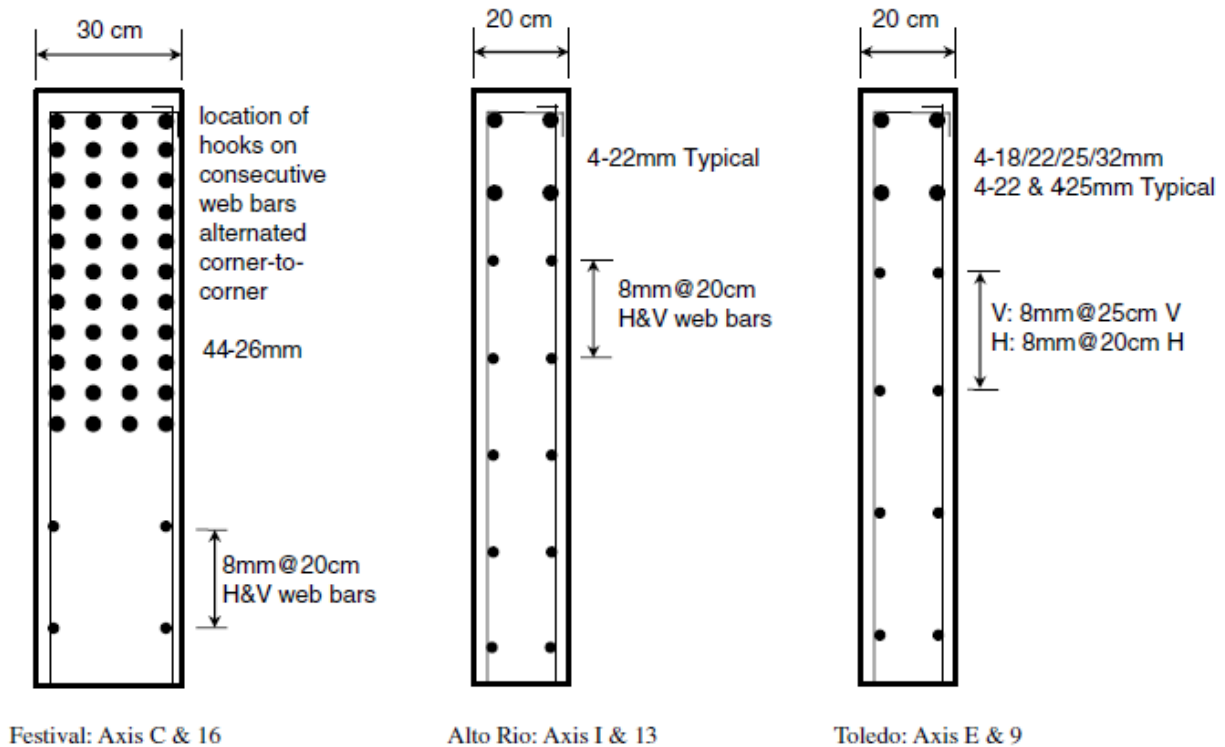


Figure 5.5. Typical wall boundaries: (a) Festival; (b) Alto Río; (c) Toledo.

5.4. Implementation of Chilean code assumptions in the case study

Chilean code assumptions and provisions were implemented in the case study herein as the existing building was strengthened by a certain number of shear walls in order to make the ratio of shear wall in the one principal direction (Y) of the building to the floor area (A_w/A_f) about 3% in each floor to check the enhancement or improvement of the building seismic response taking into account reducing the existed shear walls and core reinforcement.

The modification made to the building is illustrated in following sub division attributed by Pushover and Eigen value analysis representing the characteristics of the building.

5.4.1. Strengthened building layout

Five shear walls were introduced in the Y-direction with total area of 3.5 m², with minimum required light reinforcement in longitudinal and transversal directions which consists of 10mm diameter bars spaced at 20 cm ($\rho_v = 0.39\%$) and 8mm diameter bars spaced at 20 cm ($\rho_t = 0.25\%$), respectively. Horizontal web bars are typically placed outside of vertical bars and anchored at the wall edge with 90-degree hooks.

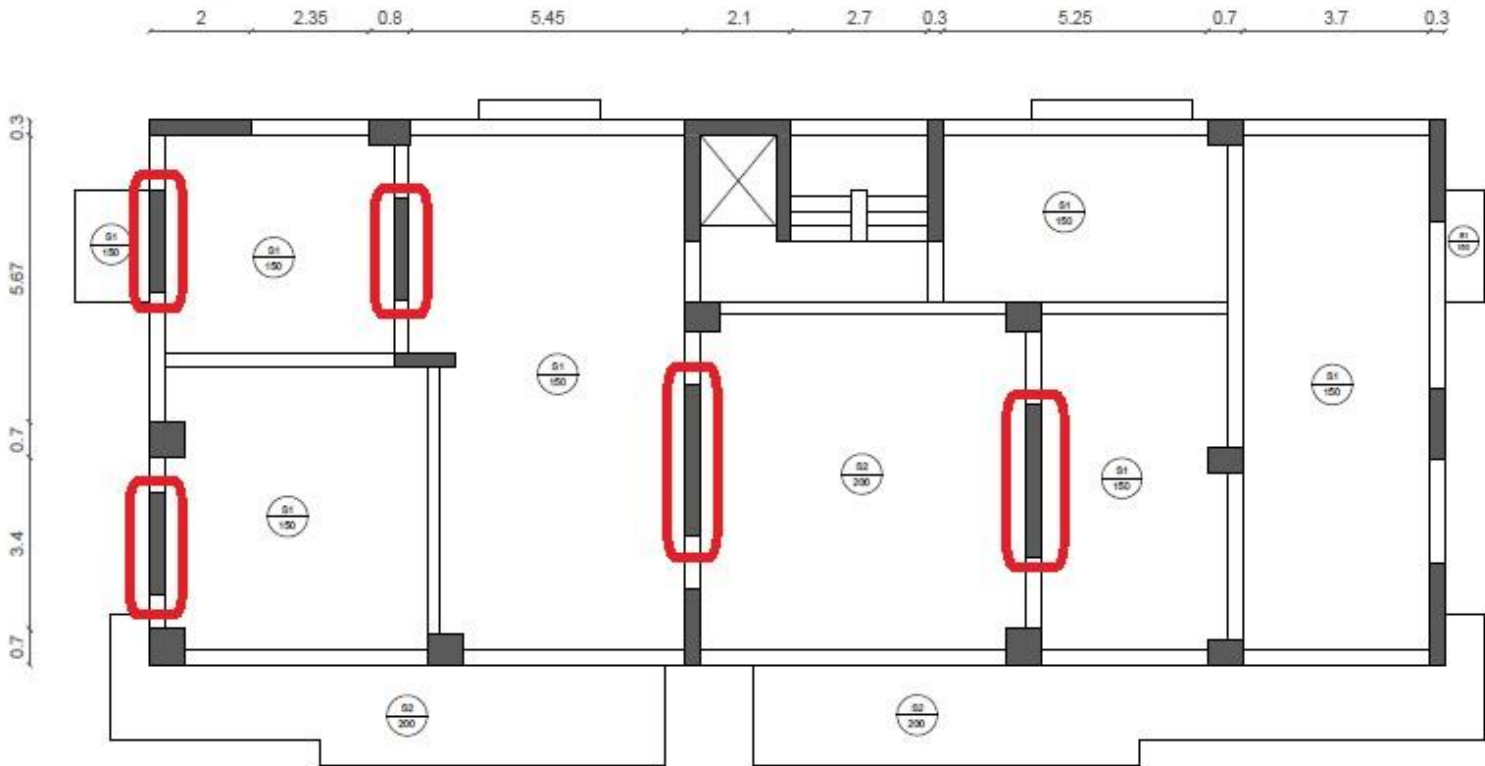
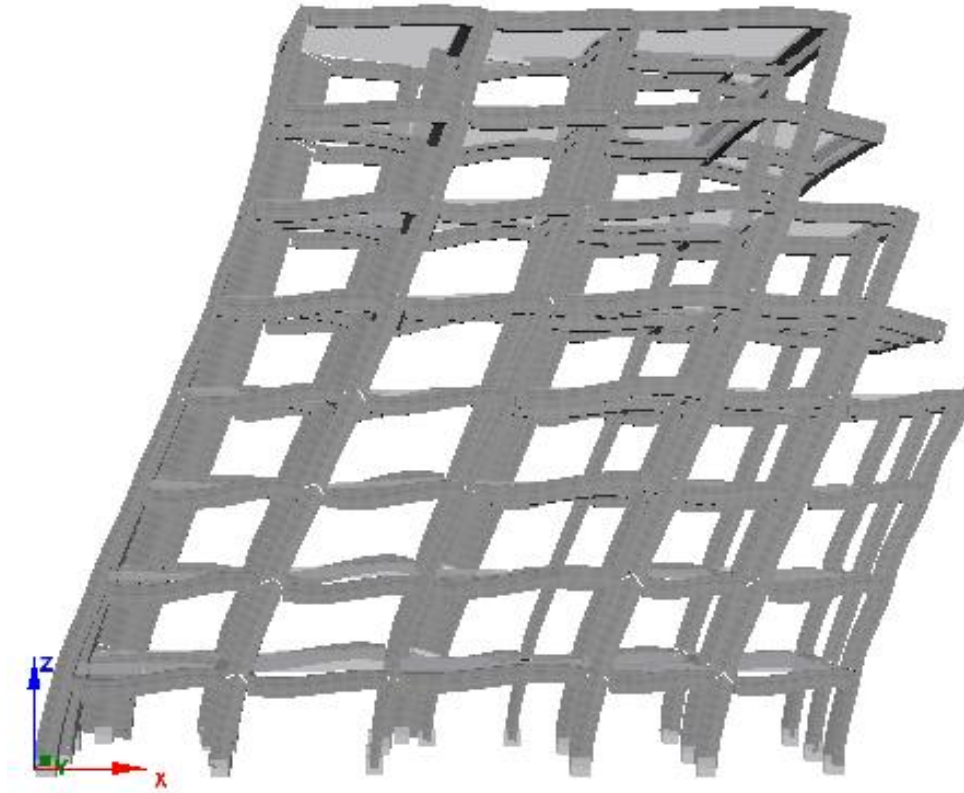


Figure 5.6. Plan View of the Strengthened building

5.4.2. Eigen value analysis

In the calculation of eigenvalues analysis the efficient Lanczos algorithm [Hughes, 1987] is used for the evaluation of the structural natural frequencies and mode shapes.

The number of Eigenvalues used is 10 as shown in table 5.1.



**Figure 5.7. Deformed shape of the building at the fundamental period (0.56 secs)
From Eigen-value analysis.**

MODAL PERIODS AND FREQUENCIES		
Mode	Period (sec)	Frequency (Hertz)
1	0.56778071	1.76124336
2	0.28976843	3.45103153
3	0.25871798	3.86521255
4	0.18981624	5.26825307
5	0.13338849	7.4968985
6	0.12190602	8.20304057
7	0.10081859	9.9188054
8	0.09820132	10.18316278
9	0.08697631	11.49738367
10	0.08064702	12.39971488

Table 5.1. Modal periods and frequencies.

5.4.3. Pushover analysis

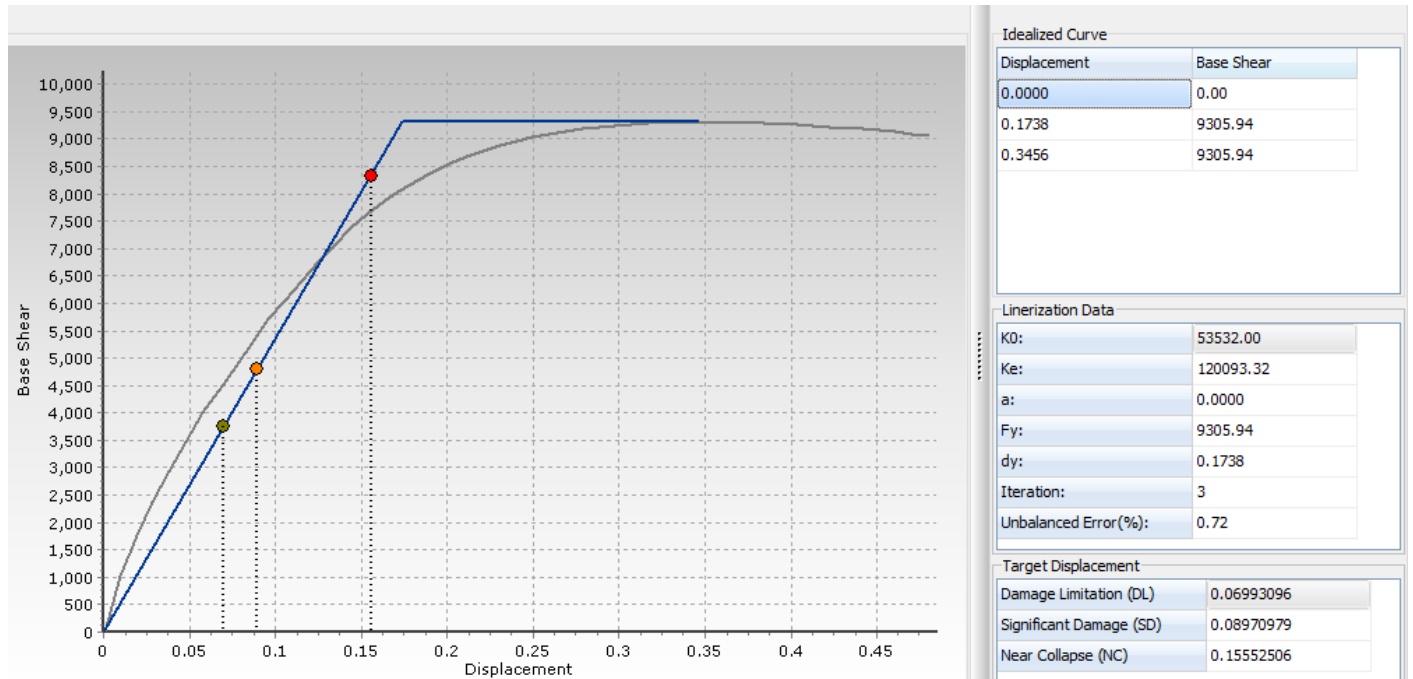


Figure 5.8. Pushover capacity curve in X-direction.

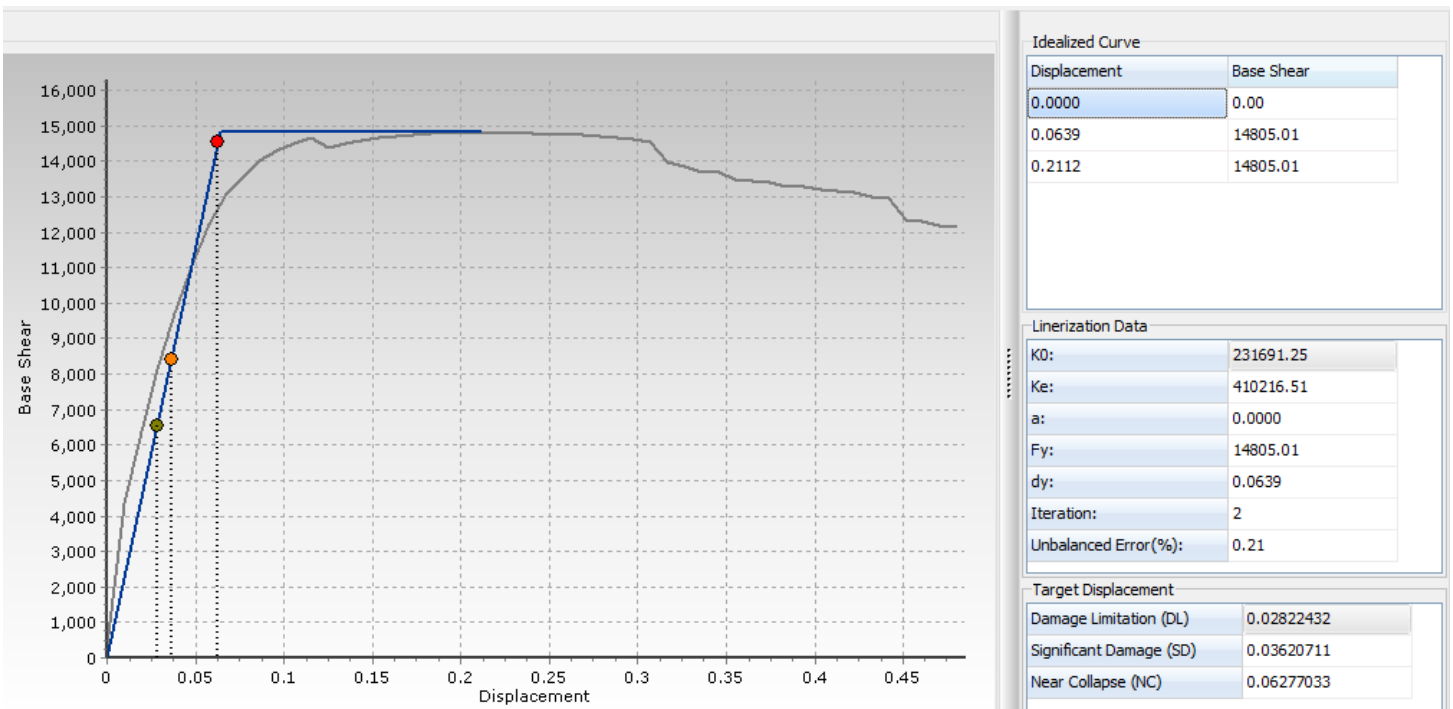


Figure 5.9. Pushover capacity curve in Y-direction.

CHAPTER 6 DATA ANALYSIS AND RESULTS

6.1. Identification of damage limit states for RC buildings

In order to carry out risk assessments for building populations of varied composition, it is either necessary to develop a series of vulnerability curve sets for different building types where the performance criteria are defined according to the specified structural characteristics, or use observational damage statistics that provide a compositional match to the assessed building stock.

In practice, it is impossible to find the quantity and range of damage distribution data required for either of these approaches to be implemented with any confidence in the result. A new approach is therefore proposed by (T. Rossetto, A. Elnashai) wherein data for different structural systems can be combined to produce a single set of ‘homogenized’ or ‘general’ curves applicable to all, through the use of a damage scale that accounts for the differences in the damage rate of disparate systems. Such a damage scale is required to adopt limit states that are defined in terms of both the damage expected in different structural systems and of a structural response parameter indicative of the global building damage state.

A new damage scale named the homogenized reinforced concrete damage scale (HRC scale) is therefore proposed and used herein to generate vulnerability curves. The scale is subdivided into seven damage states, each of which is clearly defined in Table 6.1 in terms of the typical structural and non-structural damage expected in the four main types of reinforced concrete structure found in Europe.

ISD _{max%} (%) limits for HRC-scale				
HRC damage state	All	N-D MRF	Infilled MRF	Shear-walls
None	0.00	0.00	0.00	0.00
Slight	0.13	0.32	0.05	0.26
Light	0.19	0.43	0.08	0.34
Moderate	0.56	1.02	0.30	0.72
Extensive	1.63	2.41	1.15	1.54
Part. Coll.	3.34	4.27	2.80	2.56
Collapse	>4.78	>5.68	>4.36	>3.31

Table 6.1. Threshold values of ISD_{max%} defining the HRC-scale damage limit states for general RC structures (All), non-ductile MRF, infilled MRF and shear wall structures.



6.2. Methodology

Using Seismostruct software a nonlinear time history analysis has been performed for 16 near field records to obtain the displacement time history of an existing building in Athens. These 16 records are originally obtained from 8 stations, 4 accelerograms in each of Norcia and Aquila regions, each accelerogram gives 2 components the East-west and the North-south which are illustrated below as DATA1 and DATA2.

Results arising from applying these “near-fault” ground motion records to the building are obtained, these results indicates the top floor displacement that the building undergoes due to that certain ground motion record divided by the total building height representing the inter storey drift ratio to evaluate the damage limit states.

The ground motions under investigation have an input parameter of time step size 0.01 sec, the total number of output time step ranges between 3000 to 5000 (30 sec to 50 sec) depending on the length of the accelerogram. All accelerograms are applied in positive X and Y-directions with a damping ratio near to 5%.

The displacement value gives an indication for at which structural damage state the building will suffer when subjected to such a ground motion, these results are represented in the form of plots followed by tables for each earthquake showing the maximum displacement and the corresponding predefined limit damage state.



6.3. Dynamic time history Results for the original building

6.3.1. Aquila earthquake in X-Direction

6.3.1.1. Record from AQA station

1. AQA-Data1 @ X-Dir

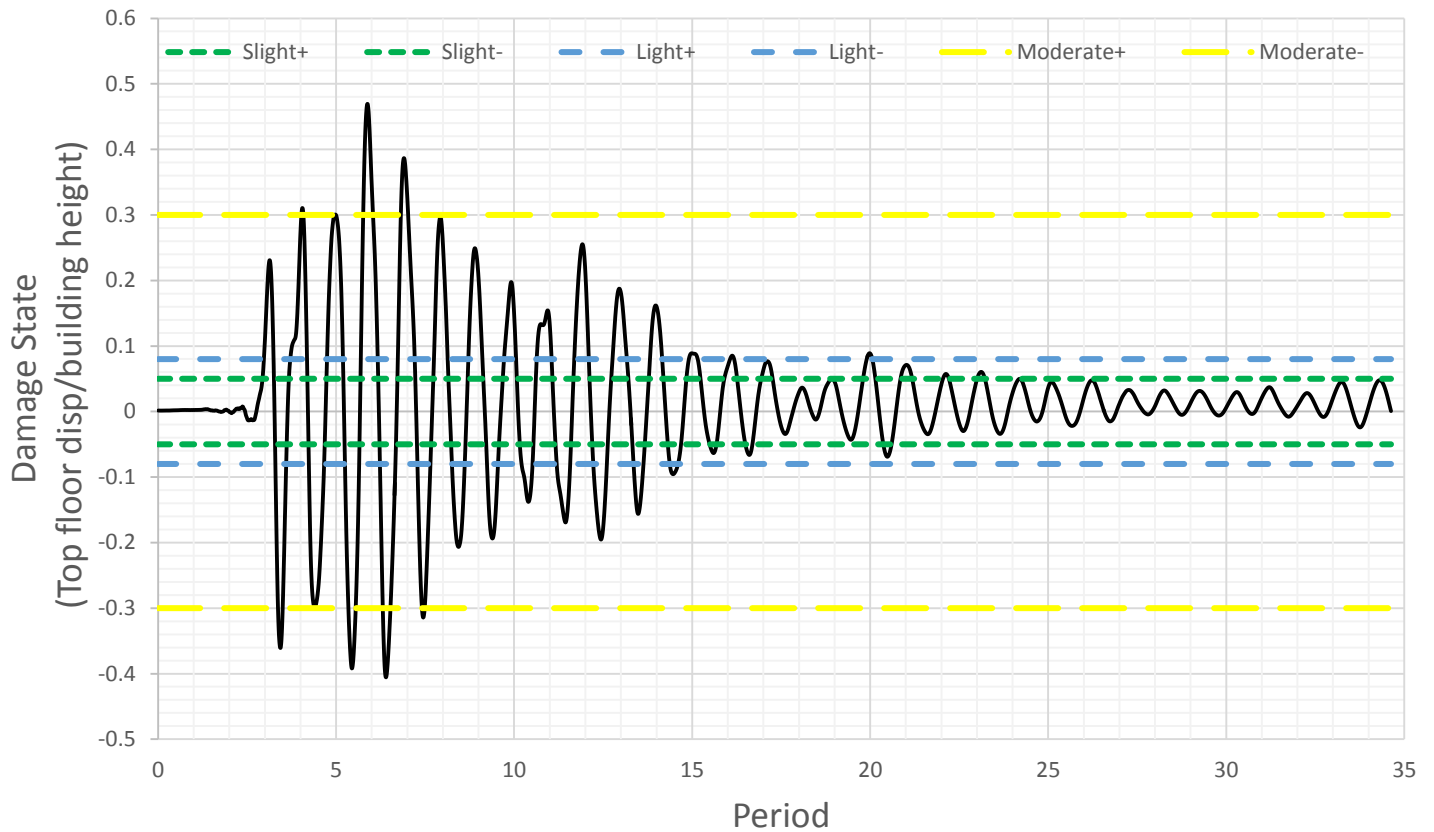


Figure 6.1. Figure showing ISD% and damage limit states (Infilled MRF) for recording station AQA

Record	Max. Roof Displacement	Drift (Disp./height)%	Damage State
AQA-DATA1	0.11	0.47	Moderate

Table 6.2. Table of Displacements and damage levels for recording station AQA

2. AQA-Data2 @ X-Dir

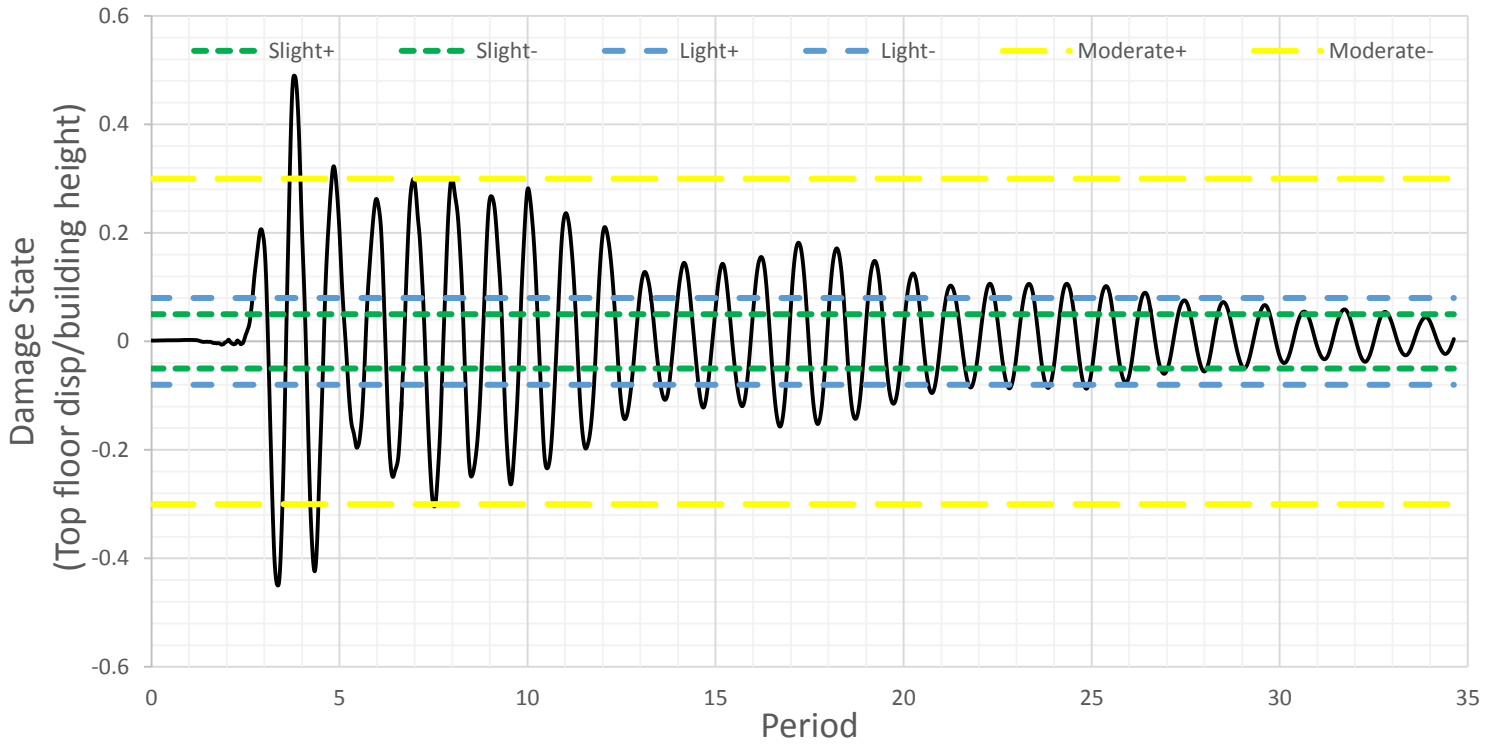


Figure 6.2. Figure showing ISD% and damage limit states (Infilled MRF) for recording station AQA

Record	Max. Roof Displacement	Drift (Disp./height)%	Damage State
AQA-DATA2	0.12	0.49	Moderate

Table 6.3. Table of Displacements and damage levels for recording station AQA



6.3.1.2. Record from AQG station

1. AQG-Data1 @ X-Dir

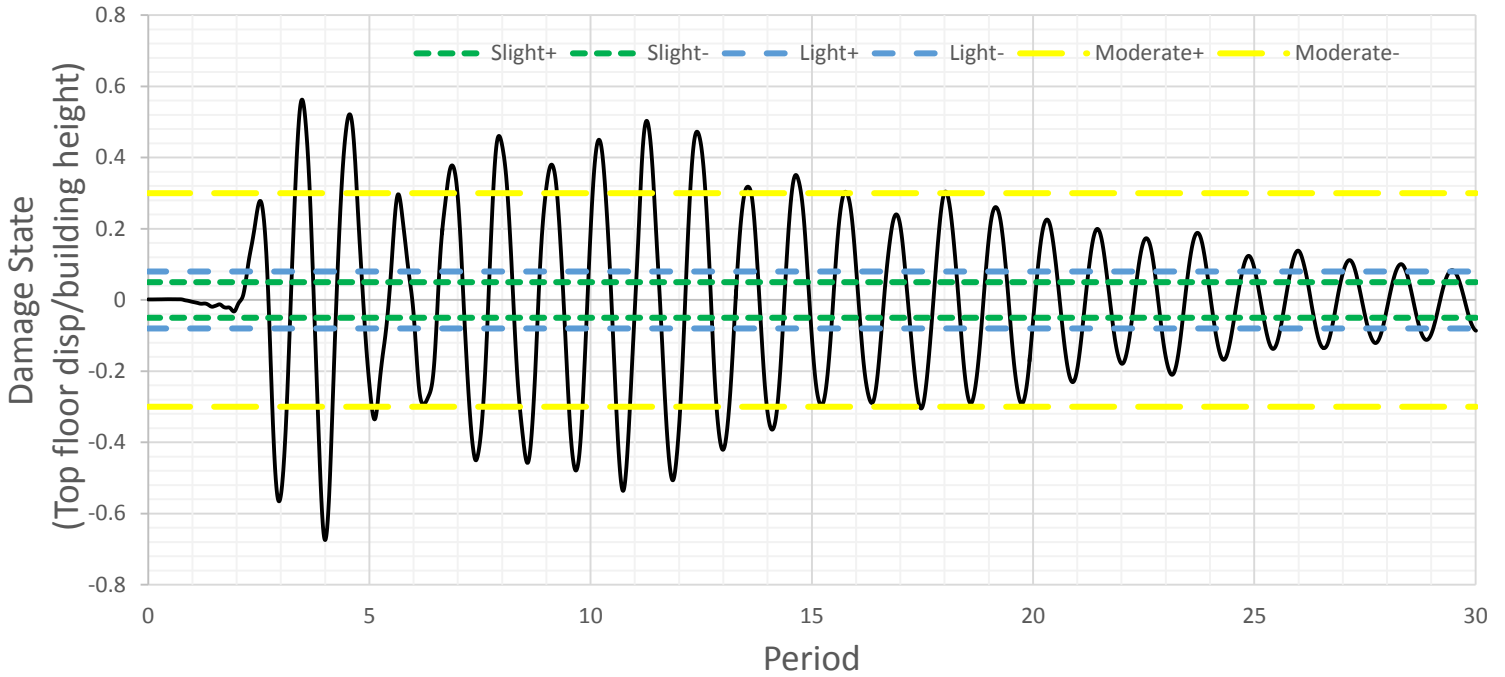


Figure 6.3. Figure showing ISD% and damage limit states (Infilled MRF) for recording station AQG

Record	Max. Roof Displacement	Drift (Disp./height)%	Damage State
AQG-DATA1	-0.16	-0.67	Moderate

Table 6.4. Table of Displacements and damage levels for recording station AQG



2. AQG-Data2 @ X-Dir

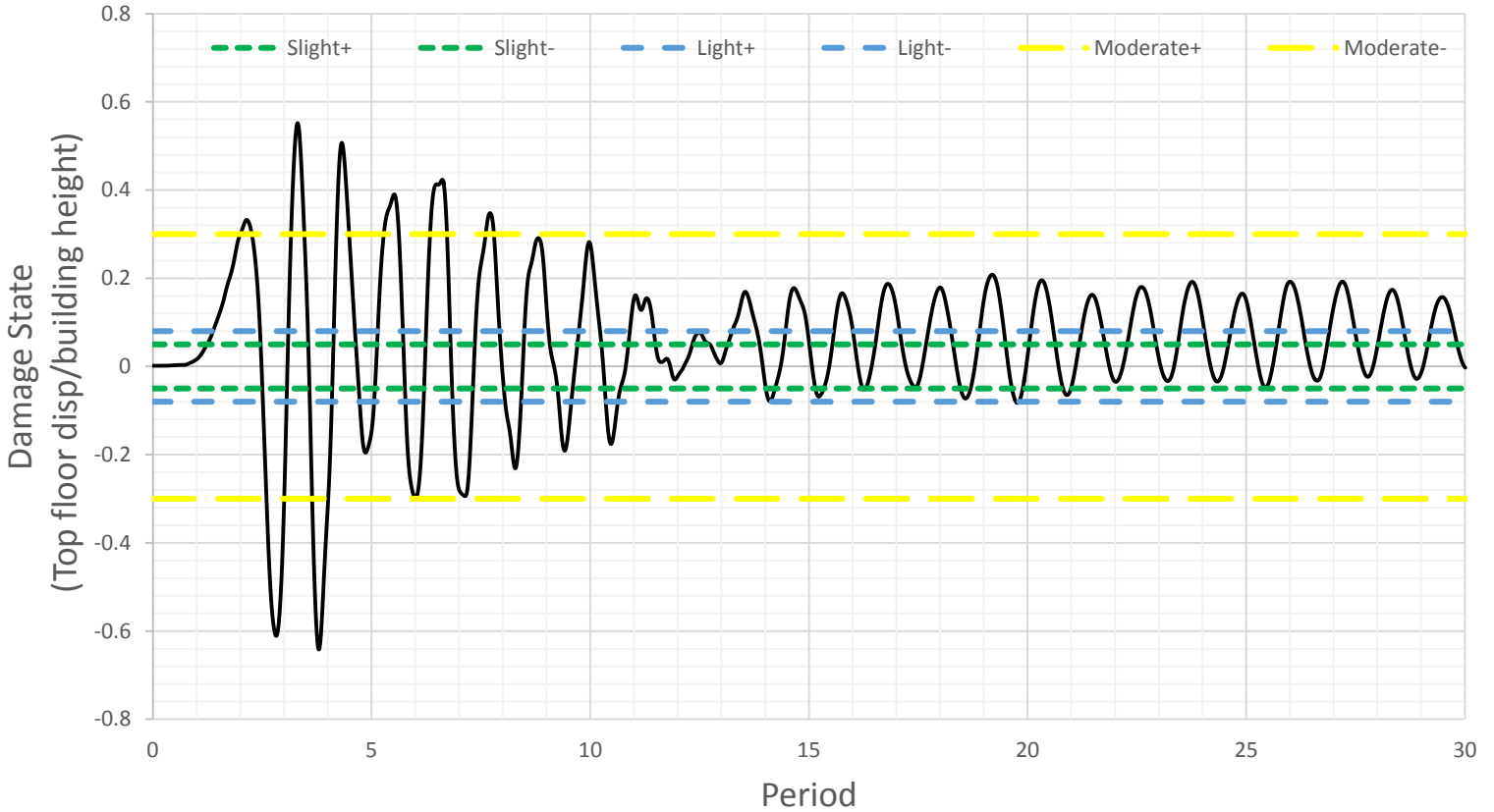


Figure 6.4. Figure showing ISD% and damage limit states (Infilled MRF) for recording station AQG

Record	Max. Roof Displacement	Drift (Disp./height)%	Damage State
AQG-DATA2	-0.15	-0.64	Moderate

Table 6.5. Table of Displacements and damage levels for recording station AQG



6.3.1.3. Record from AQK station

1. AQK-Data1 @X-Dir.

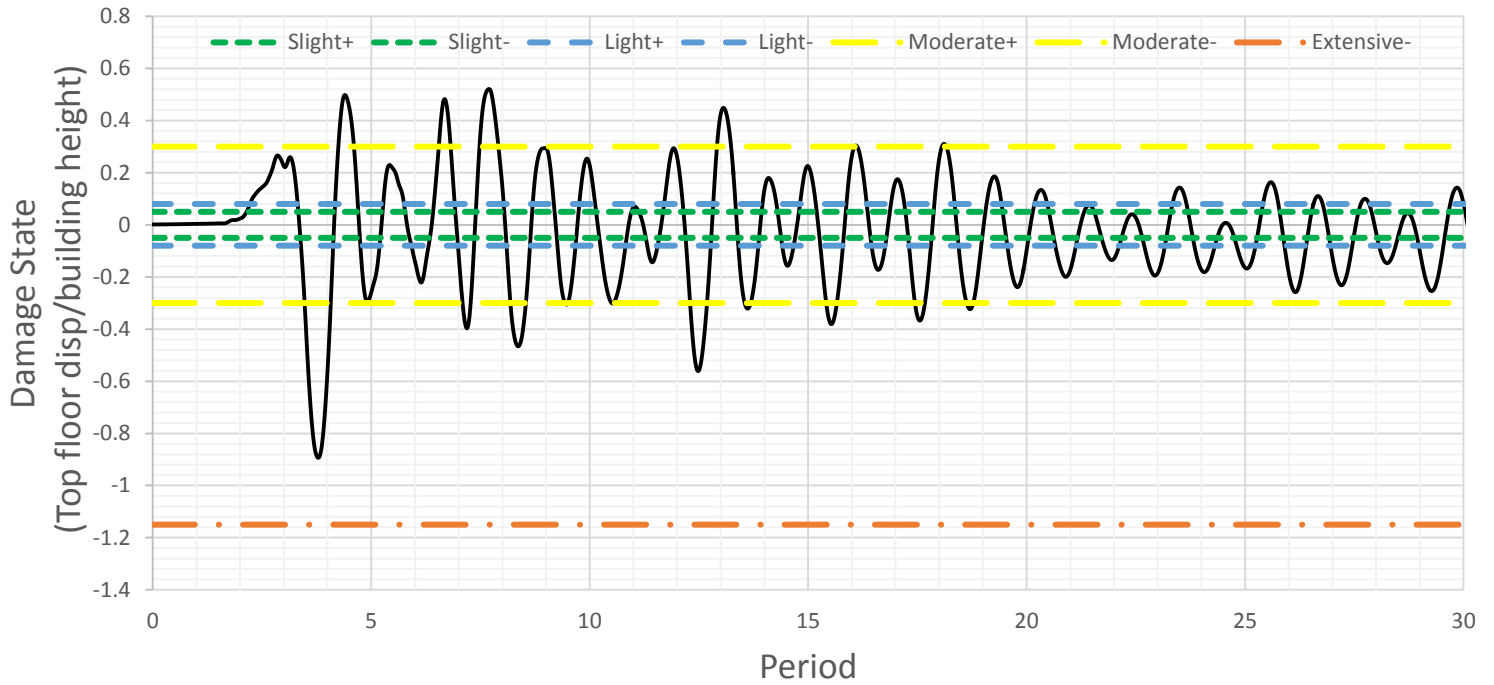


Figure 6.5. Figure showing ISD% and damage limit states (Infilled MRF) for recording station AQK

Record	Max. Roof Displacement	Drift (Disp./height)%	Damage State
AQK-DATA1	-0.21	-0.89	Moderate

Table 6.6. Table of Displacements and damage levels for recording station AQK



2. AQK-Data2 @X-Dir.

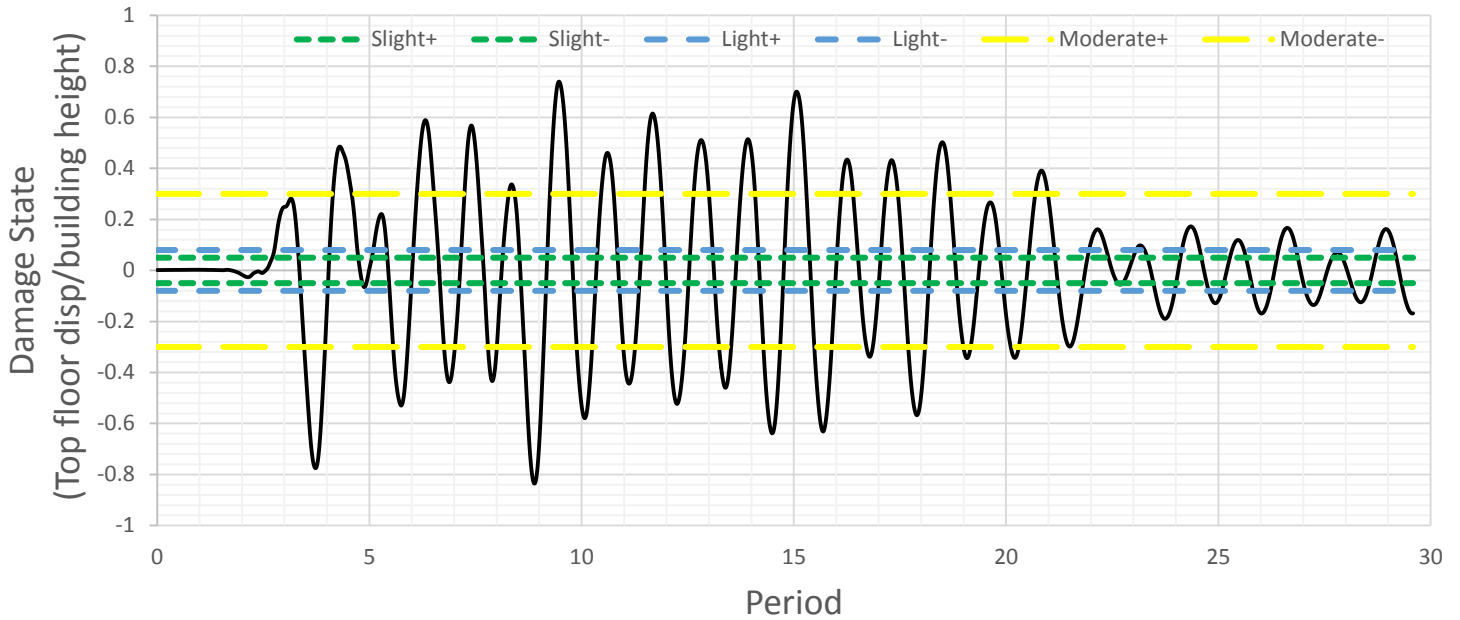


Figure 6.6. Figure showing ISD% and damage limit states (Infilled MRF) for recording station AQK

Record	Max. Roof Displacement	Drift (Disp./height)%	Damage State
AQK-DATA2	-0.20	-0.84	Moderate

Table 6.7. Table of Displacements and damage levels for recording station AQK



6.3.1.4. Record from AQV Station

1. AQV-Data1 @X-Dir.

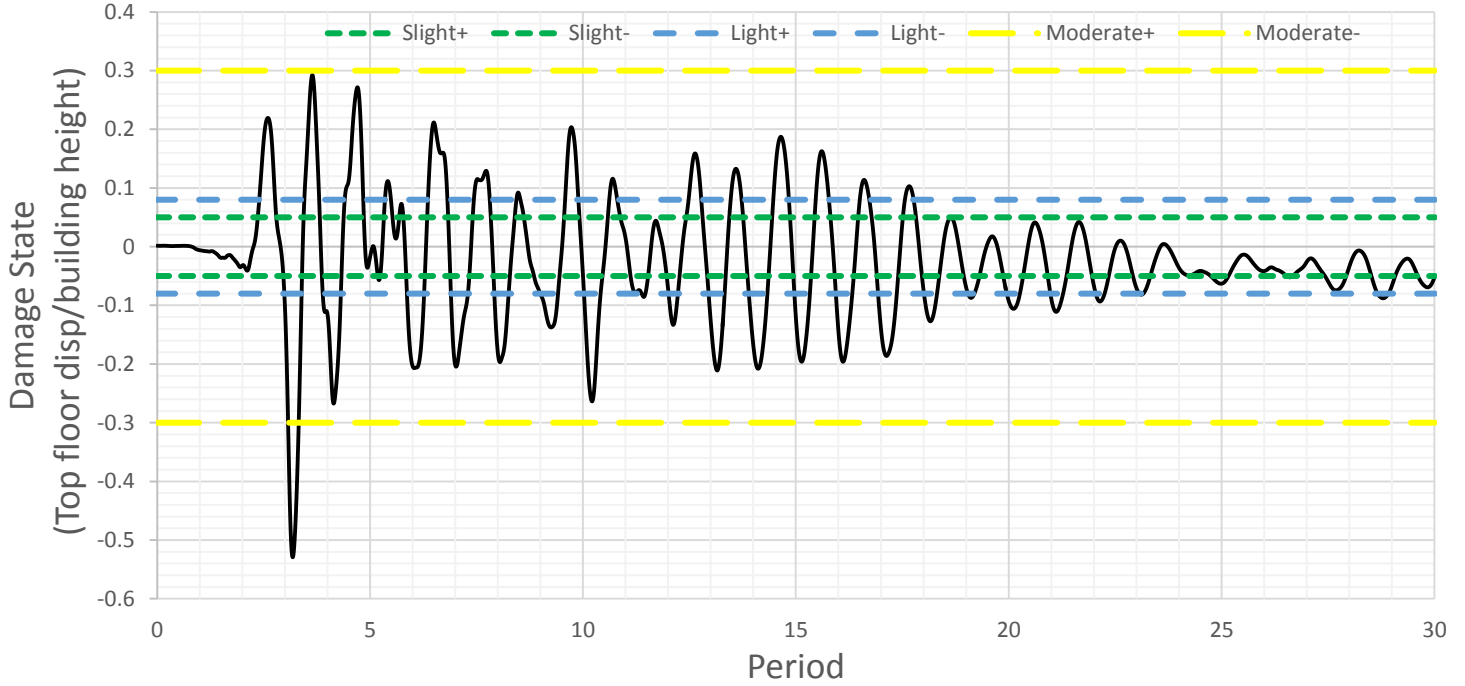


Figure 6.7. Figure showing ISD% and damage limit states (Infilled MRF) for recording station AQV

Record	Max. Roof Displacement	Drift (Disp./height)%	Damage State
AQV-DATA1	-0.13	-0.53	Moderate

Table 6.8. Table of Displacements and damage levels for recording station AQV



2. AQV-Data2 @X-Dir.

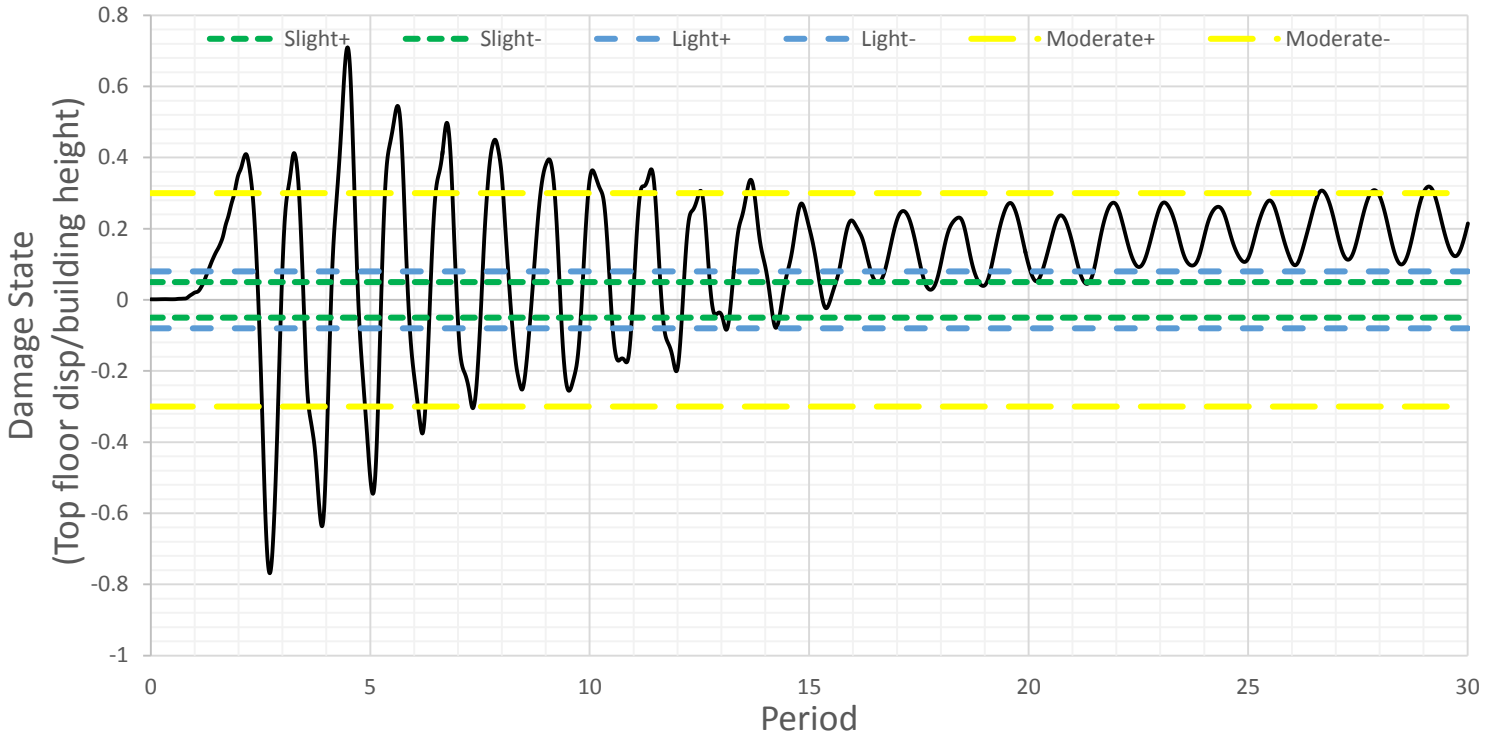


Figure 6.8. Figure showing ISD% and damage limit states (Infilled MRF) for recording station AQV

Record	Max. Roof Displacement	Drift (Disp./height)%	Damage State
AQV-DATA2	-0.18	-0.77	Moderate

Table 6.9. Table of Displacements and damage levels for recording station AQV



6.3.2. Norcia earthquake in X-Direction
6.3.2.1. Record from ACC station

1. ACC-Data1 @ X-Dir.

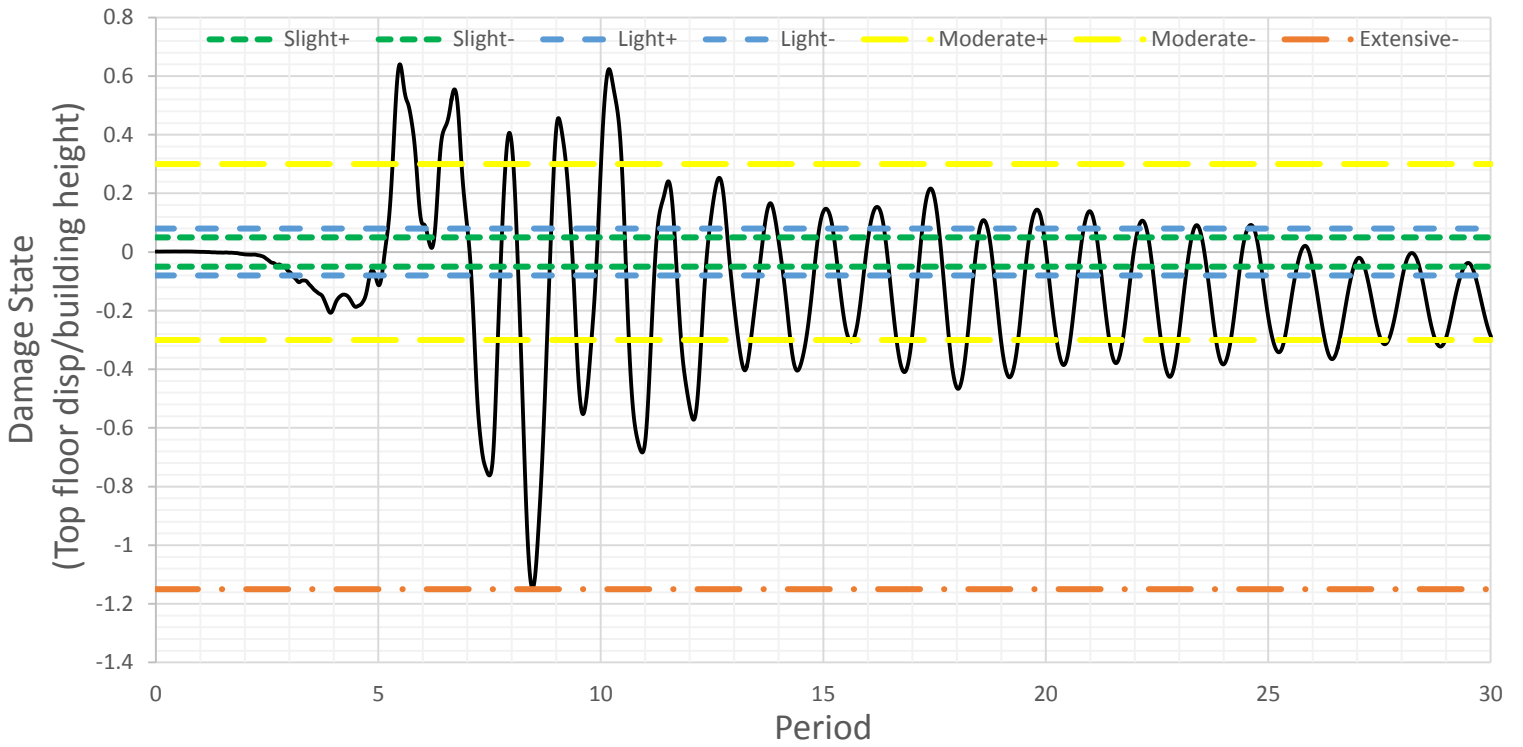


Figure 6.9. Figure showing ISD% and damage limit states (Infilled MRF) for recording station ACC

Record	Max. Roof Displacement	Drift (Disp./height)%	Damage State
ACC-DATA1	-0.28	-1.15	Extensive

Table 6.10. Table of Displacements and damage levels for recording station ACC



2. ACC-Data2 @ X-Dir.

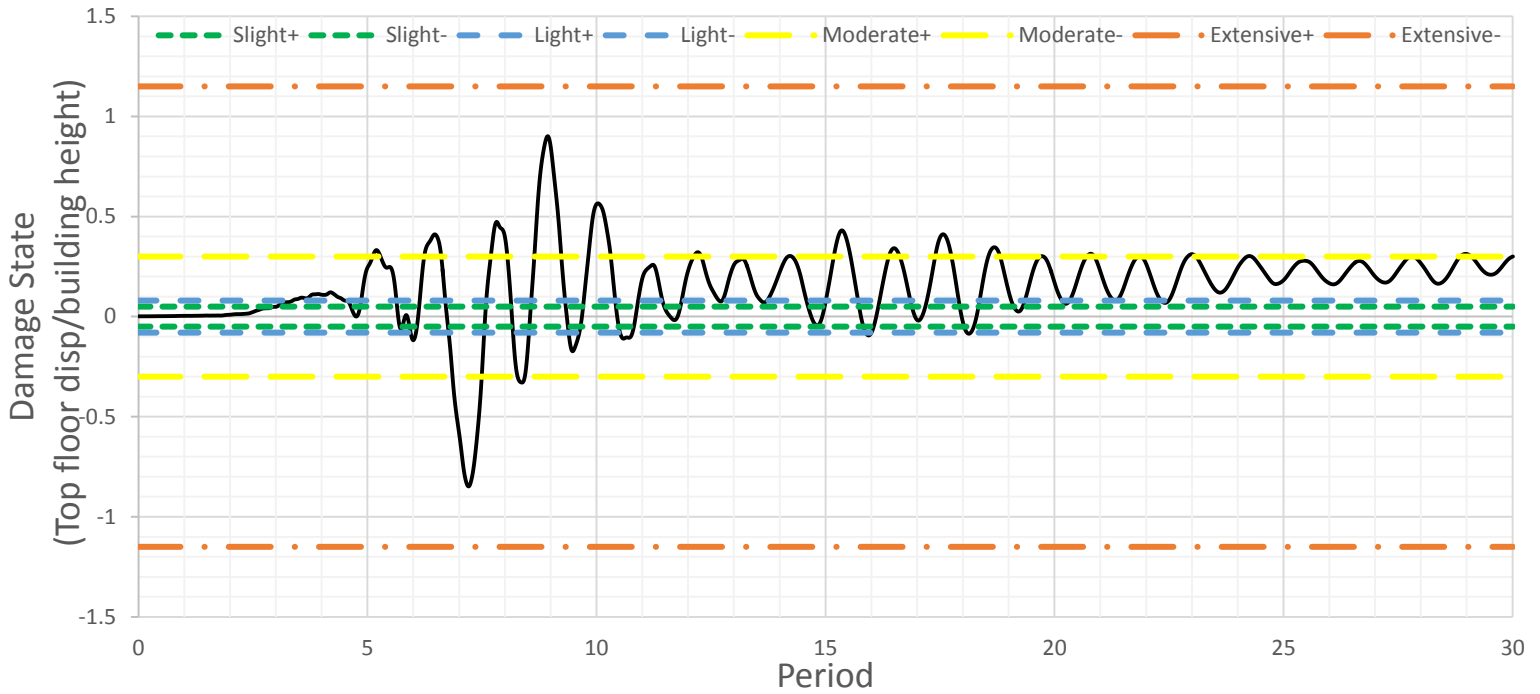


Figure 6.10. Figure showing ISD% and damage limit states (Infilled MRF) for recording station ACC

Record	Max. Roof Displacement	Drift (Disp./height)%	Damage State
ACC-DATA2	0.20	0.90	Moderate

Table 6.11. Table of Displacements and damage levels for recording station ACC

6.3.2.2. Record from AMT station

1. AMT-Data1 @ X-Dir.

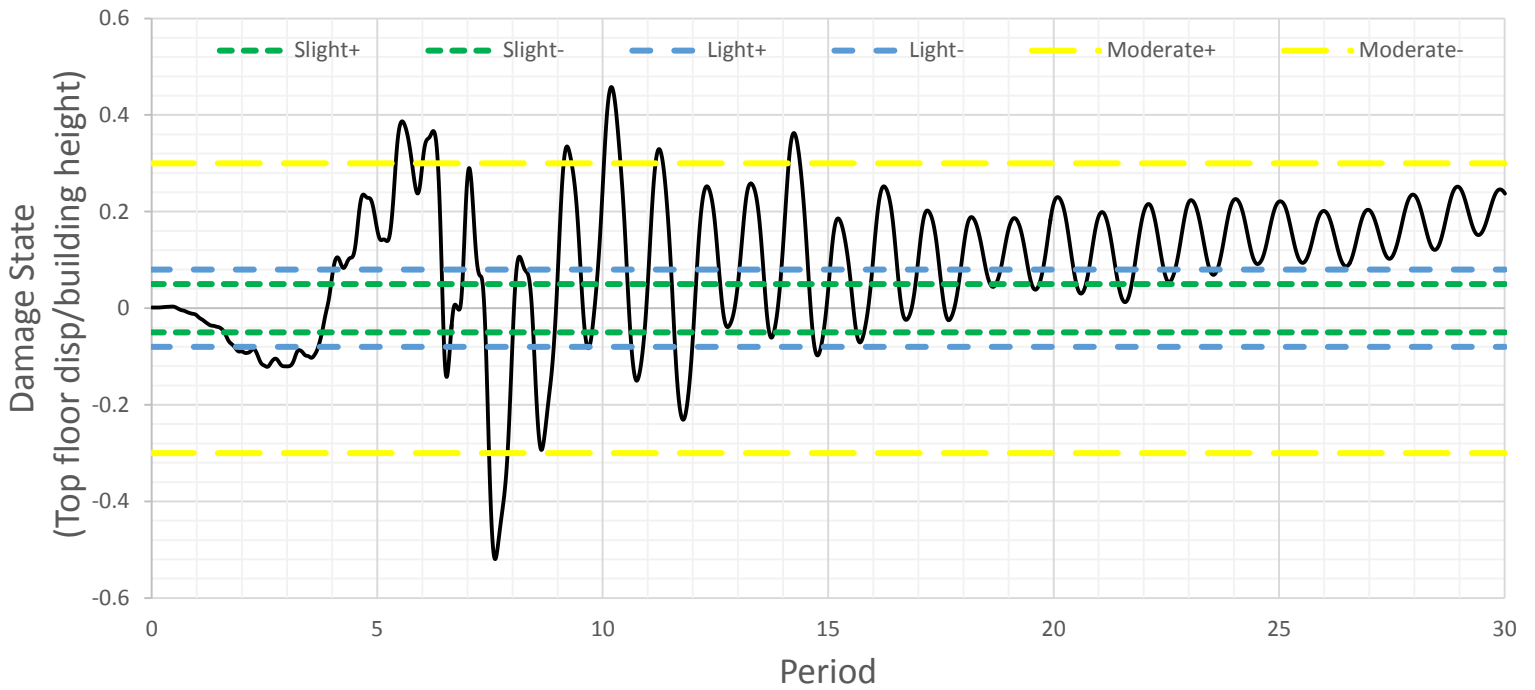


Figure 6.11. Figure showing ISD% and damage limit states (Infilled MRF) for recording station AMT

Record	Max. Roof Displacement	Drift (Disp./height)%	Damage State
AMT-DATA1	-0.12	-0.52	Moderate

Table 6.12. Table of Displacements and damage levels for recording station AMT



2. AMT-Data2 @ X-Dir.

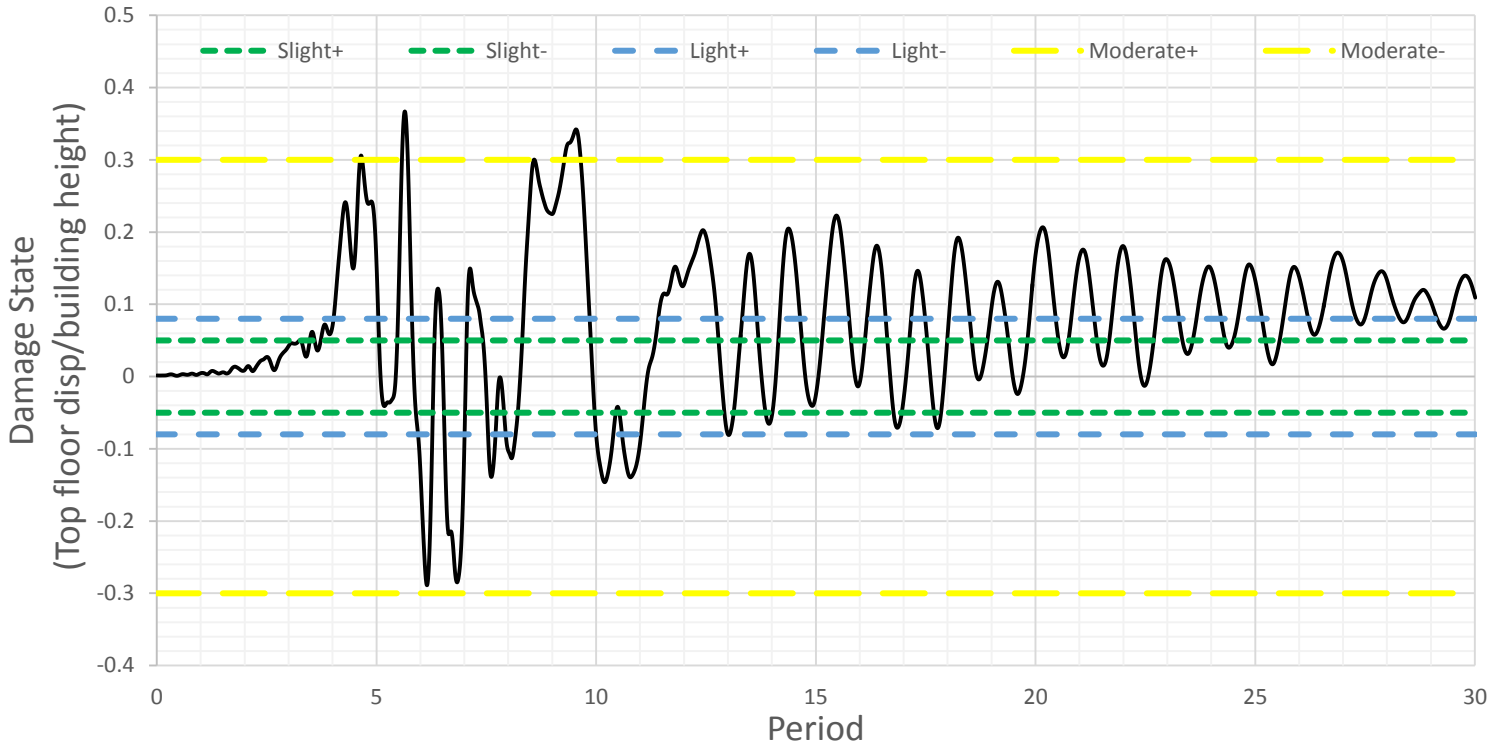


Figure 6.12. Figure showing ISD% and damage limit states (Infilled MRF) for recording station AMT

Record	Max. Roof Displacement	Drift (Disp./height)%	Damage State
AMT-DATA2	-0.09	-0.37	Moderate

Table 6.13. Table of Displacements and damage levels for recording station AMT

6.3.2.3. Record from T1201 station

1. T1201-Data1 @ X-Dir.

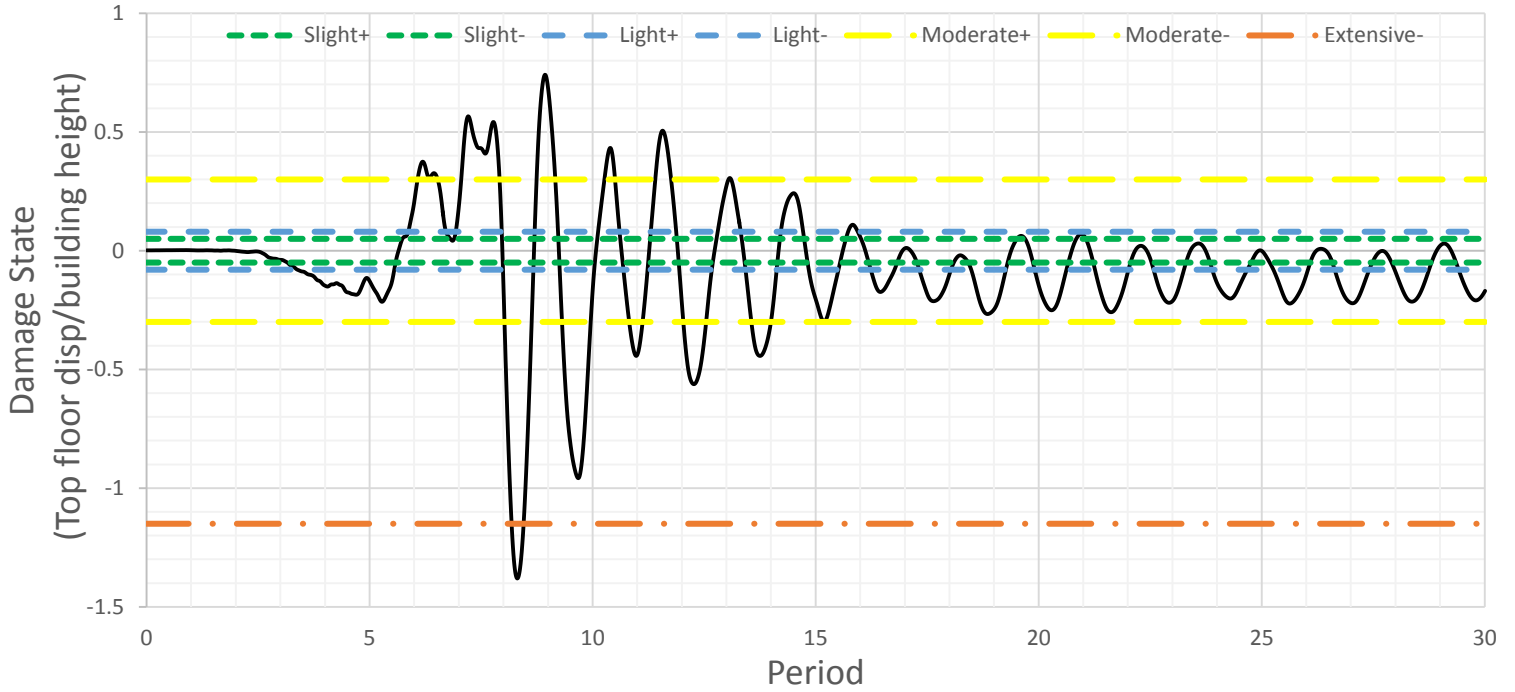


Figure 6.13. Figure showing ISD% and damage limit states (Infilled MRF) for recording station T1201

Record	Max. Roof Displacement	Drift (Disp./height)%	Damage State
T1201-DATA1	-0.33	-1.38	Extensive

Table 6.14. Table of Displacements and damage levels for recording station T1201



2. T1201-Data2 @ X-Dir.

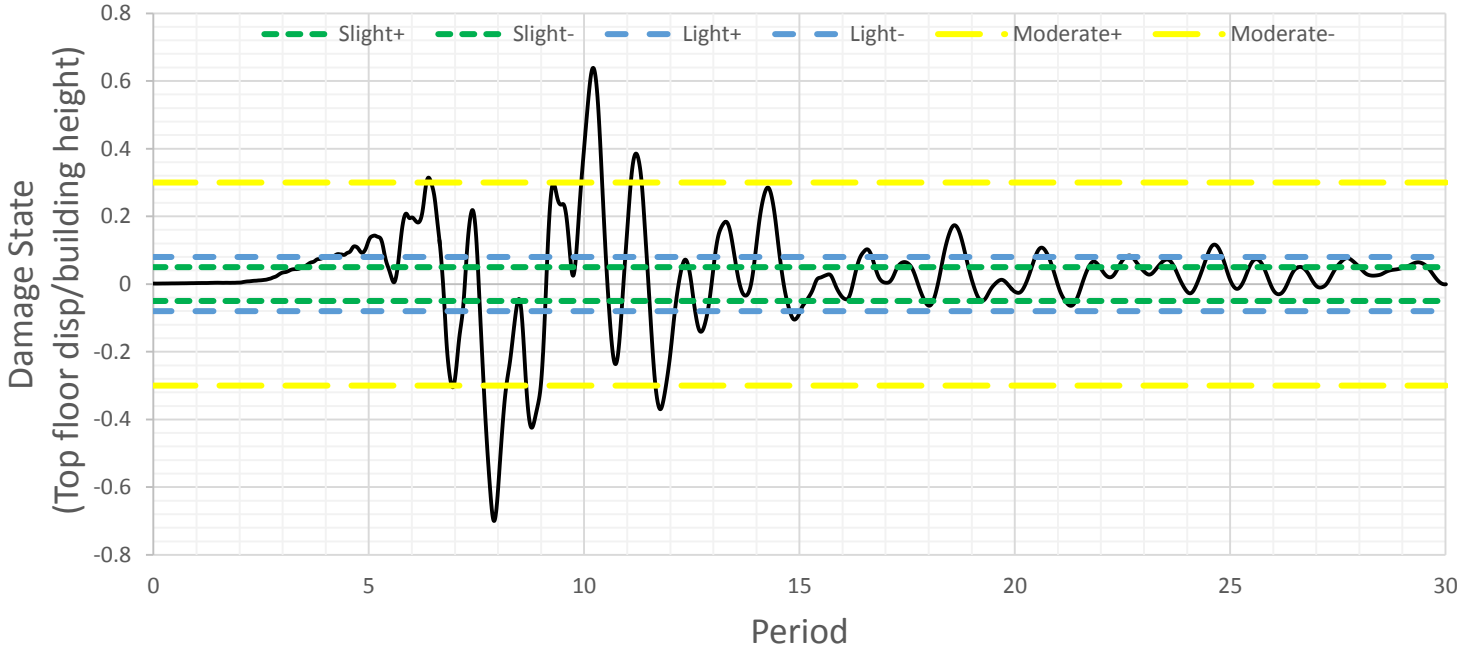


Figure 6.14. Figure showing ISD% and damage limit states (Infilled MRF) for recording station T1201

Record	Max. Roof Displacement	Drift (Disp./height)%	Damage State
T1201-DATA2	-0.17	-0.70	Moderate

Table 6.15. Table of Displacements and damage levels for recording station T1201

6.3.2.4. Record from NRC station

1. NRC-Data1 @ X-Dir.

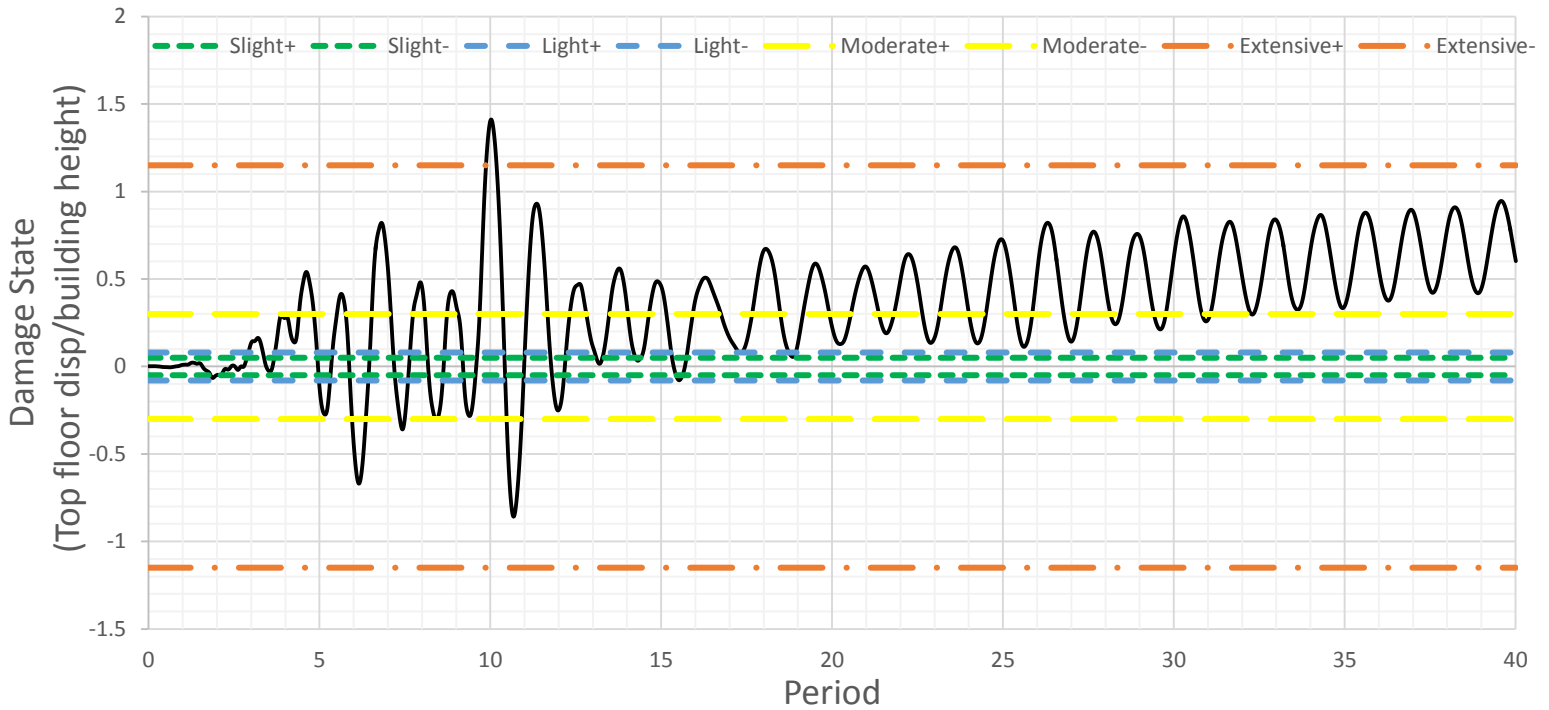


Figure 6.15. Figure showing ISD% and damage limit states (Infilled MRF) for recording station NRC

Record	Max. Roof Displacement	Drift (Disp./height)%	Damage State
NRC-DATA1	0.34	1.41	Extensive

Table 6.16. Table of Displacements and damage levels for recording station NRC



2. NRC-Data2 @ X-Dir.

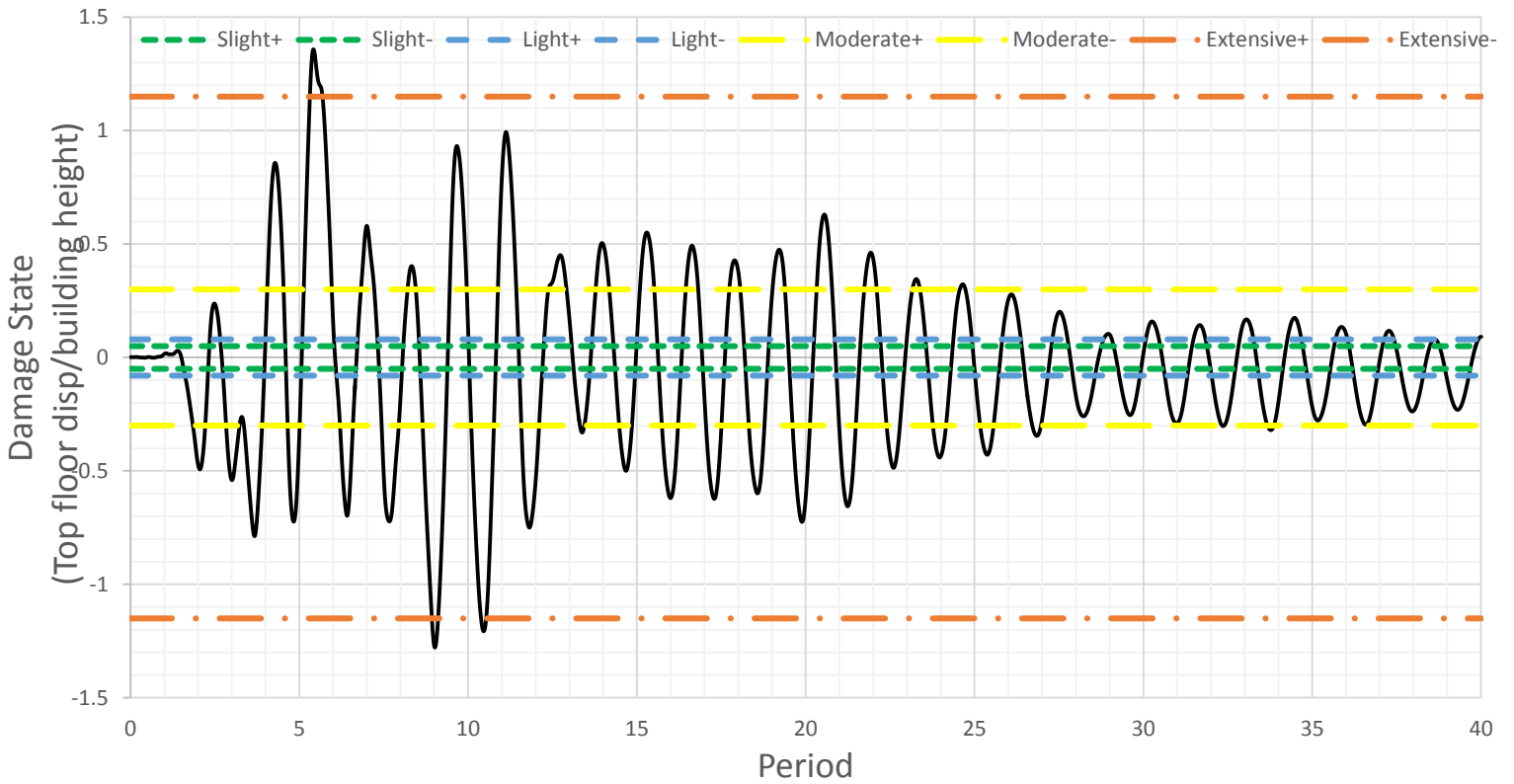


Figure 6.16. Figure showing ISD% and damage limit states (Infilled MRF) for recording station NRC

Record	Max. Roof Displacement	Drift (Disp./height)%	Damage State
NRC-DATA2	-0.31	-1.28	Extensive

Table 6.17. Table of Displacements and damage levels for recording station NRC



6.3.3. Aquila earthquake in Y-direction
6.3.3.1. Record from AQA station

1. AQA-Data1 @ Y-Dir

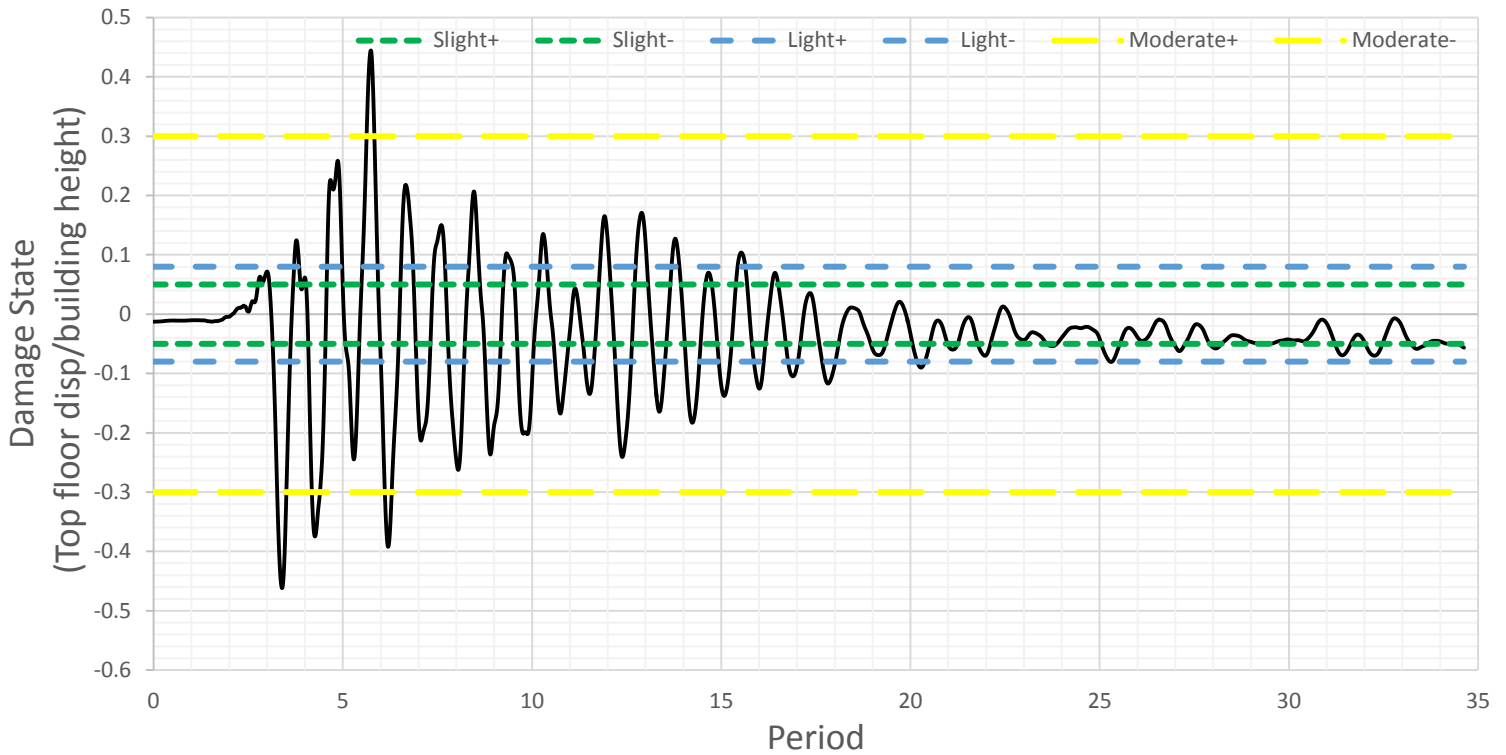


Figure 6.17. Figure showing ISD% and damage limit states (Infilled MRF) for recording station AQA

Record	Max. Roof Displacement	Drift (Disp./height)%	Damage State
AQA-DATA1	-0.11	-0.46	Moderate

Table 6.18. Table of Displacements and damage levels for recording station AQA



2. AQA-Data2 @ Y-Dir

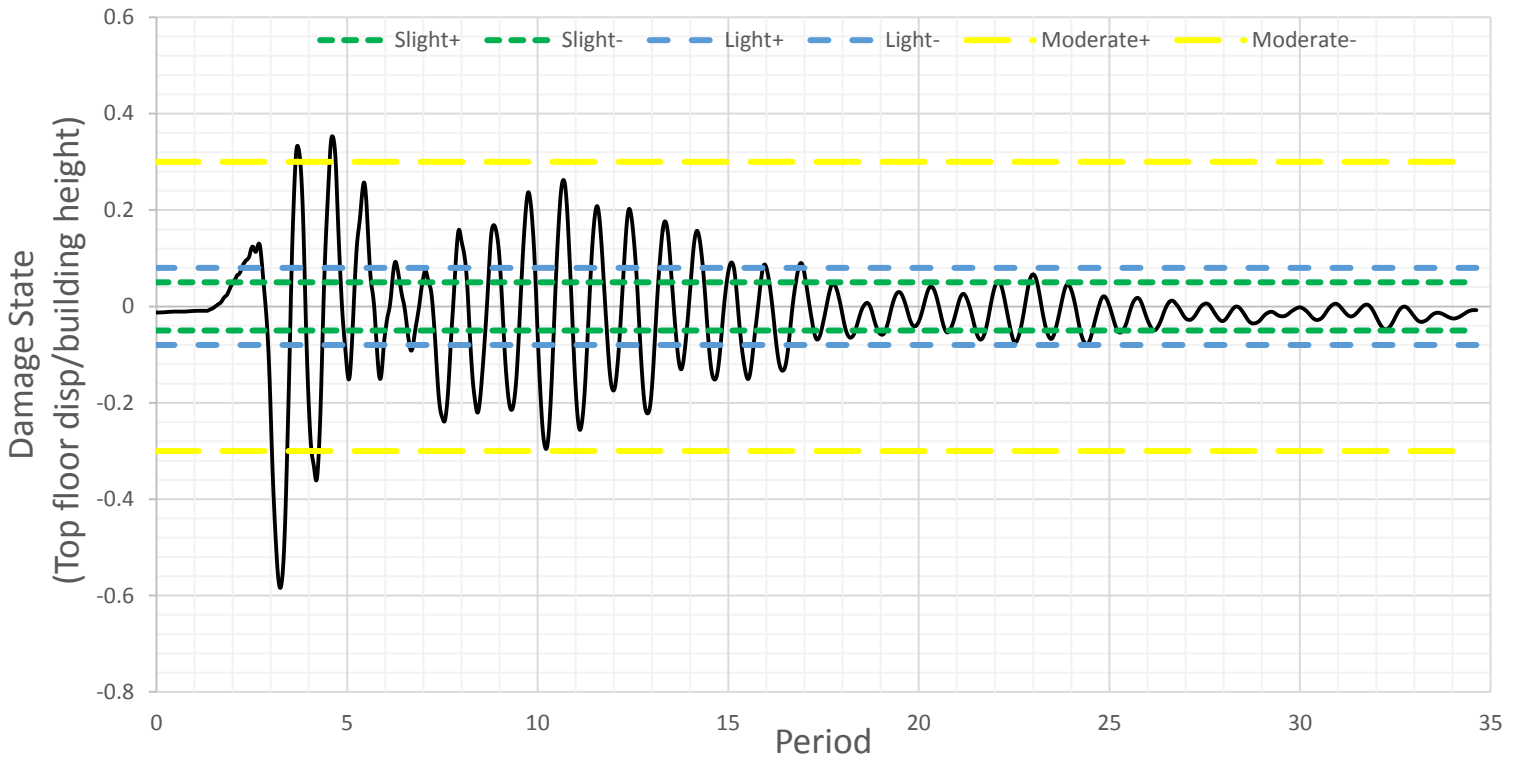


Figure 6.18. Figure showing ISD% and damage limit states (Infilled MRF) for recording station AQA

Record	Max. Roof Displacement	Drift (Disp./height)%	Damage State
AQA-DATA2	-0.14	-0.58	Moderate

Table 6.19. Table of Displacements and damage levels for recording station AQA



6.3.3.2. Record from AQG station

1. AQG-Data1 @ Y-Dir

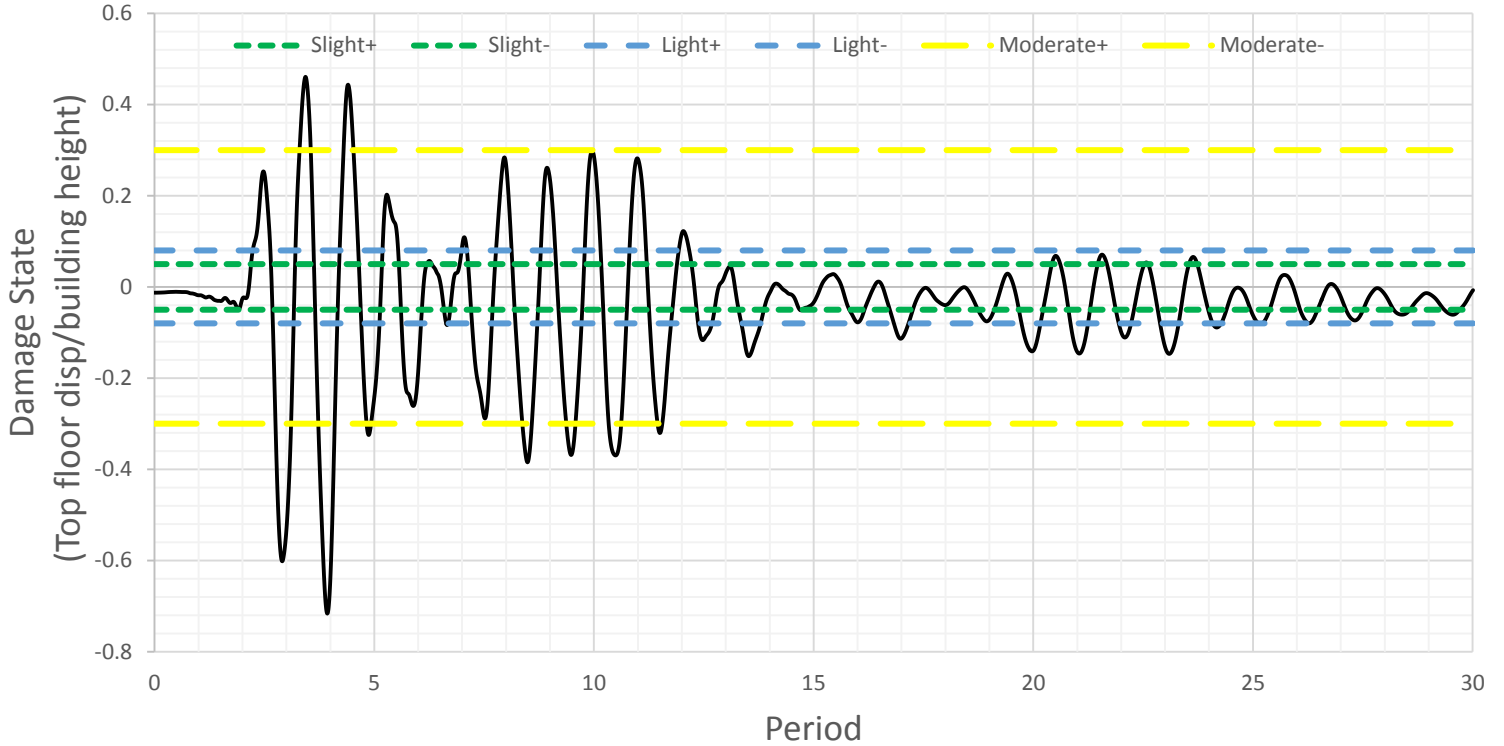


Figure 6.19. Figure showing ISD% and damage limit states (Infilled MRF) for recording station AQG

Record	Max. Roof Displacement	Drift (Disp./height)%	Damage State
AQG-DATA1	-0.17	-0.72	Moderate

Table 6.20. Table of Displacements and damage levels for recording station AQG

2. AQG-Data2 @ Y-Dir

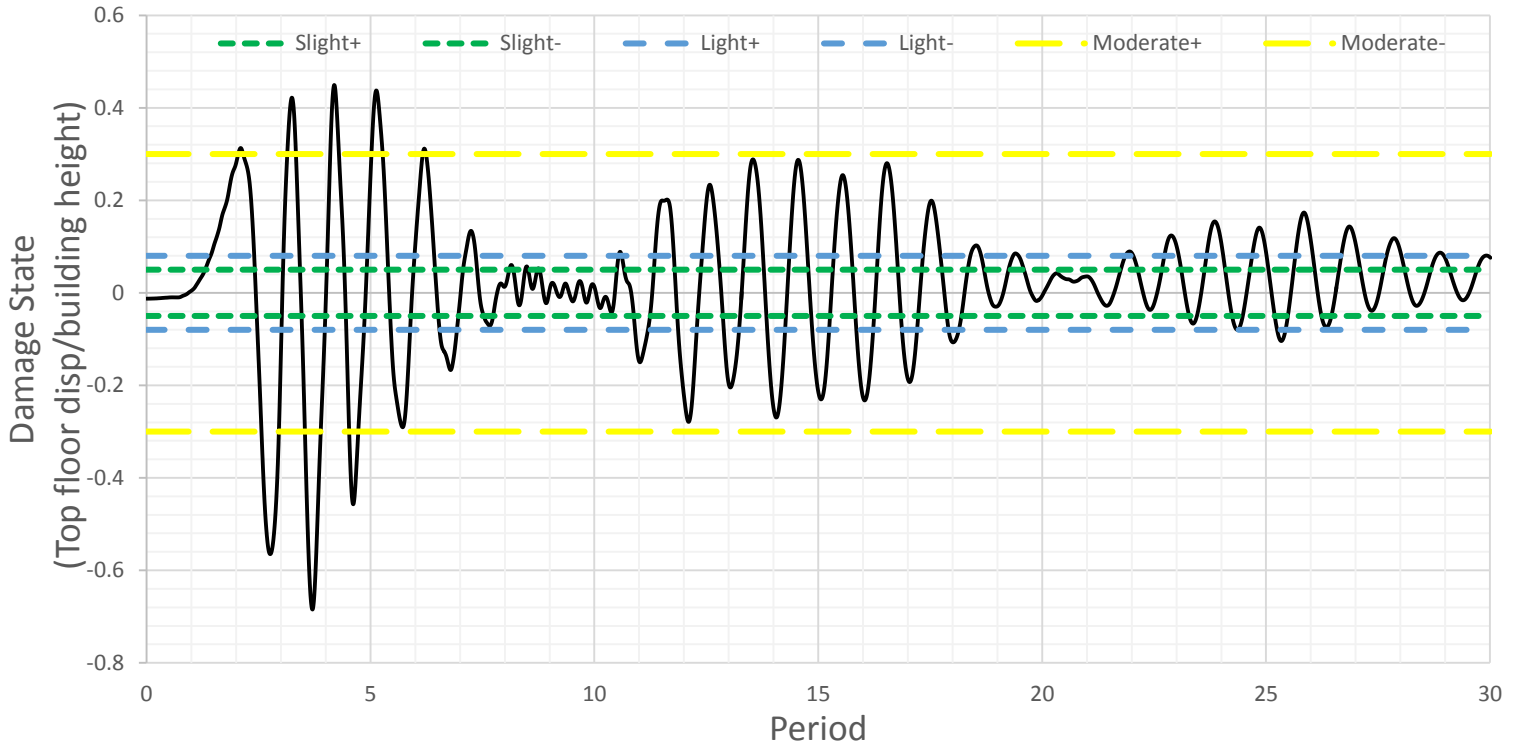


Figure 6.20. Figure showing ISD% and damage limit states (Infilled MRF) for recording station AQG

Record	Max. Roof Displacement	Drift (Disp./height)%	Damage State
AQG-DATA2	-0.16	-0.68	Moderate

Table 6.21. Table of Displacements and damage levels for recording station AQG



6.3.3.3. Record from AQK station

1. AQK-Data1 @ Y-Dir

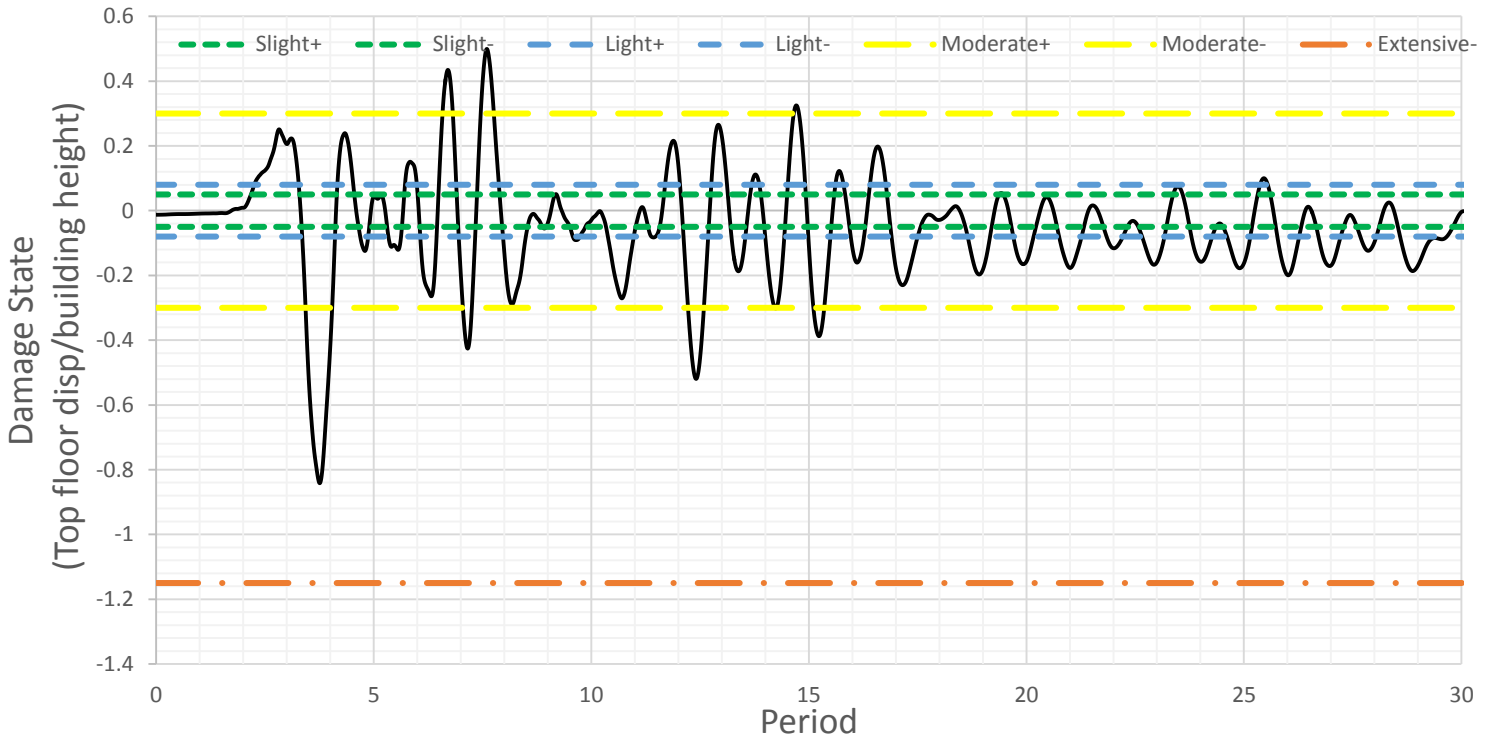


Figure 6.21. Figure showing ISD% and damage limit states (Infilled MRF) for recording station AQK

Record	Max. Roof Displacement	Drift (Disp./height)%	Damage State
AQK-DATA1	-0.20	-0.84	Moderate

Table 6.22. Table of Displacements and damage levels for recording station AQK



2. AQK-Data2 @ Y-Dir

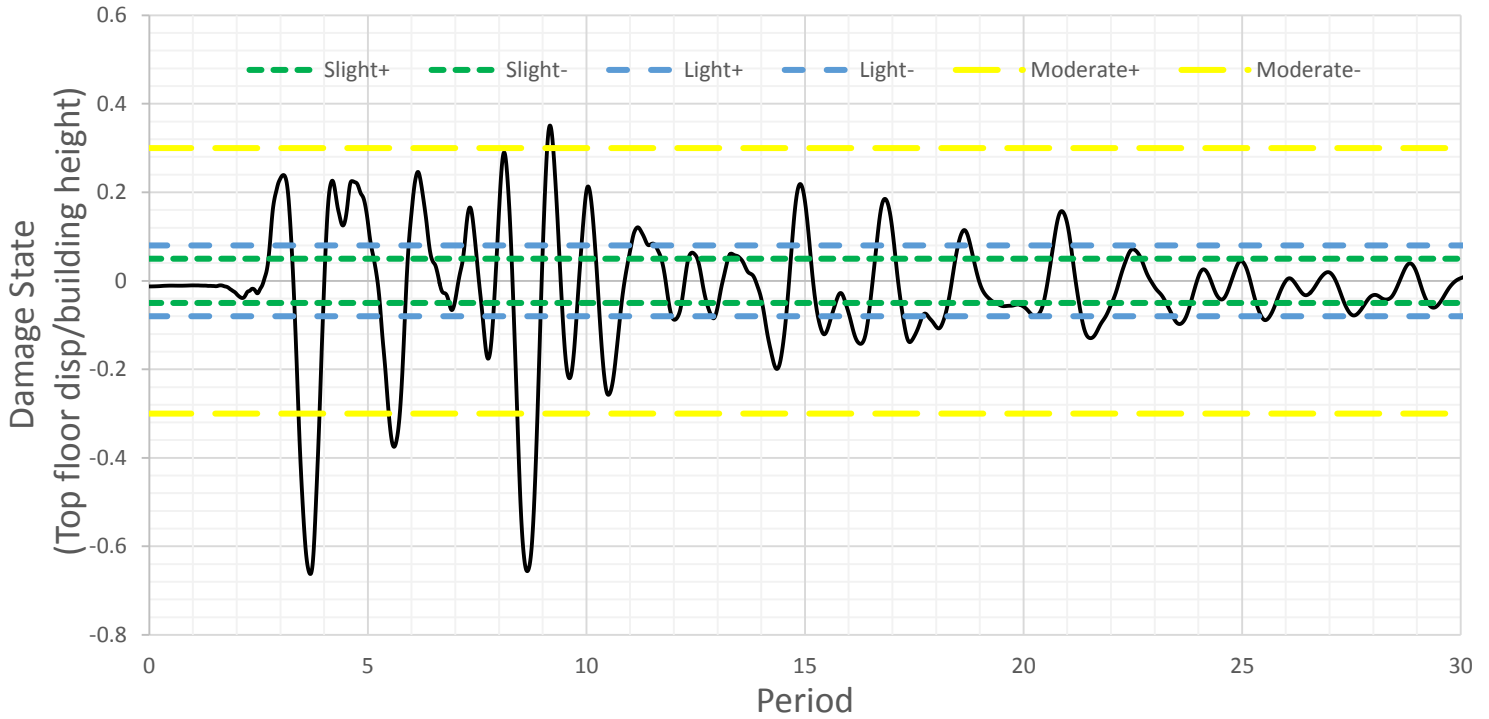


Figure 6.22. Figure showing ISD% and damage limit states (Infilled MRF) for recording station AQK

Record	Max. Roof Displacement	Drift (Disp./height)%	Damage State
AQK-DATA2	-0.16	-0.66	Moderate

Table 6.23. Table of Displacements and damage levels for recording station AQK



6.3.3.4. Record from AQVstation

1. AQV-Data1 @ Y-Dir

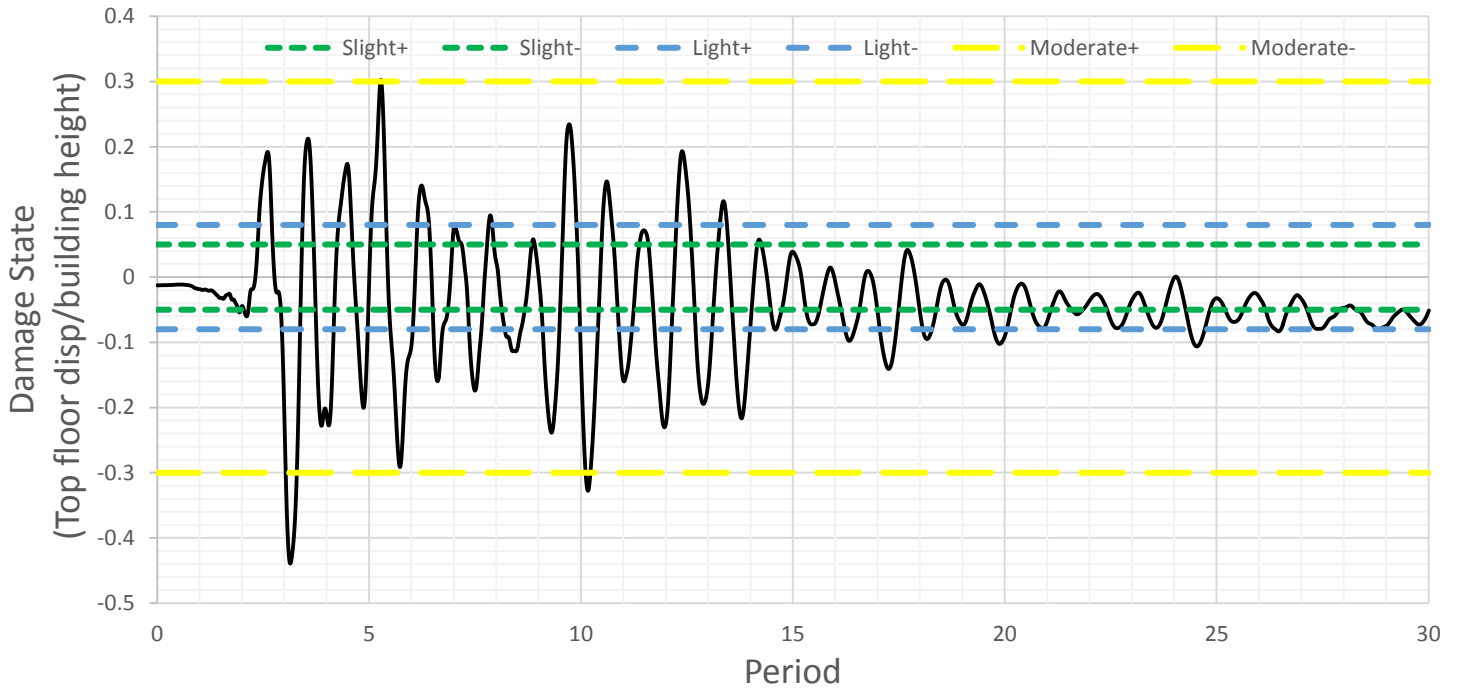


Figure 6.23. Figure showing ISD% and damage limit states (Infilled MRF) for recording station AQV

Record	Max. Roof Displacement	Drift (Disp./height)%	Damage State
AQV-DATA1	-0.11	-0.44	Moderate

Table 6.24. Table of Displacements and damage levels for recording station AQV



2. AQV-Data2 @ Y-Dir

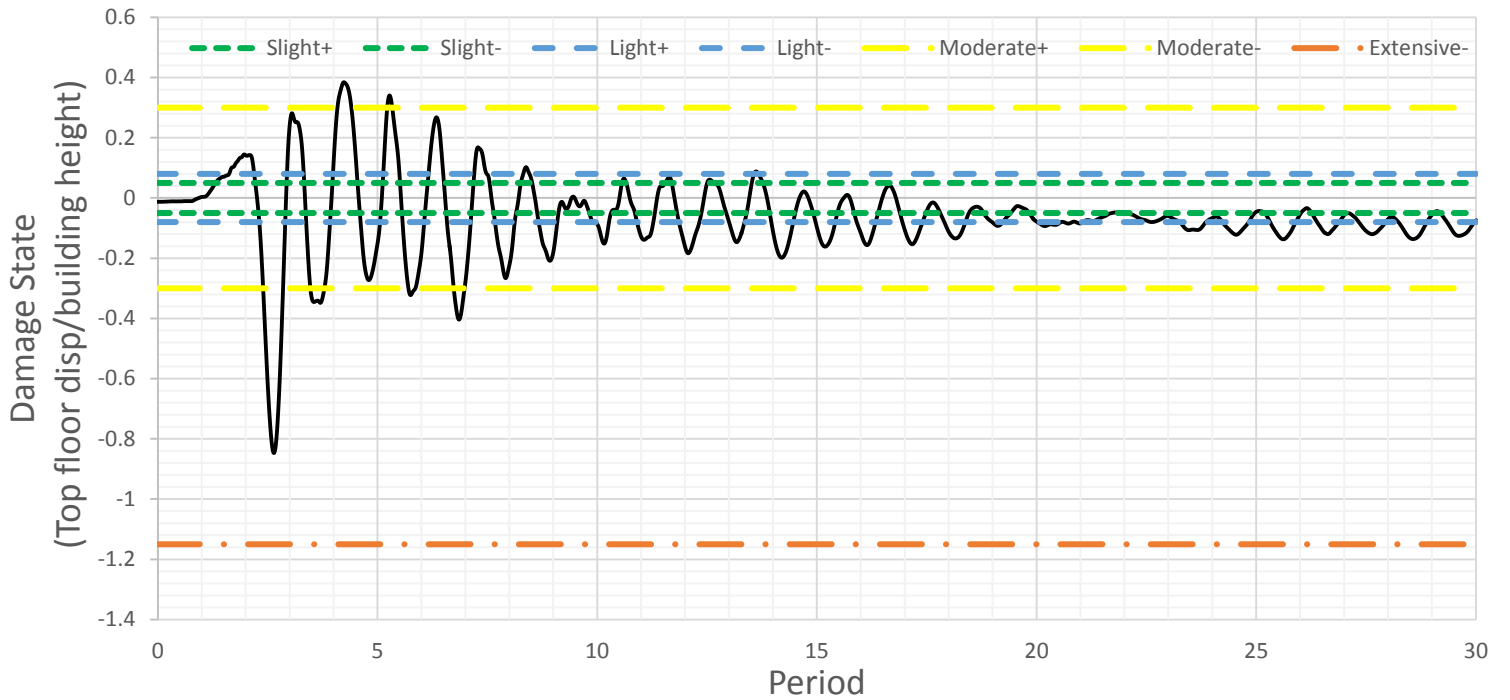


Figure 6.24. Figure showing ISD% and damage limit states (Infilled MRF) for recording station AQV

Record	Max. Roof Displacement	Drift (Disp./height)%	Damage State
AQV-DATA2	-0.20	-0.85	Moderate

Table 6.25. Table of Displacements and damage levels for recording station AQV



6.3.4. Norcia earthquake in Y-Direction
6.3.4.1. Record from ACC station

1. ACC-Data1 @ Y-Dir

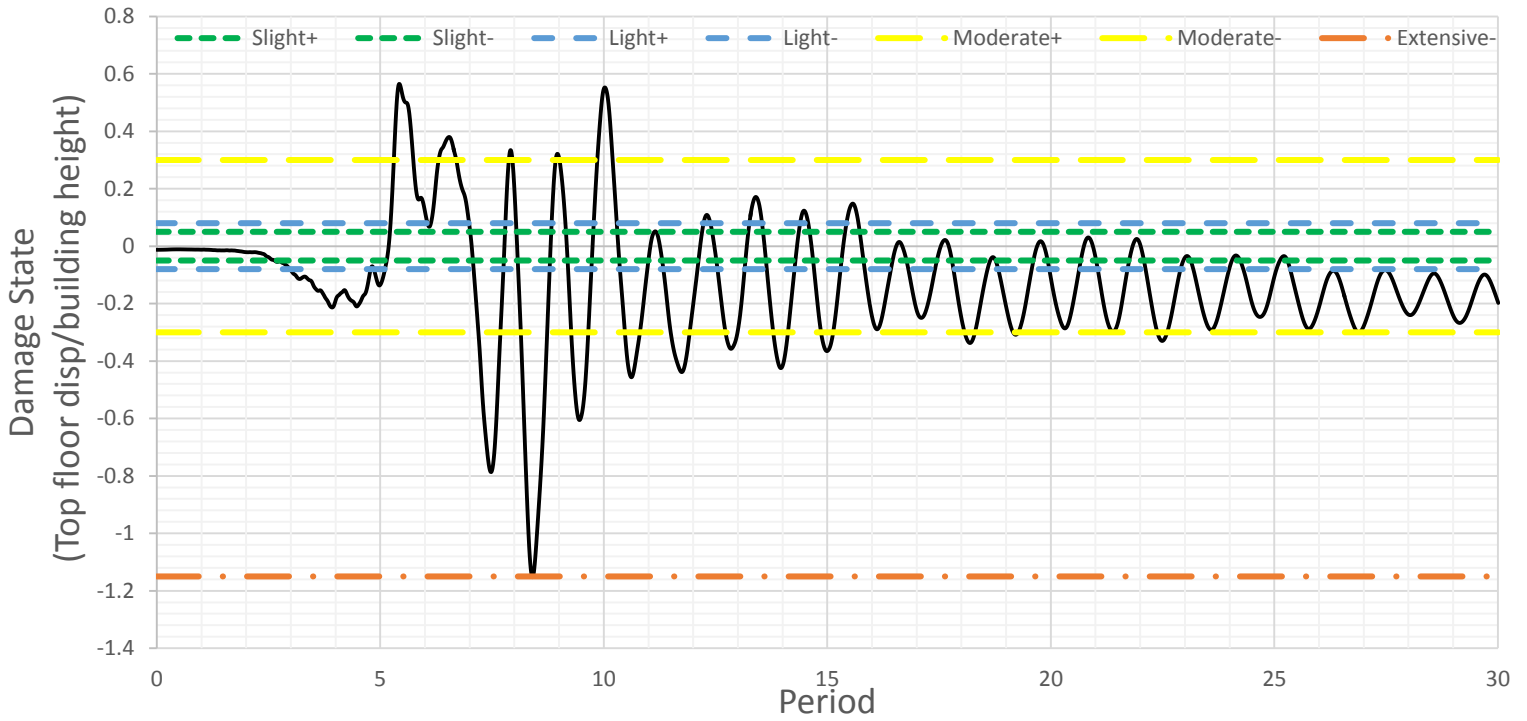


Figure 6.25. Figure showing ISD% and damage limit states (Infilled MRF) for recording station ACC

Record	Max. Roof Displacement	Drift (Disp./height)%	Damage State
ACC-DATA1	-0.28	-1.15	Extensive

Table 6.26. Table of Displacements and damage levels for recording station ACC



2. ACC-Data2 @ Y-Dir

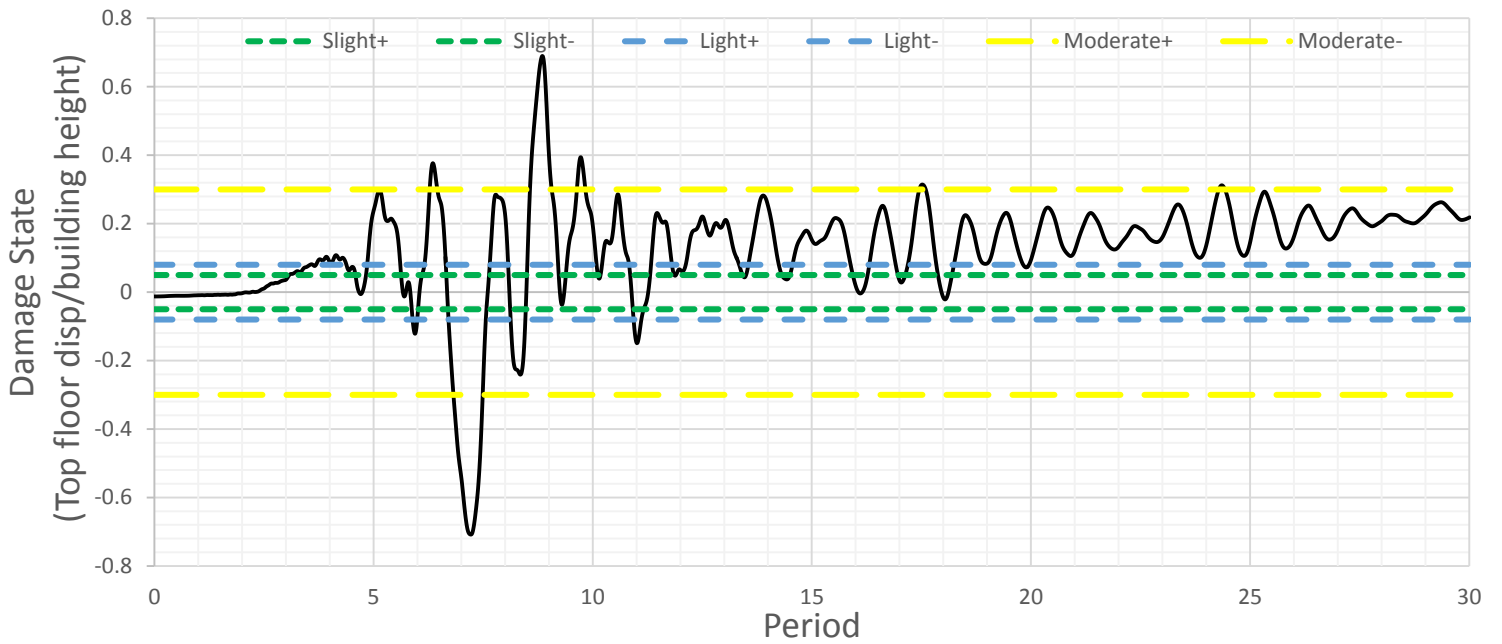


Figure 6.26. Figure showing ISD% and damage limit states (Infilled MRF) for recording station ACC

Record	Max. Roof Displacement	Drift (Disp./height)%	Damage State
ACC-DATA2	-0.17	-0.71	Moderate

Table 6.27. Table of Displacements and damage levels for recording station ACC

6.3.4.2. Record from AMT station

1. AMT-Data1 @ Y-Dir

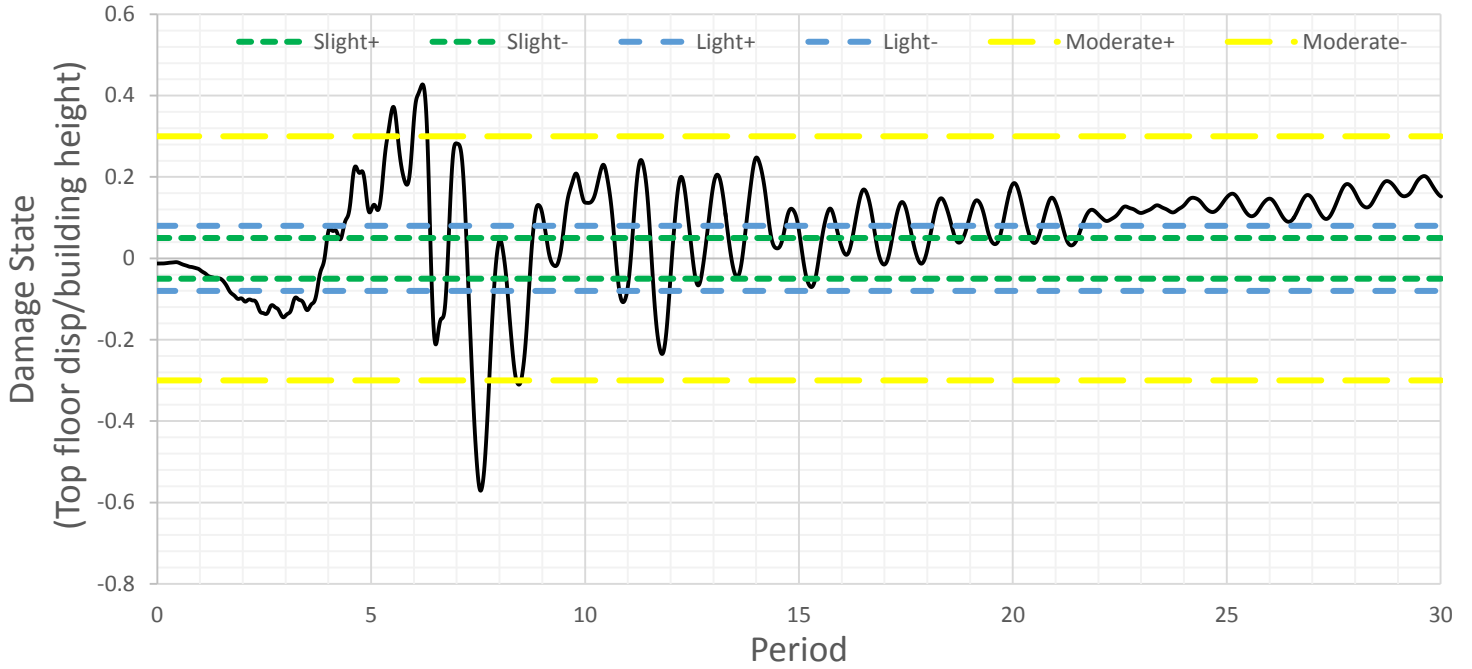


Figure 6.27. Figure showing ISD% and damage limit states (Infilled MRF) for recording station AMT

Record	Max. Roof Displacement	Drift (Disp./height)%	Damage State
AMT-DATA1	-0.14	-0.57	Moderate

Table 6.28. Table of Displacements and damage levels for recording station AMT



2. AMT-Data2 @ Y-Dir

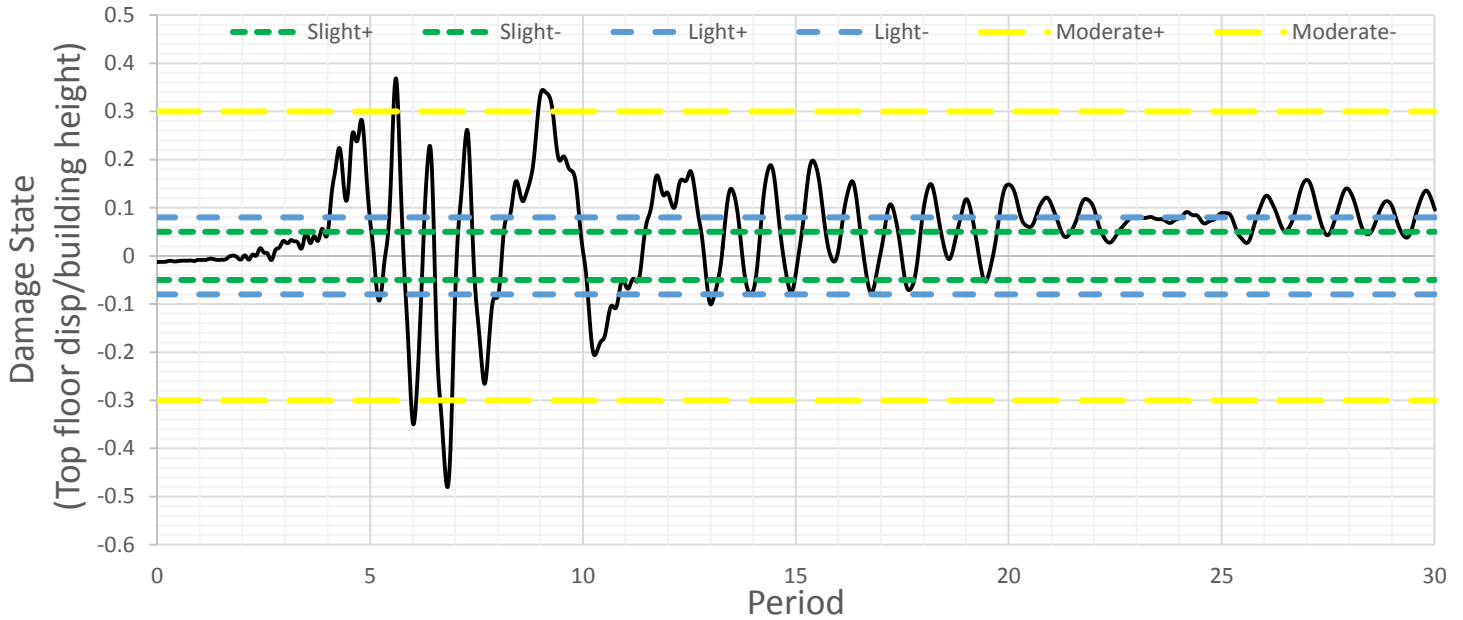


Figure 6.28. Figure showing ISD% and damage limit states (Infilled MRF) for recording station AMT

Record	Max. Roof Displacement	Drift (Disp./height)%	Damage State
AMT-DATA2	-0.12	-0.48	Moderate

Table 6.29. Table of Displacements and damage levels for recording station AMT



6.3.4.3. Record from T1201 station

1. T1201-Data1 @ Y-Dir

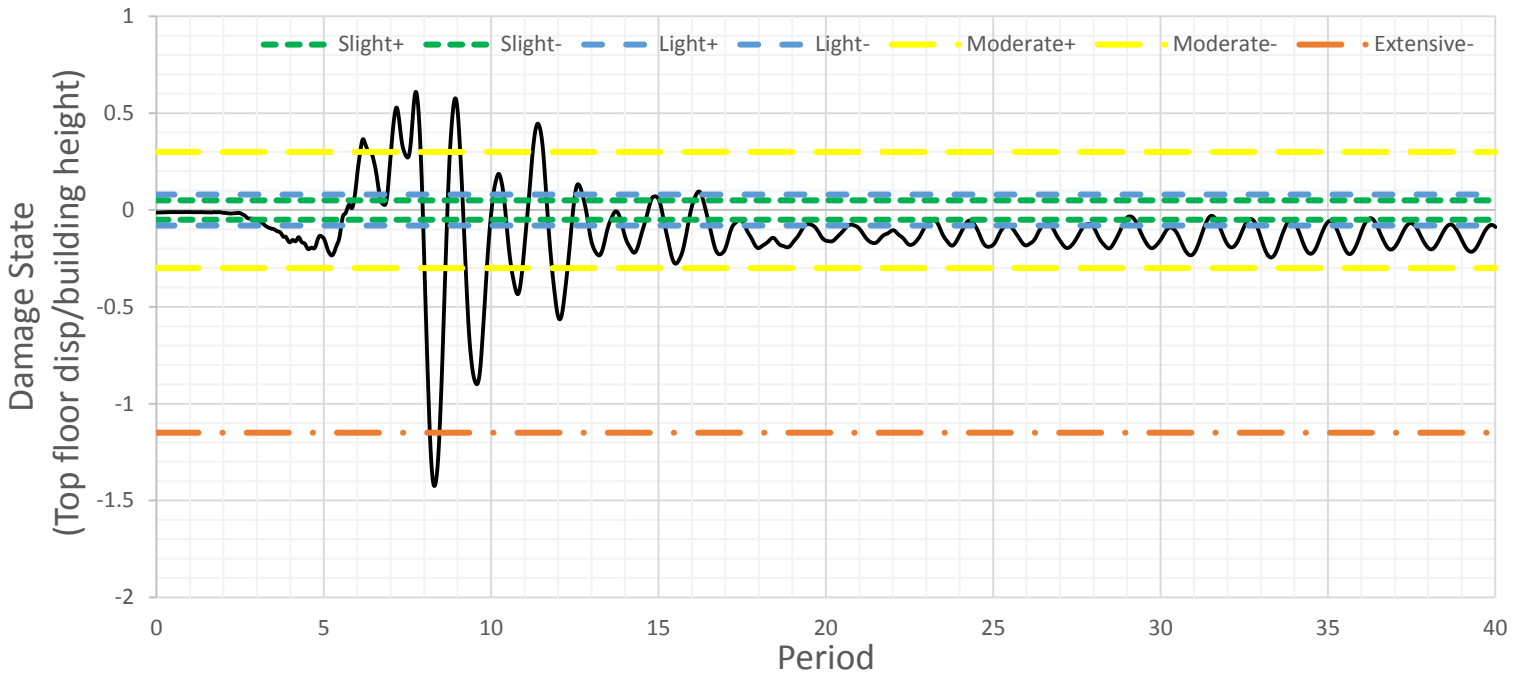


Figure 6.29. Figure showing ISD% and damage limit states (Infilled MRF) for recording station T1201

Record	Max. Roof Displacement	Drift (Disp./height)%	Damage State
T1201-DATA1	-0.34	-1.43	Extensive

Table 6.30. Table of Displacements and damage levels for recording station T1201



2. T1201-Data2 @ Y-Dir

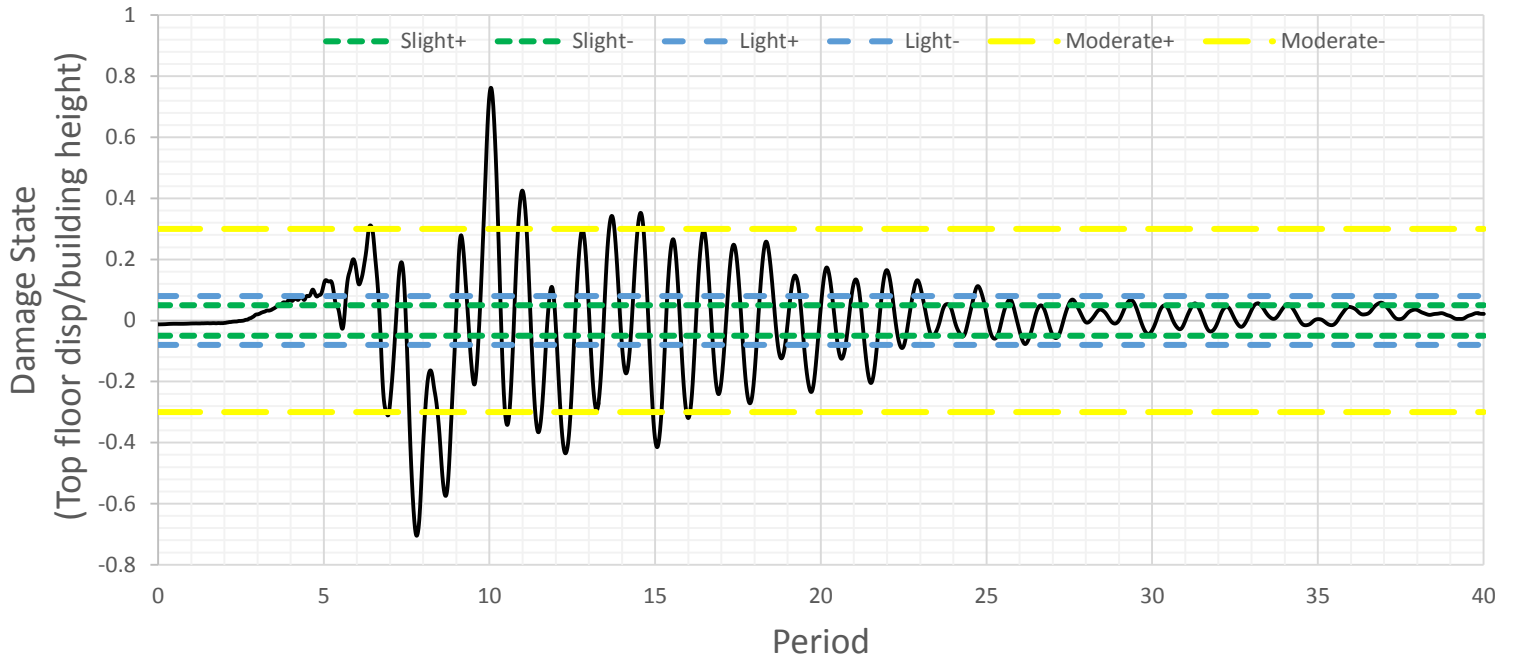


Figure 6.30. Figure showing ISD% and damage limit states (Infilled MRF) for recording station T1201

Record	Max. Roof Displacement	Drift (Disp./height)%	Damage State
T1201-DATA2	0.18	0.76	Moderate

Table 6.31. Table of Displacements and damage levels for recording station T1201



6.3.4.4. Record from NRC station

1. NRC-Data1 @ Y-Dir

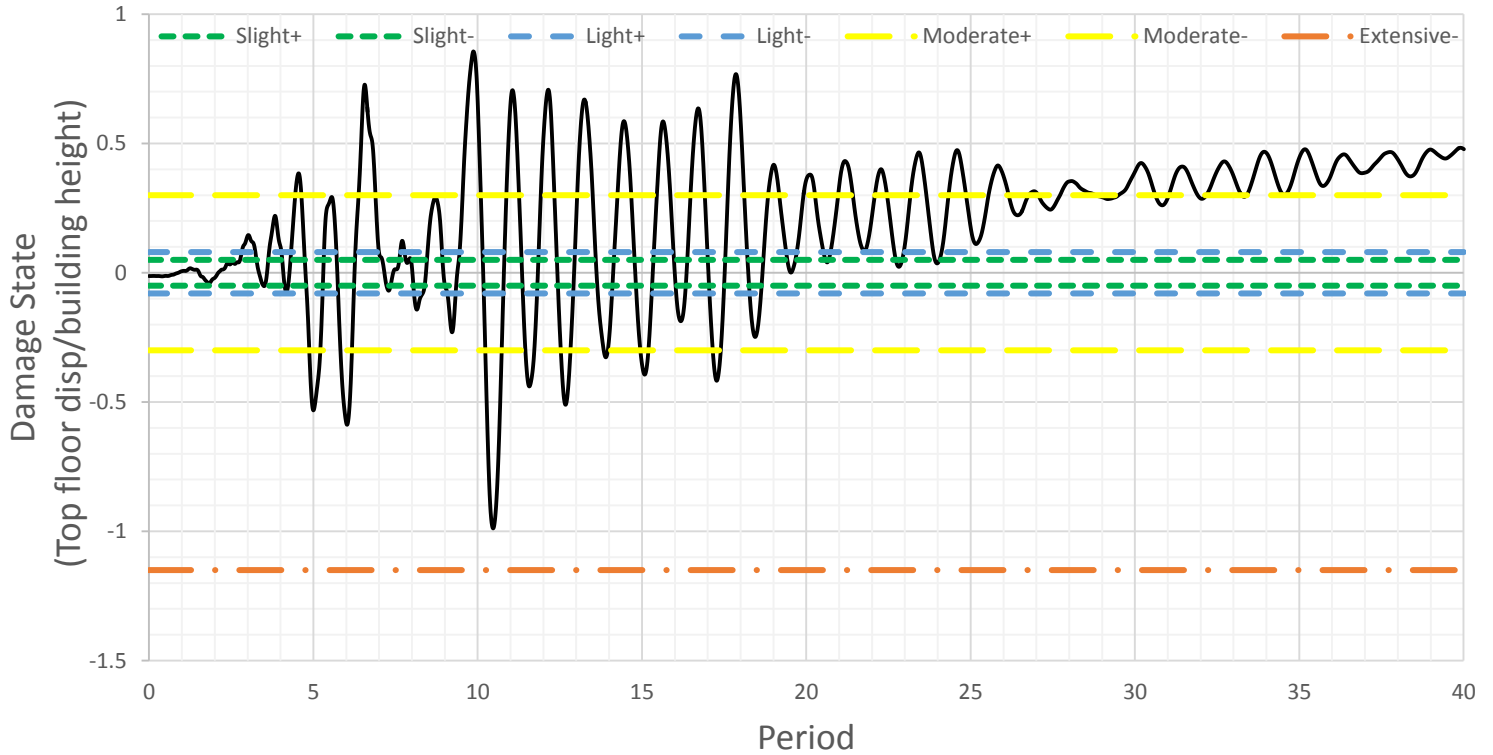


Figure 6.31. Figure showing ISD% and damage limit states (Infilled MRF) for recording station NRC

Record	Max. Roof Displacement	Drift (Disp./height)%	Damage State
NRC-DATA1	-0.24	-0.99	Extensive

Table 6.32. Table of Displacements and damage levels for recording station NRC



2. NRC-Data2 @ Y-Dir

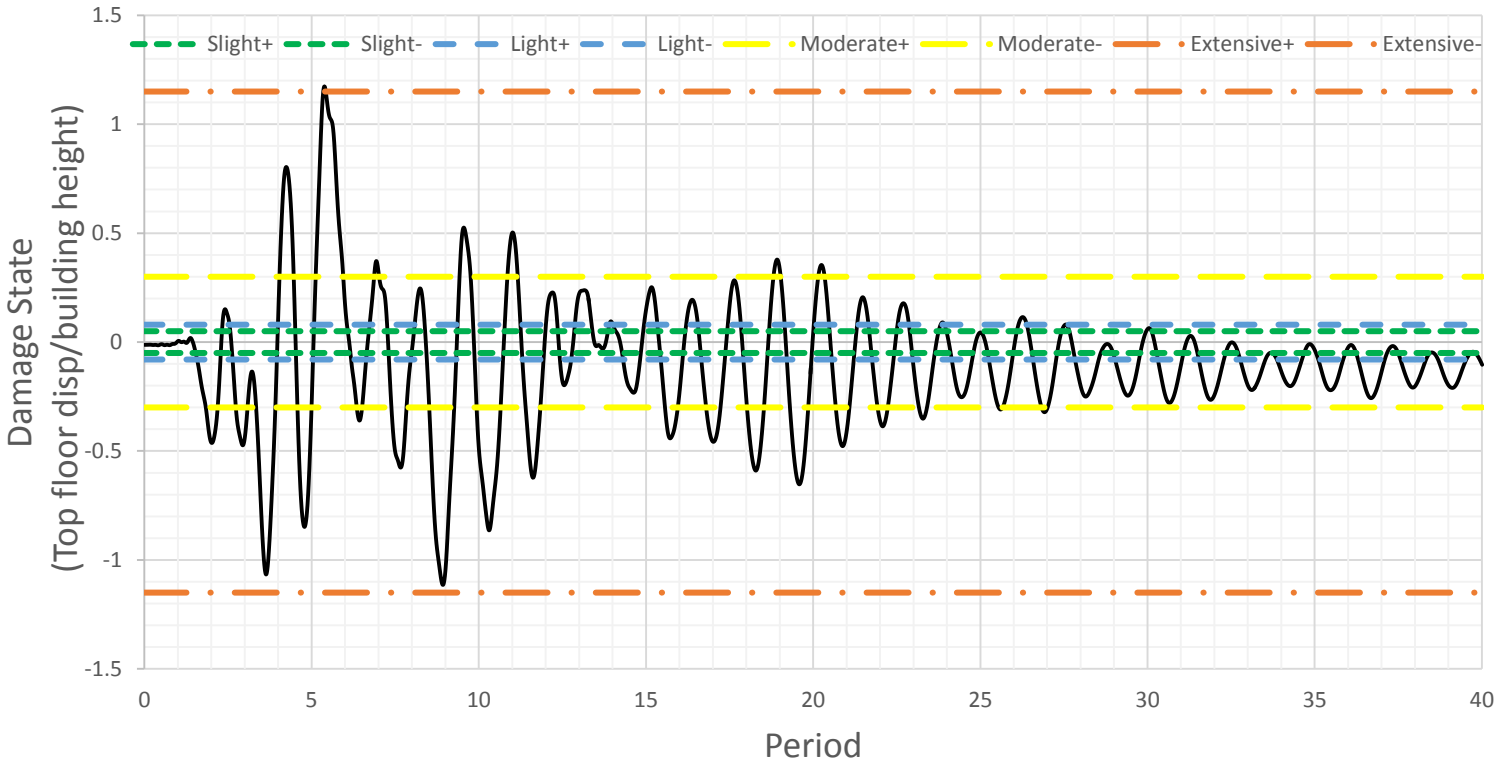


Figure 6.32. Figure showing ISD% and damage limit states (Infilled MRF) for recording station NRC

Record	Max. Roof Displacement	Drift (Disp./height)%	Damage State
NRC-DATA2	0.28	1.17	Extensive

Table 6.33. Table of Displacements and damage levels for recording station NRC



6.4. Dynamic time history results of strengthened building

6.4.1. Aquila Earthquake in Y-Direction

6.4.1.1. Record from AQA station

1. AQA-Data1 @Y-Dir

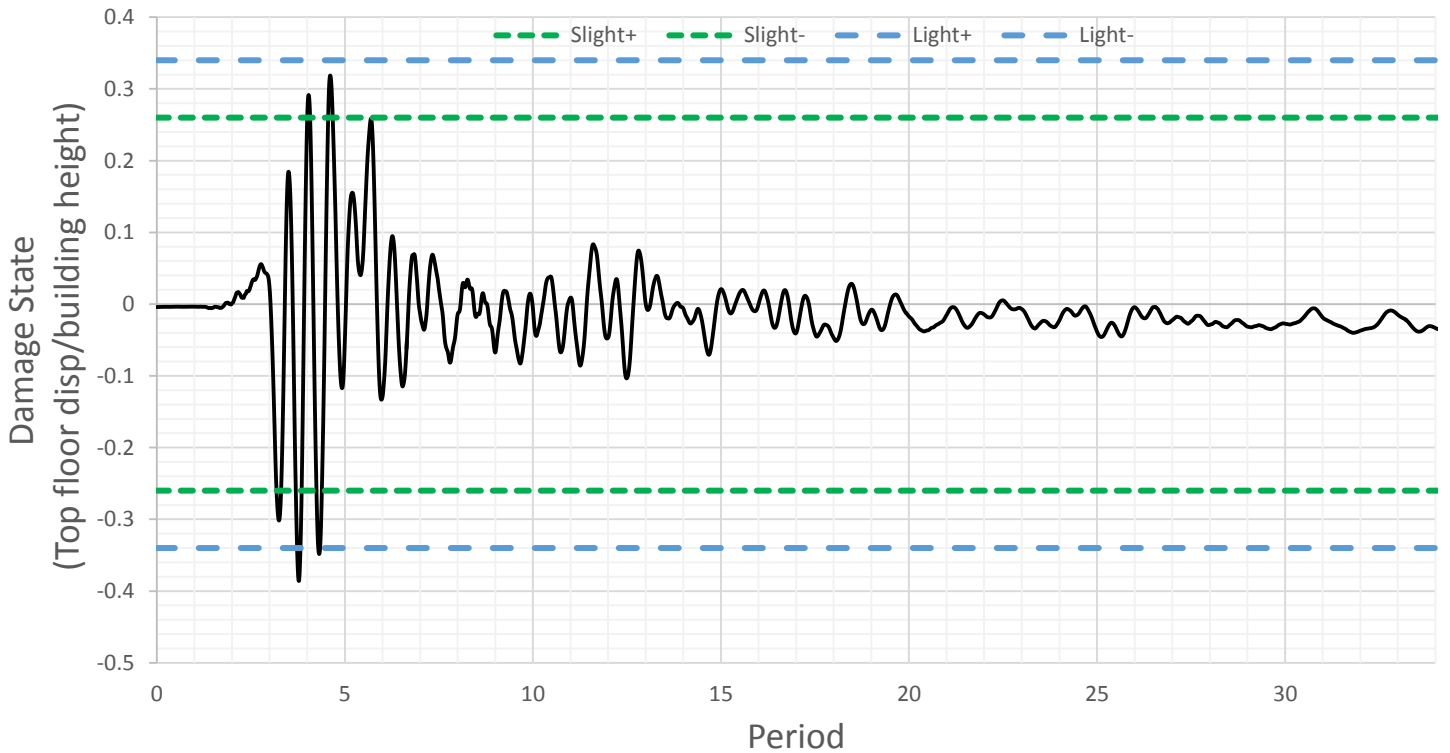


Figure 6.33. Figure showing ISD% and damage limit states (Shear walls) for recording station AQA

Record	Max. Roof Displacement	Drift (Disp./height)%	Damage State
AQA-DATA1	-0.09	-0.39	Light

Table 6.34. Table of Displacements and damage levels for recording station AQA



2. AQA-Data2 @Y-Dir

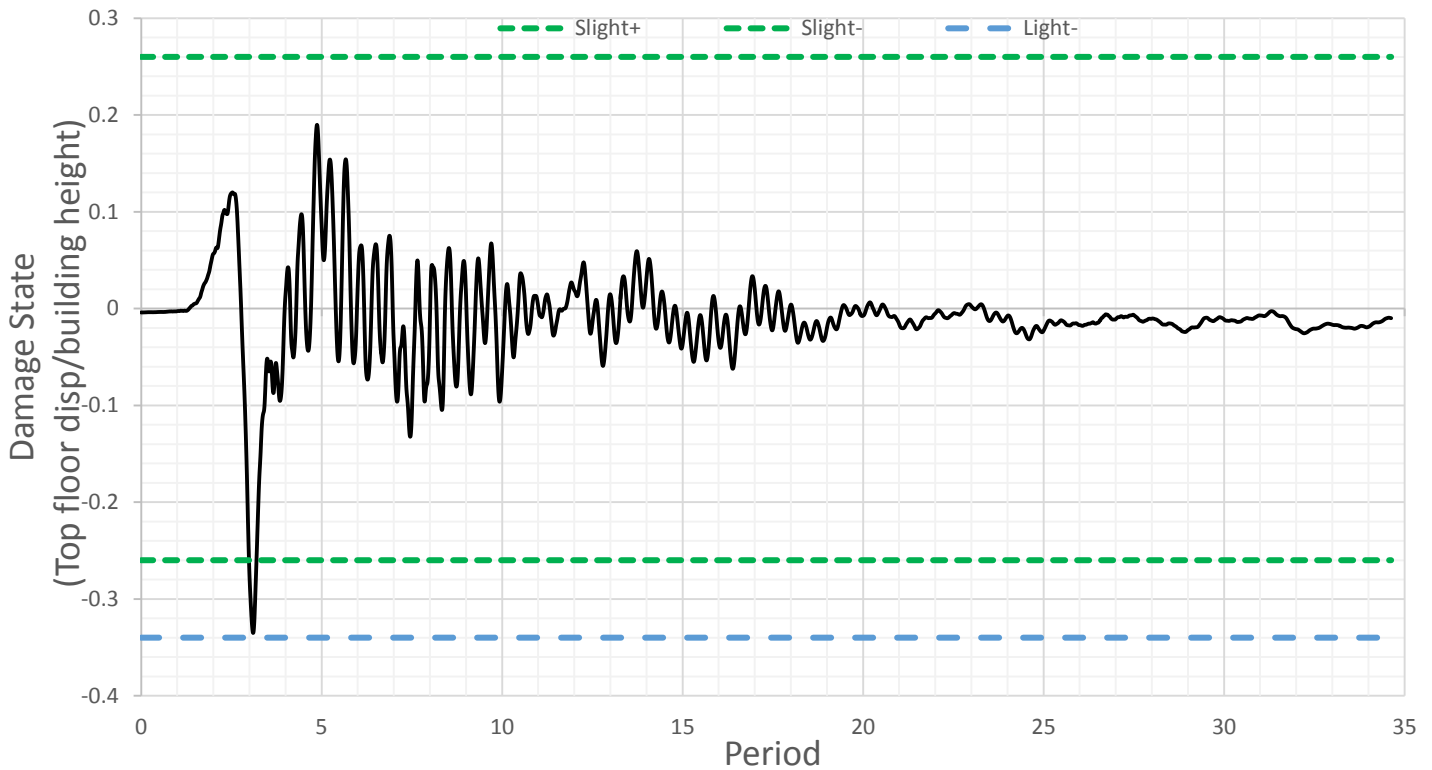


Figure 6.34. Figure showing ISD% and damage limit states (Shear walls) for recording station AQA

Record	Max. Roof Displacement	Drift (Disp./height)%	Damage State
AQA-DATA2	-0.08	-0.34	Light

Table 6.35. Table of Displacements and damage levels for recording station AQA

6.4.1.2. Record from AQG station

1. AQG-Data1 @Y-Dir

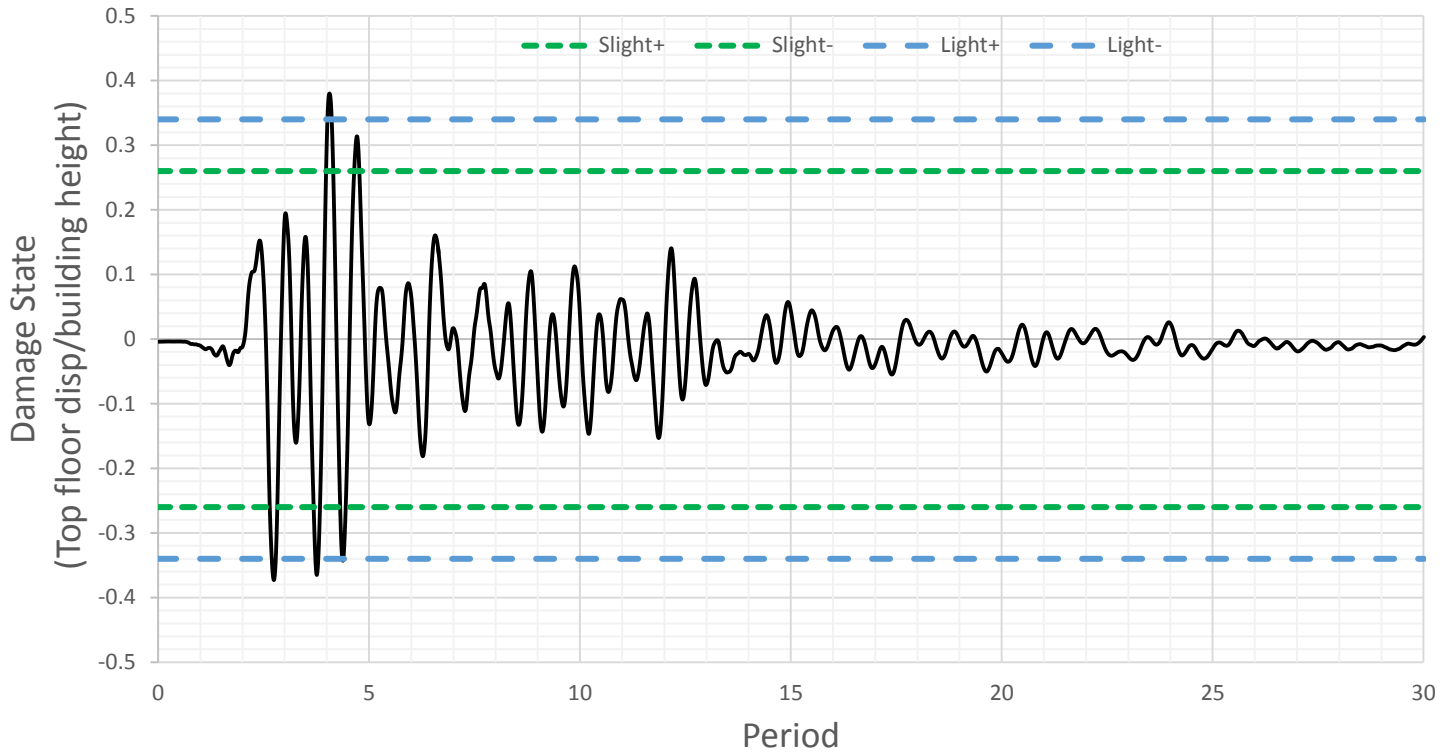


Figure 6.35. Figure showing ISD% and damage limit states (Shear walls) for recording station AQG

Record	Max. Roof Displacement	Drift (Disp./height)%	Damage State
AQG-DATA1	0.09	0.38	Light

Table 6.36. Table of Displacements and damage levels for recording station AQG



2. AQG-Data2 @Y-Dir

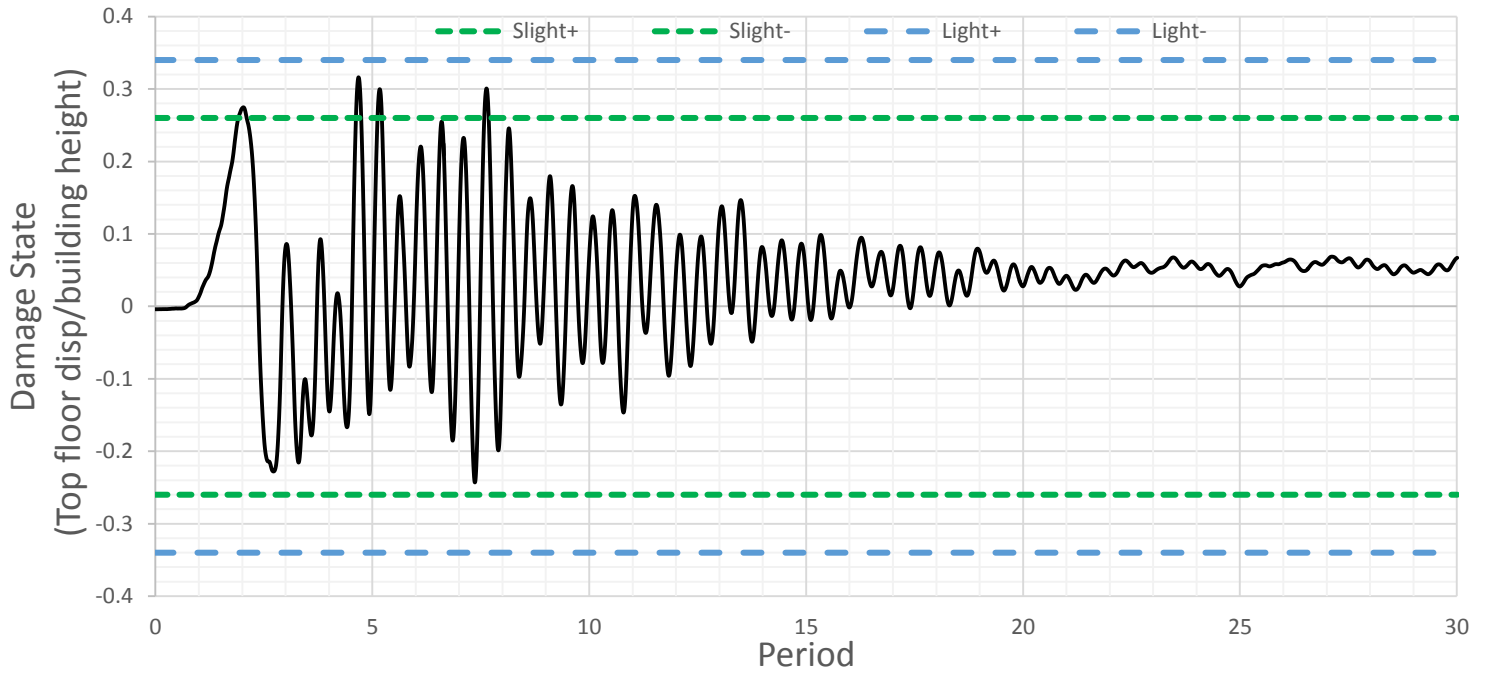


Figure 6.36. Figure showing ISD% and damage limit states (Shear walls) for recording station AQG

Record	Max. Roof Displacement	Drift (Disp./height)%	Damage State
AQG-DATA2	-0.06	-0.24	Slight

Table 6.37. Table of Displacements and damage levels for recording station AQG



6.4.1.3. Record from AQK station

1. AQK-Data1 @Y-Dir

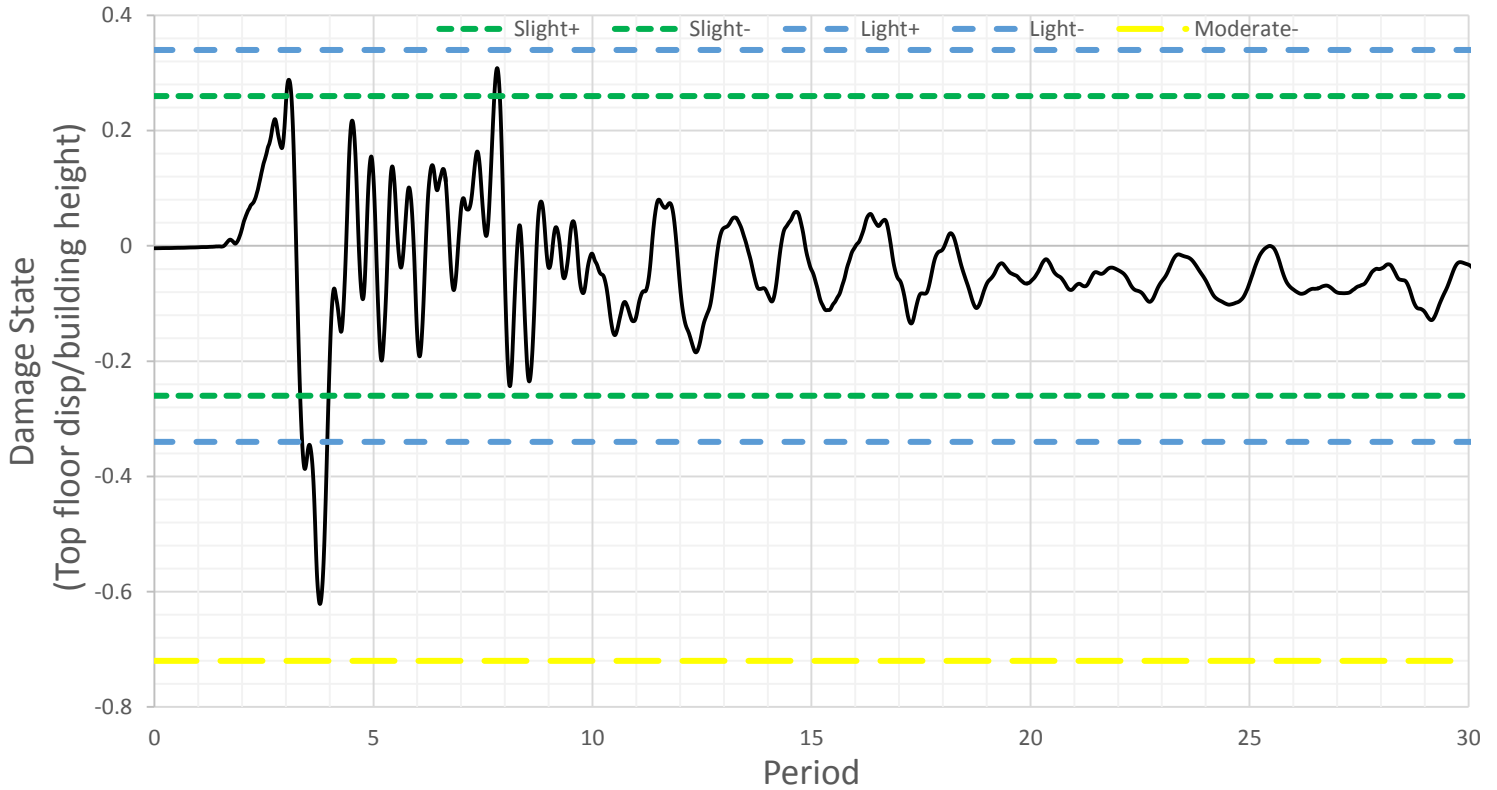


Figure 6.37. Figure showing ISD% and damage limit states (Shear walls) for recording station AQK

Record	Max. Roof Displacement	Drift (Disp./height)%	Damage State
AQK-DATA1	-0.15	-0.62	Moderate

Table 6.38. Table of Displacements and damage levels for recording station AQK

2. AQK-Data2 @Y-Dir

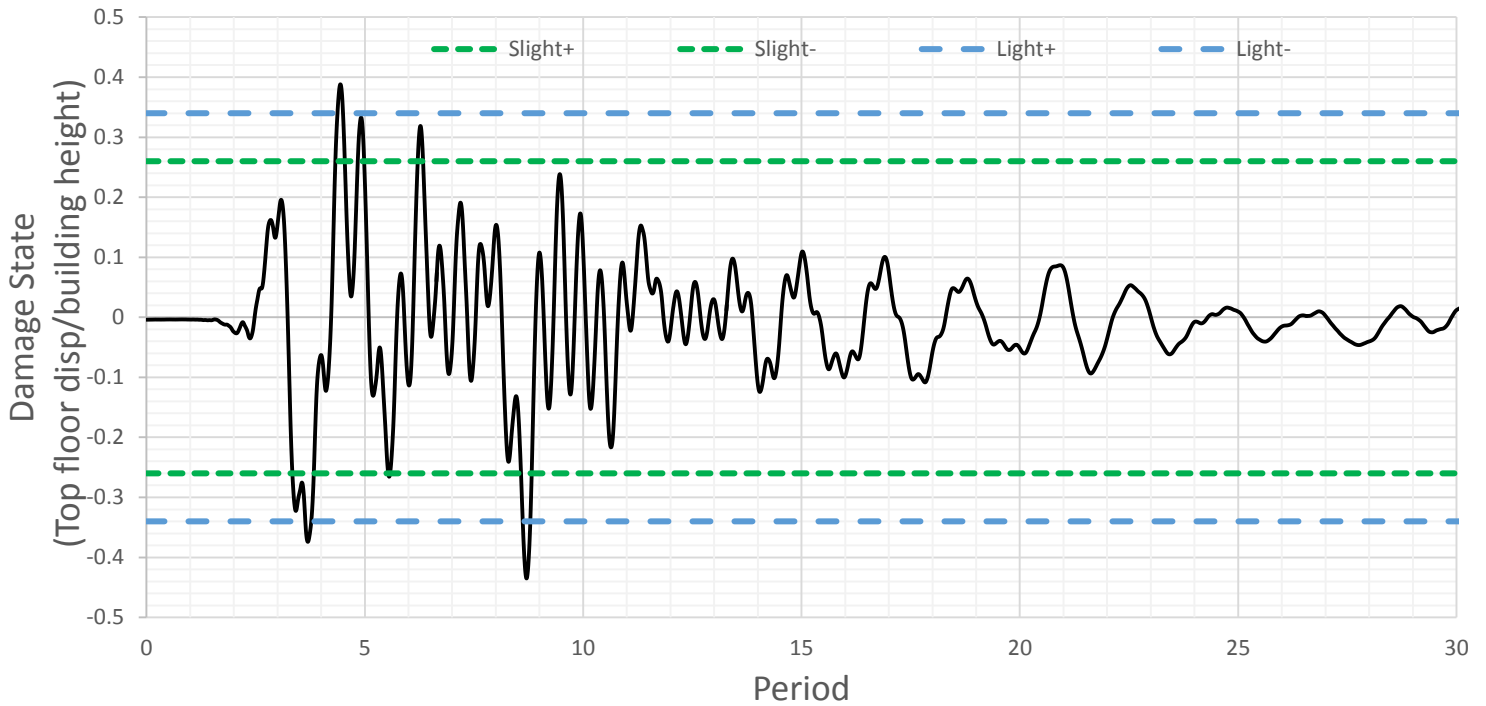


Figure 6.38. Figure showing ISD% and damage limit states (Shear walls) for recording station AQK

Record	Max. Roof Displacement	Drift (Disp./height)%	Damage State
AQK-DATA2	-0.10	-0.43	Light

Table 6.39. Table of Displacements and damage levels for recording station AQK

6.4.1.4. Record from AQV station

1. AQV-Data1 @Y-Dir.

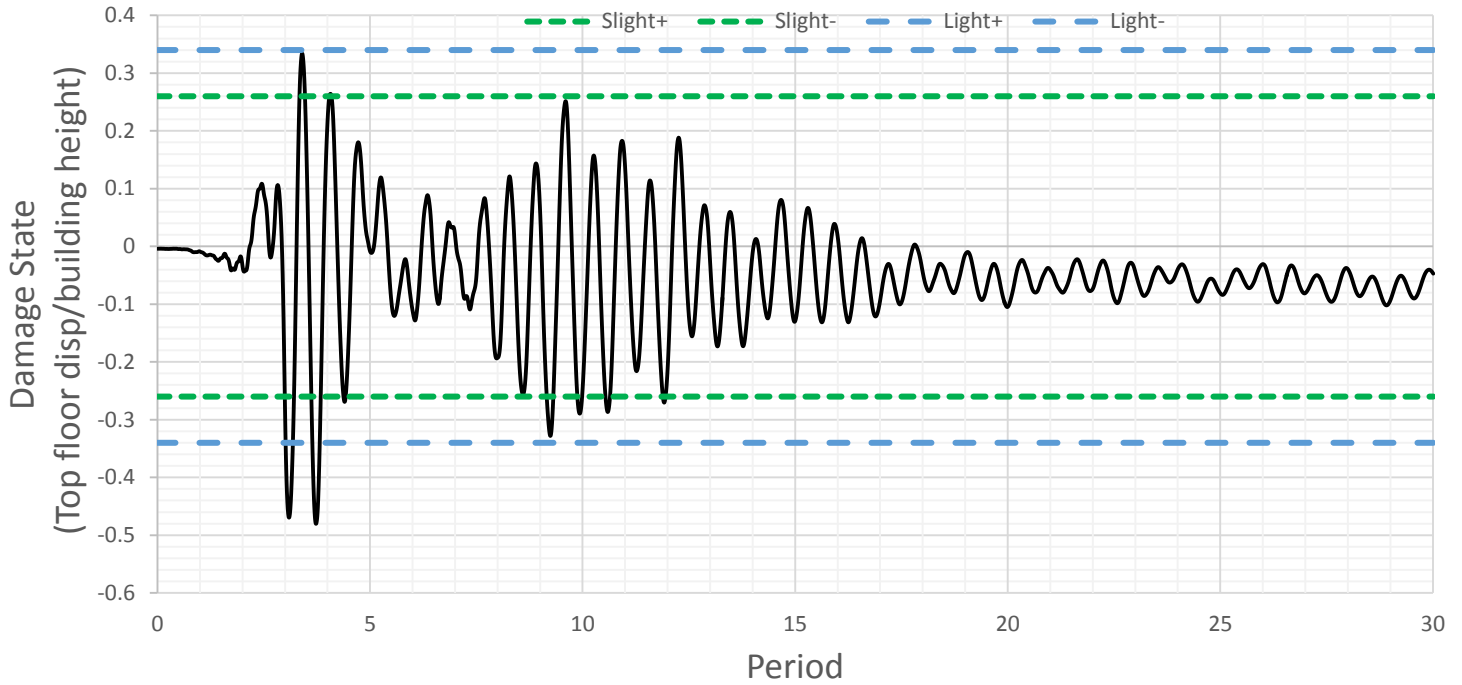


Figure 6.39. Figure showing ISD% and damage limit states (Shear walls) for recording station AQV

Record	Max. Roof Displacement	Drift (Disp./height)%	Damage State
AQV-DATA1	-0.12	-0.48	Light

Table 6.40. Table of Displacements and damage levels for recording station AQV



2. AQV-Data2 @Y-Dir.

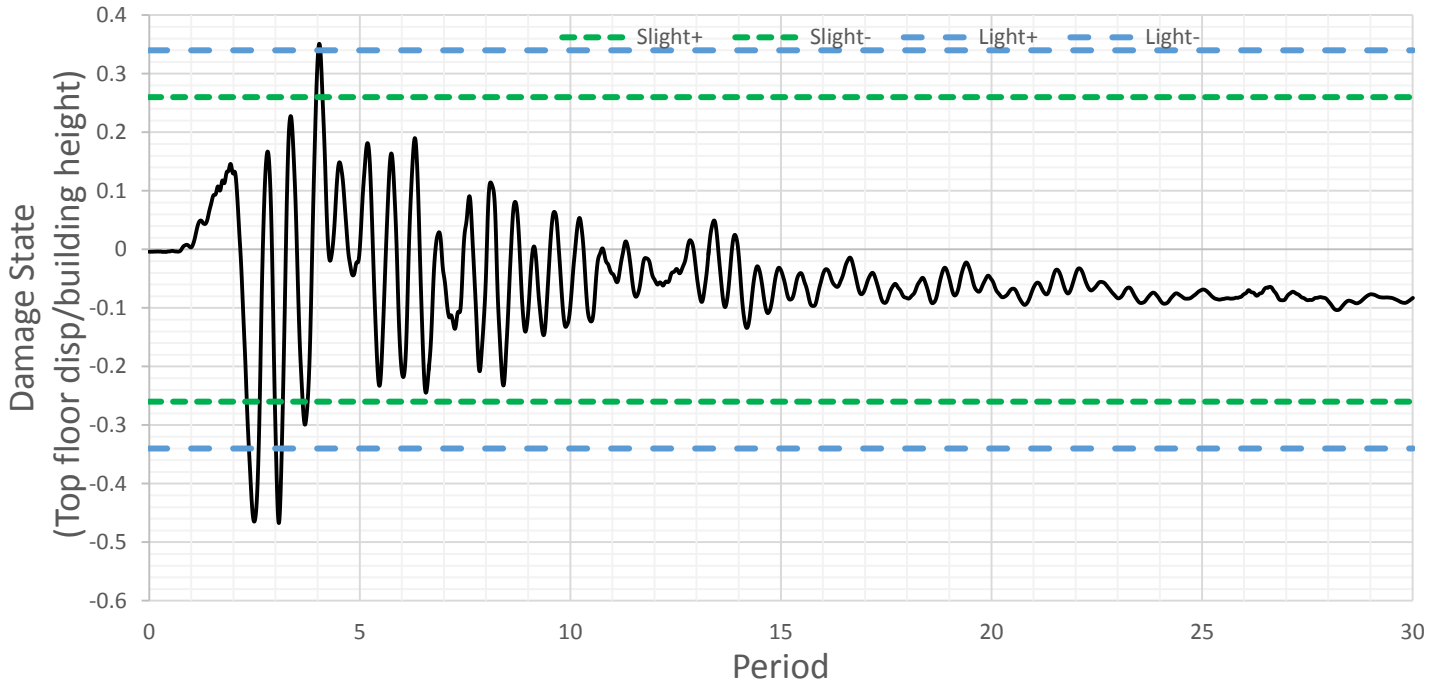


Figure 6.40. Figure showing ISD% and damage limit states (Shear walls) for recording station AQV

Record	Max. Roof Displacement	Drift (Disp./height)%	Damage State
AQV-DATA2	-0.11	-0.47	Light

Table 6.41. Table of Displacements and damage levels for recording station AQV



6.4.2. Norcia Earthquake in Y-Direction
 6.4.2.1. Record from ACC station

1. ACC-Data1 @Y-Dir.

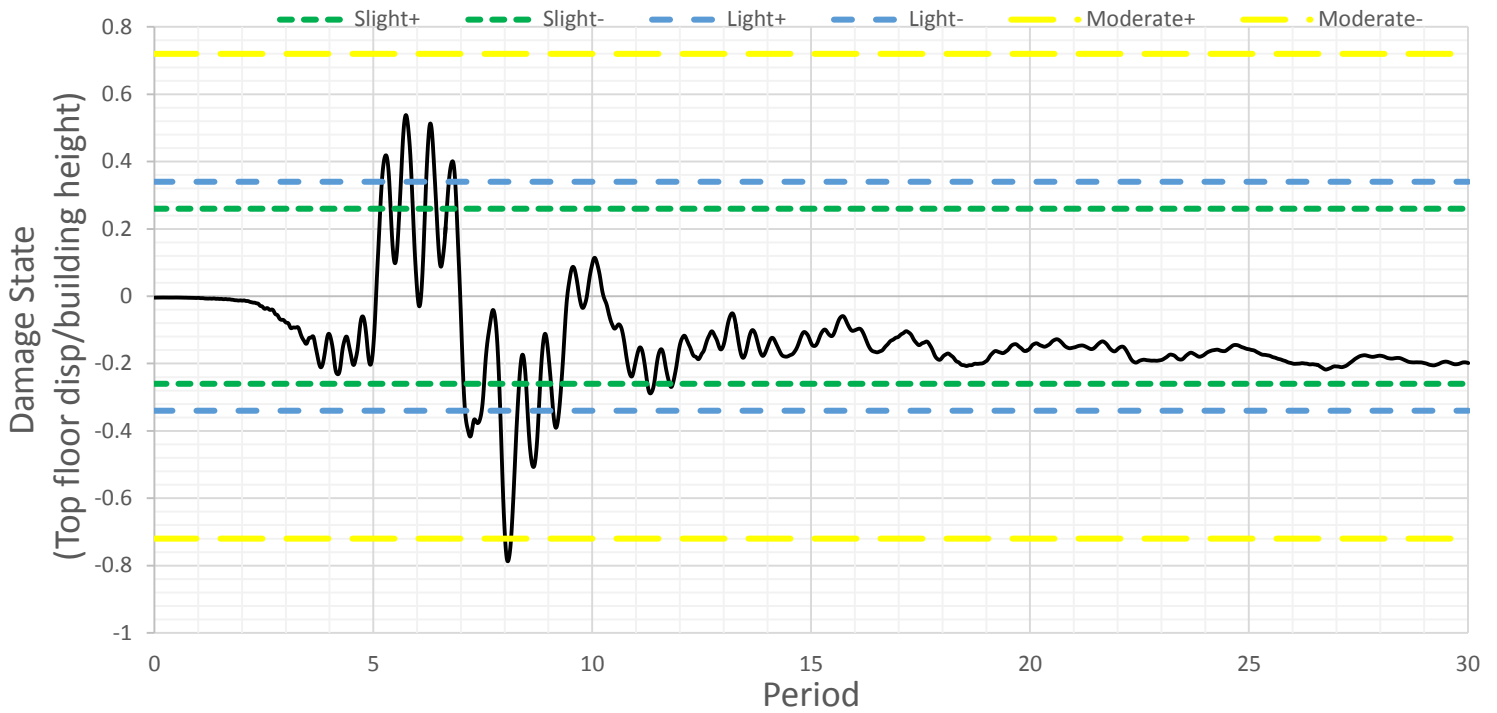


Figure 6.41. Figure showing ISD% and damage limit states (Shear walls) for recording station ACC

Record	Max. Roof Displacement	Drift (Disp./height)%	Damage State
ACC-DATA1	-0.19	-0.79	Moderate

Table 6.42. Table of Displacements and damage levels for recording station ACC



2. ACC-Data2 @Y-Dir.

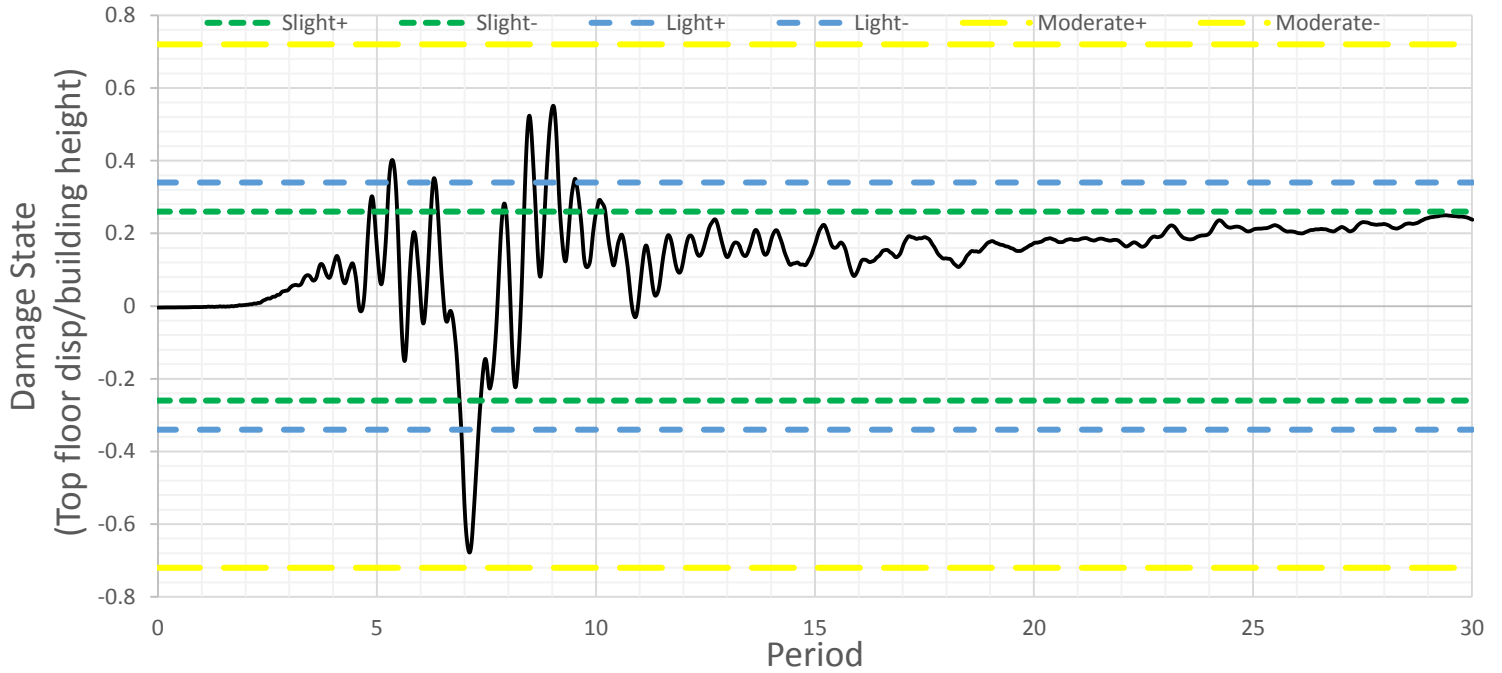


Figure 6.42. Figure showing ISD% and damage limit states (Shear walls) for recording station ACC

Record	Max. Roof Displacement	Drift (Disp./height)%	Damage State
ACC-DATA2	-0.16	-0.68	Light

Table 6.43. Table of Displacements and damage levels for recording station ACC



6.4.2.1.1. Record from AMT station

1. AMT-Data1 @Y-Dir.

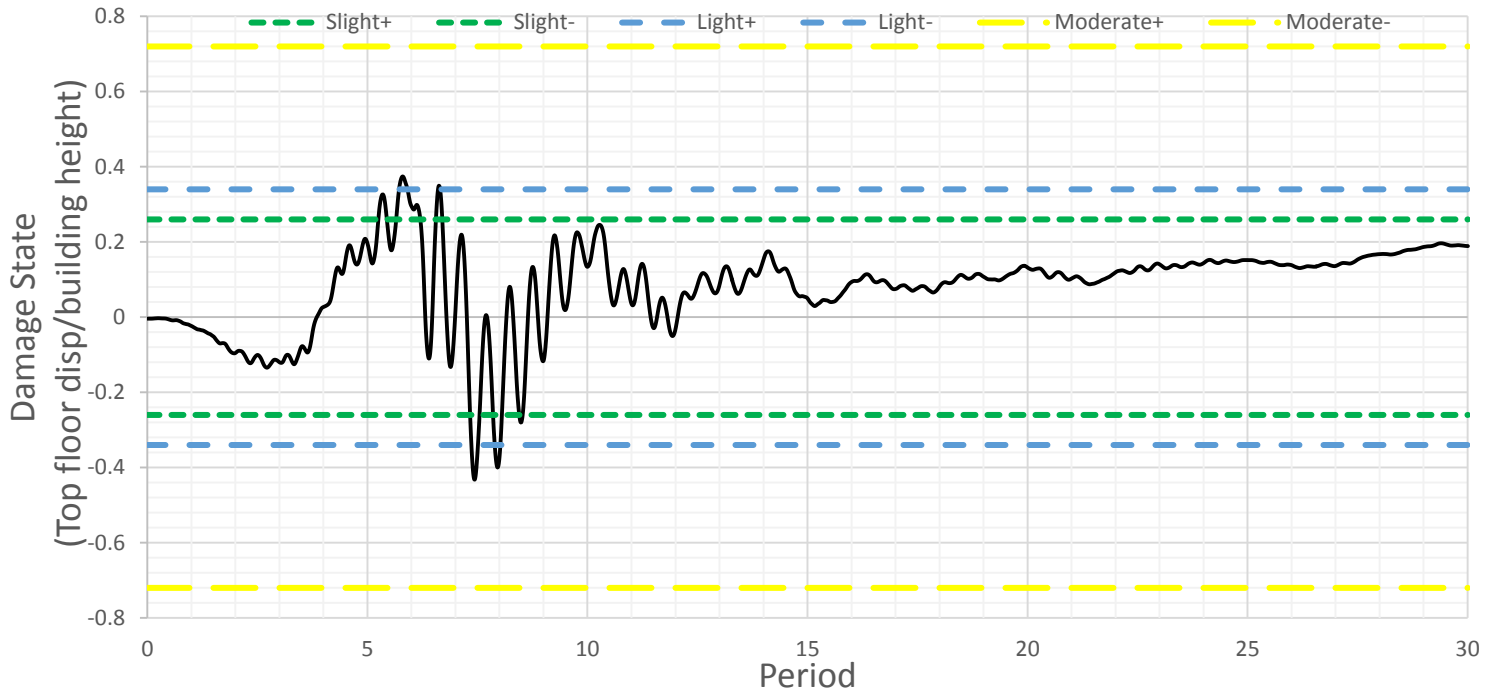


Figure 6.43. Figure showing ISD% and damage limit states (Shear walls) for recording station AMT

Record	Max. Roof Displacement	Drift (Disp./height)%	Damage State
AMT-DATA1	-0.10	-0.43	Light

Table 6.44. Table of Displacements and damage levels for recording station AMT



2. AMT-Data2 @Y-Dir.

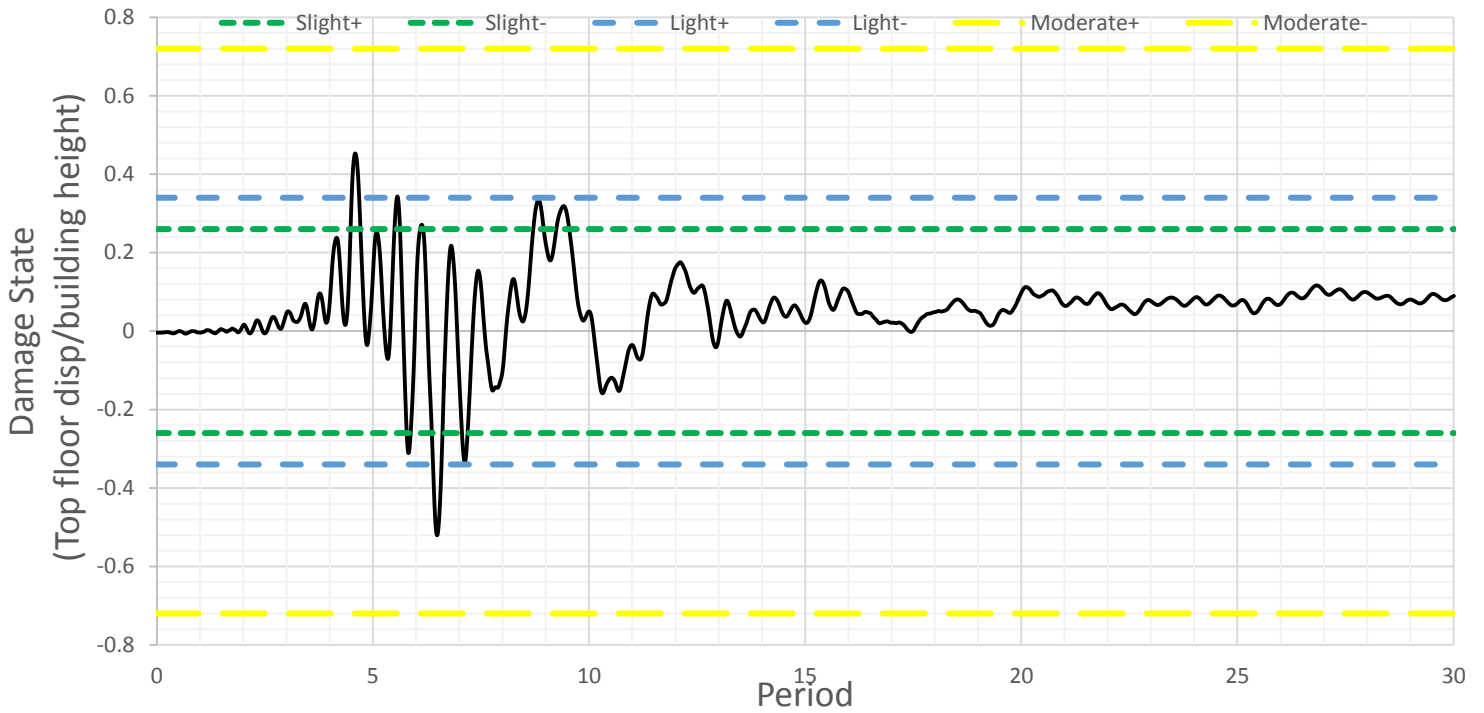


Figure 6.44. Figure showing ISD% and damage limit states (Shear walls) for recording station AMT

Record	Max. Roof Displacement	Drift (Disp./height)%	Damage State
AMT-DATA2	-0.12	-0.52	Light

Table 6.45. Table of Displacements and damage levels for recording station AMT



6.4.2.1.2. Record from T1201 station

1. T1201-Data1 @Y-Dir.

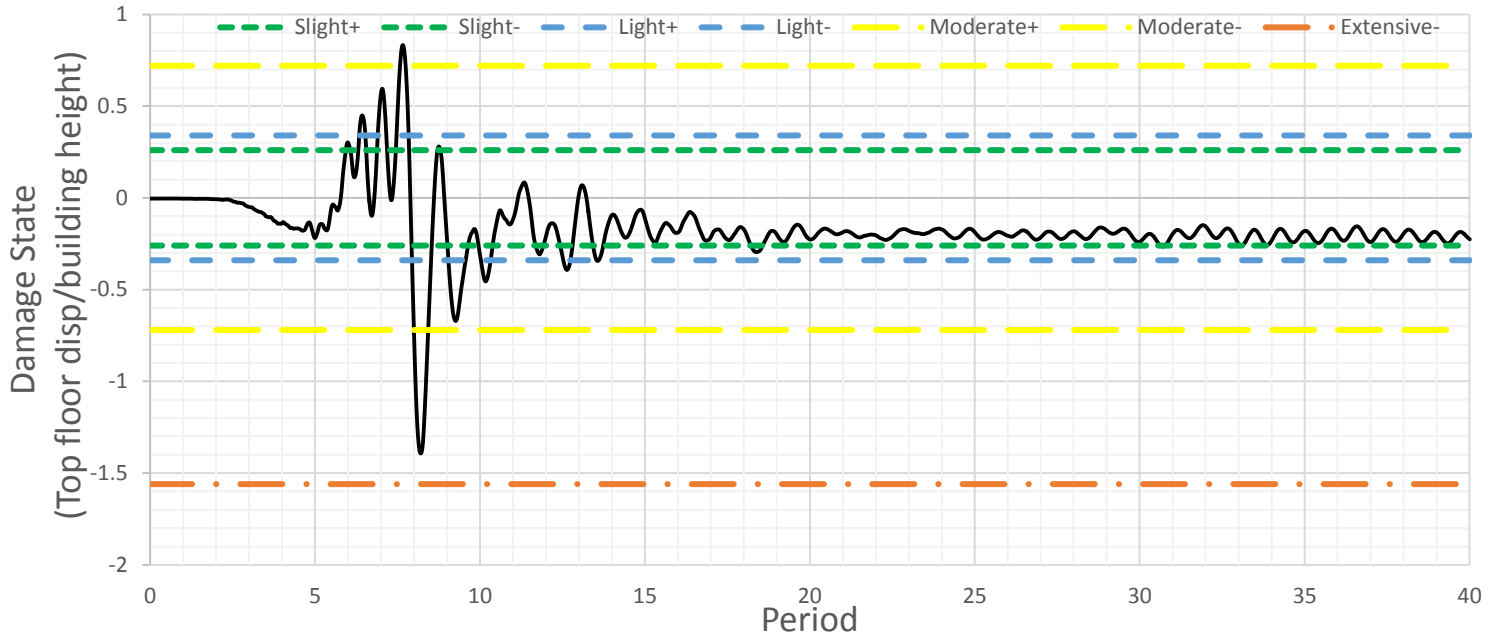


Figure 6.45. Figure showing ISD% and damage limit states (Shear walls) for recording station T1201

Record	Max. Roof Displacement	Drift (Disp./height)%	Damage State
T1201-DATA1	-0.33	-1.39	Extensive

Table 6.46. Table of Displacements and damage levels for recording station T1201



2. T1201-Data2 @Y-Dir.

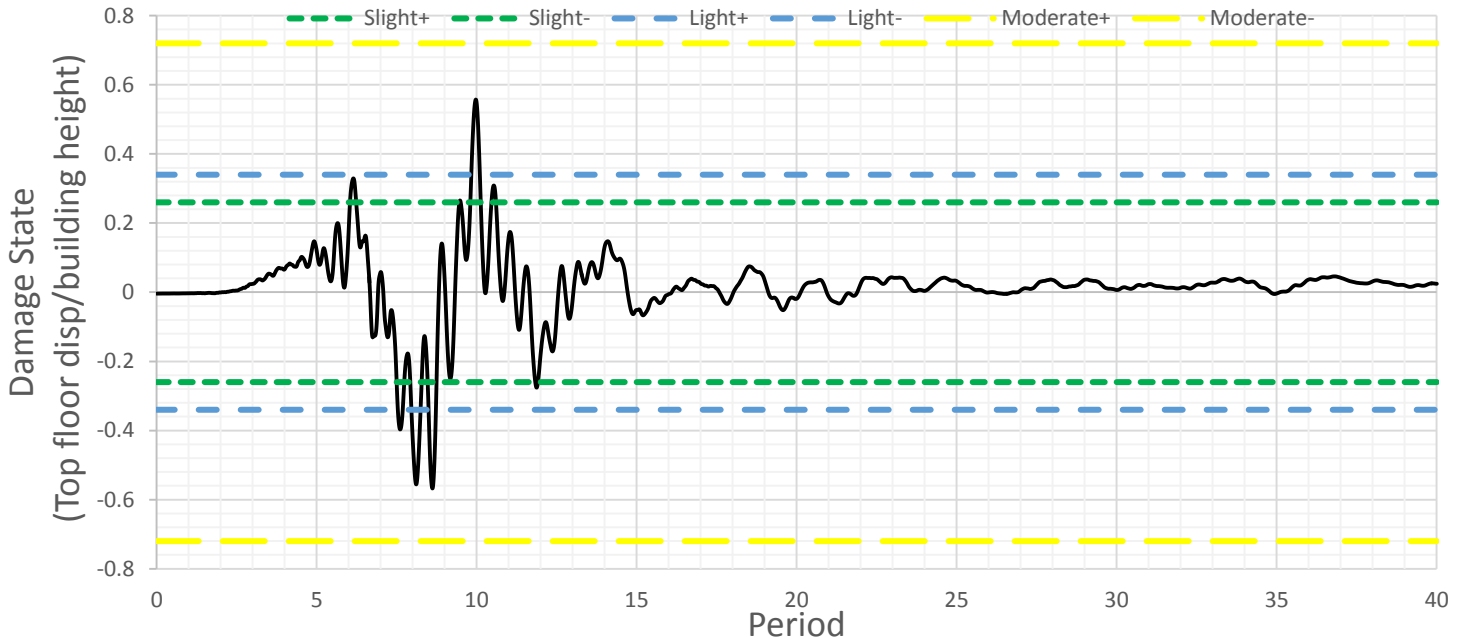


Figure 6.46. Figure showing ISD% and damage limit states (Shear walls) for recording station T1201

Record	Max. Roof Displacement	Drift (Disp./height)%	Damage State
T1201-DATA2	-0.14	-0.57	Light

Table 6.47. Table of Displacements and damage levels for recording station T1201



6.4.2.1.3. Record from NRC station

1. NRC-Data1 @Y-Dir.

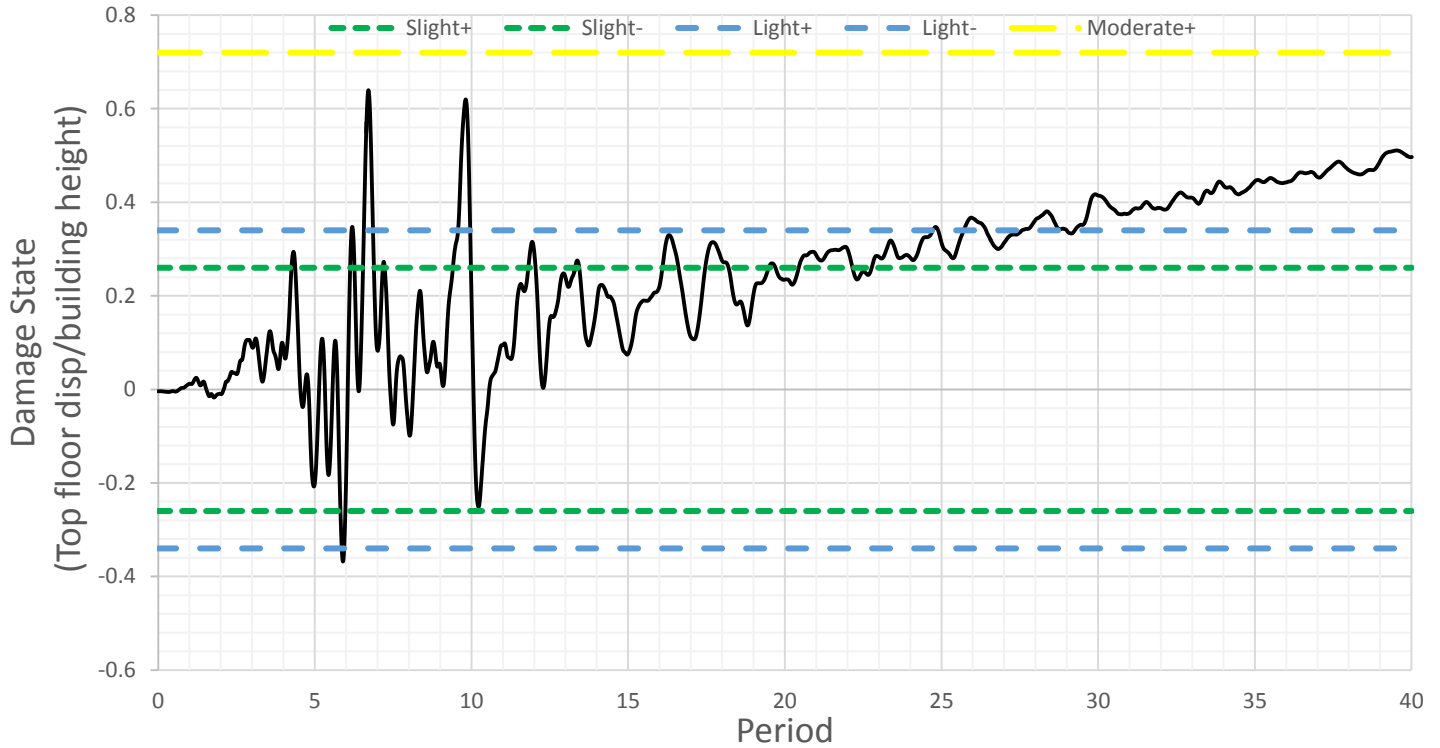


Figure 6.47. Figure showing ISD% and damage limit states (Shear walls) for recording station NRC

Record	Max. Roof Displacement	Drift (Disp./height)%	Damage State
NRC-DATA1	0.15	0.64	Light

Table 6.48. Table of Displacements and damage levels for recording station NRC



2. NRC-Data2 @Y-Dir.

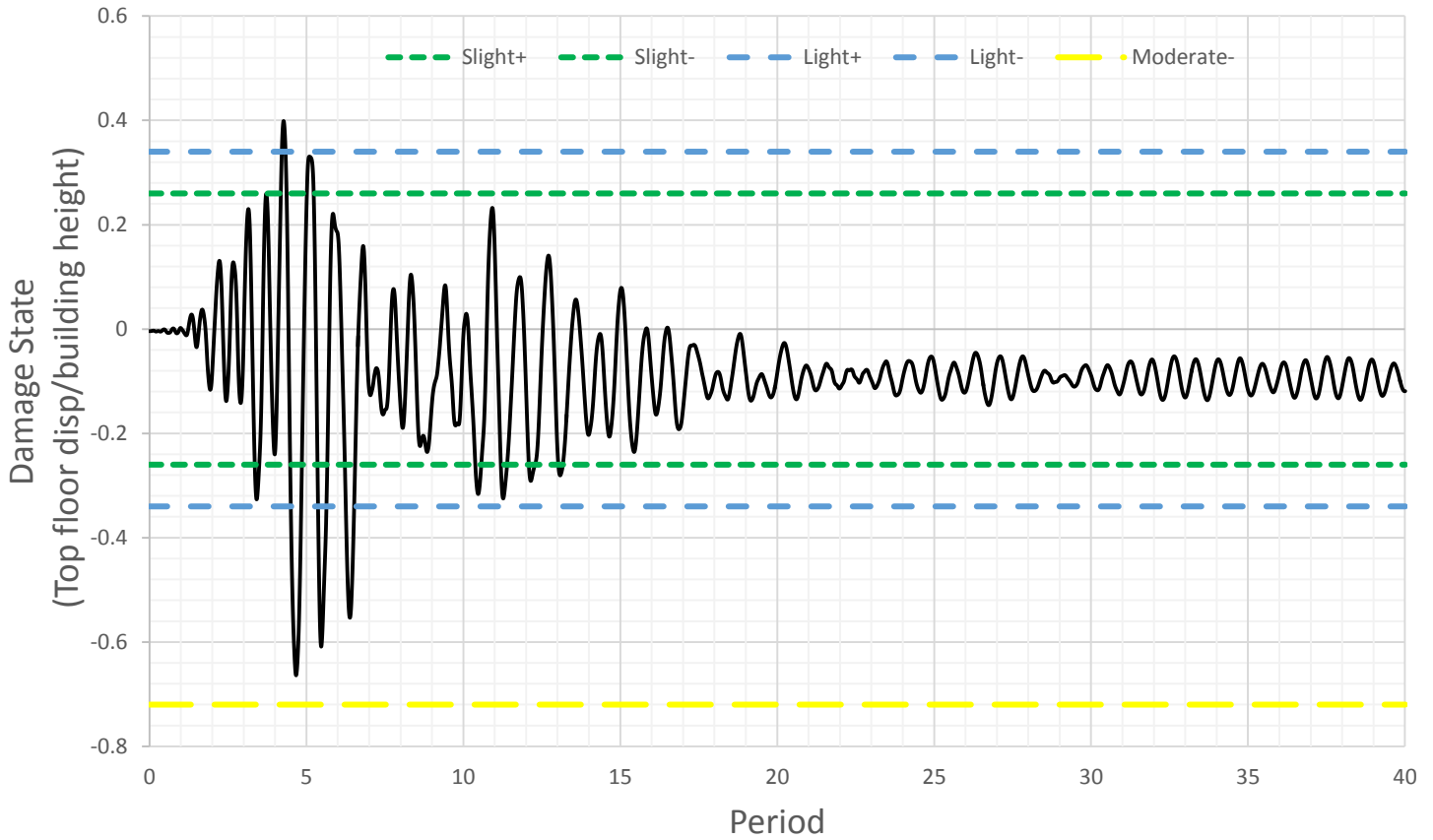


Figure 6.48. Figure showing ISD% and damage limit states (Shear walls) for recording station NRC

Record	Max. Roof Displacement	Drift (Disp./height)%	Damage State
NRC-DATA2	-0.16	-0.66	Moderate

Table 6.49. Table of Displacements and damage levels for recording station NRC

CHAPTER 7 SUMMARY AND CONCLUSIONS

7.1. Summary

The purpose of this paper is to investigate the seismic risk of an eight storey reinforced concrete building in Athens. The structure is exposed to a near field ground motions from Italian Aquila and Norcia earthquakes, due to the similarity in the geotectonic environment between Greece and Italy.

This investigation includes also the effect of the seismological parameters such as, moment magnitude, forward directivity, acceleration time history density and amplitude on the damage limit state reached by the building.

Furthermore, suggesting appropriate solution to mitigate the damage reached in practically applicable and economic approach.

As a first step, the structure was modelled using the building modeler of Seismostruct program, the height of each floor was taken approximately 3m. The dead loads are the own weight of the members, floor covering and wall loads, since the walls are divided into exterior and interior walls. The interior wall loads are distributed on the slabs while the exterior wall loads are uniformly distributed on the beams. All dead and live loads are transferred to the beams as distributed loads.

The Reinforced concrete building consists of beams which are simulated as T-sections in the interior spans while are considered as L-sections at the perimeter of the building. Shear walls, Beams and Columns are modeled as inelastic forced based plastic hinge elements (infrmFBPH), while the slabs are considered as rigid diaphragms.

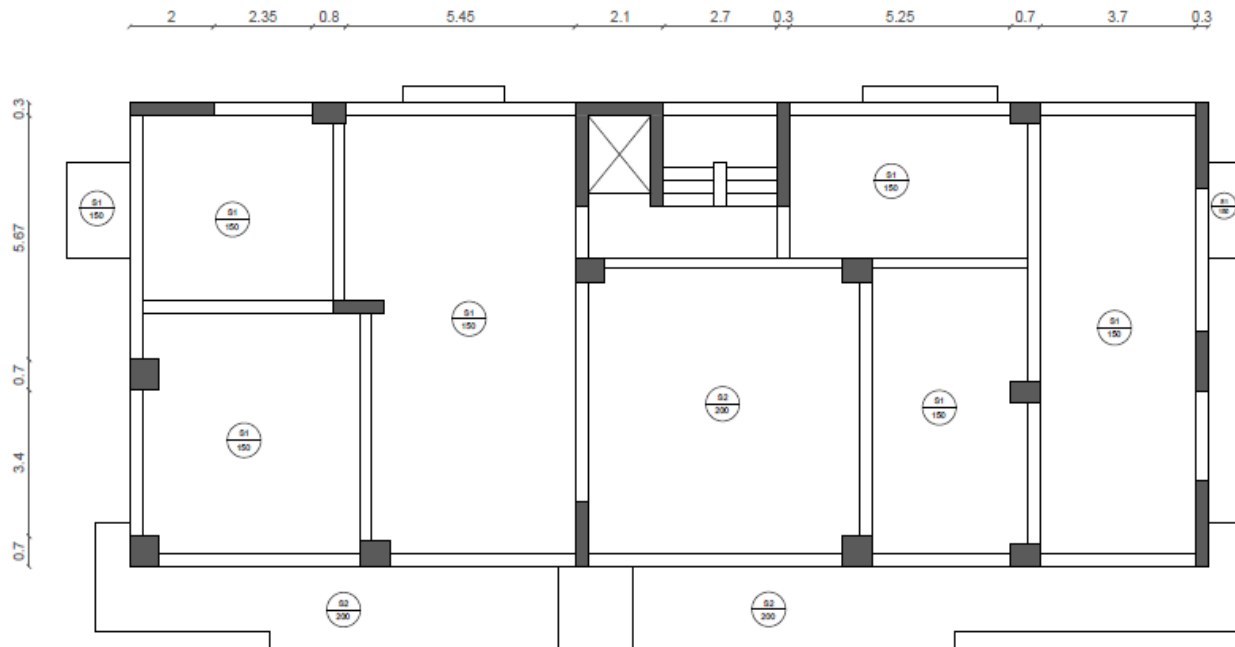


Figure 7.1. Figure showing the original building layout

In Seismostruct, in the calculation of eigenvalues analysis the efficient Lanczos algorithm [Hughes, 1987] is used for the evaluation of the structural natural frequencies and mode shapes, it is found that the fundamental period of the original building is 0.61sec.

Afterwards, a static non-linear pushover analysis is performed, in order to calculate the yield acceleration of the building (a_y) which is used later in picking up the suitable ground motion records expected to cause considerable damage.

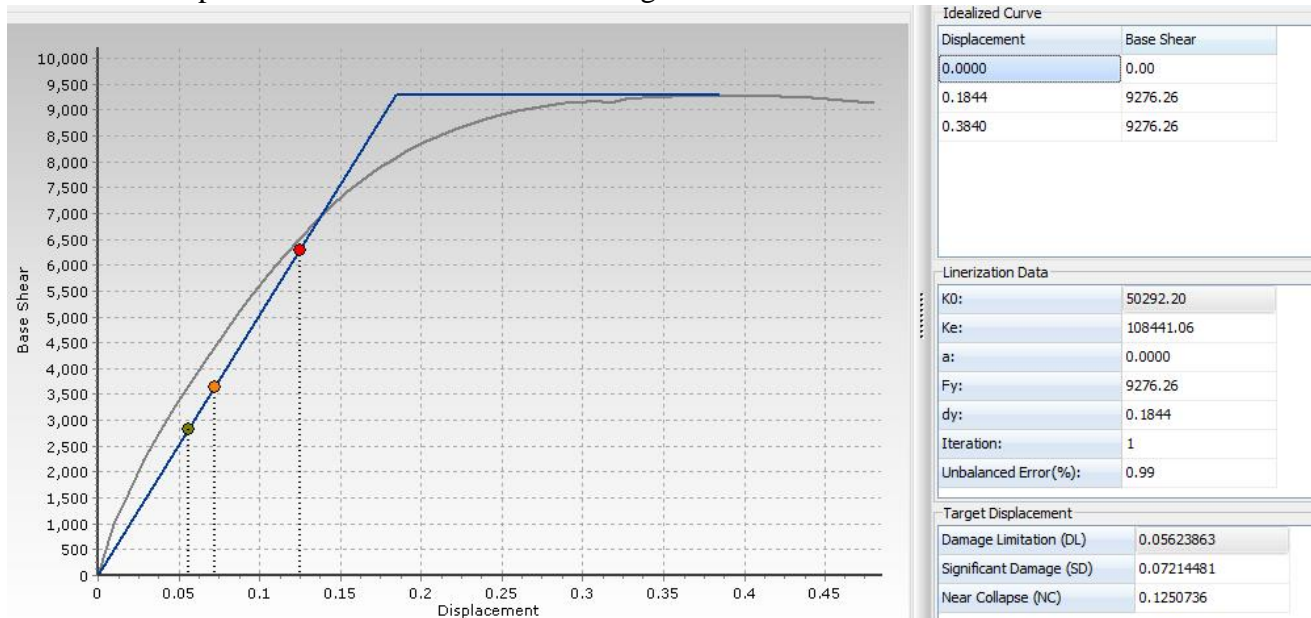


Figure 7.2 Pushover capacity curve in X-direction.

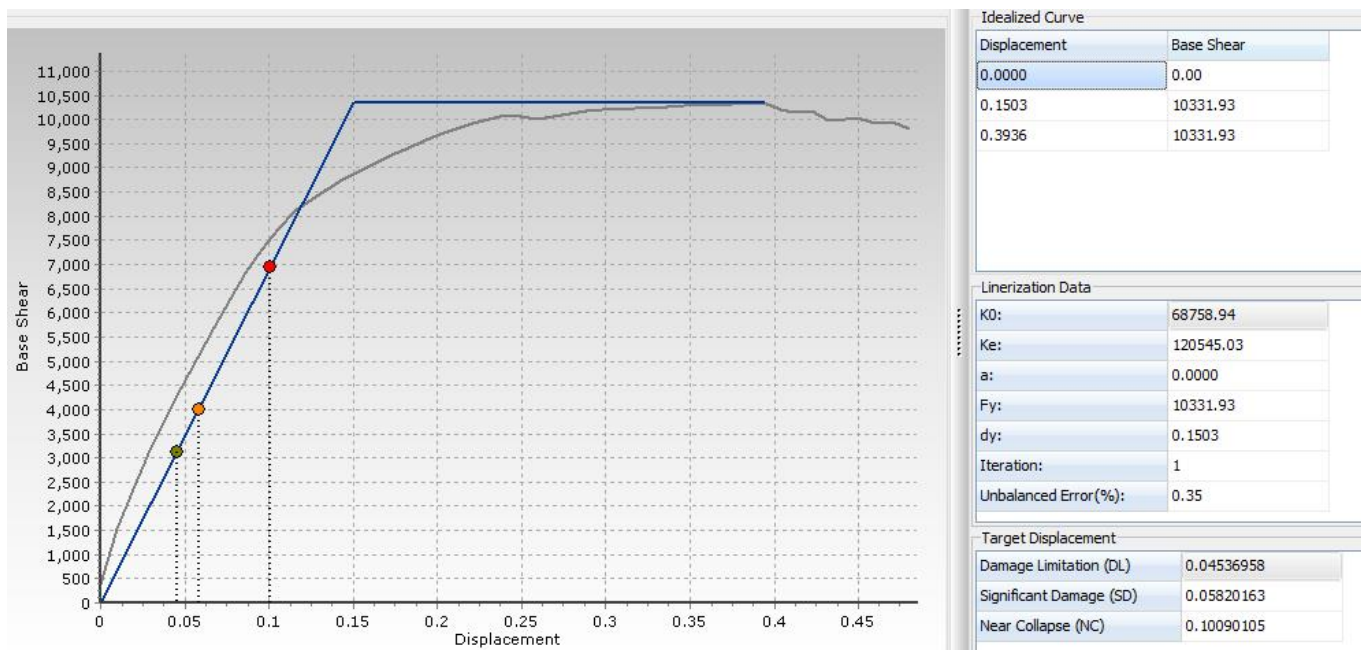


Figure 7.3 Pushover capacity curve in Y-direction.

As a result from the pushover analysis, the yielding force of the building in Y-direction was 10332 KN and since the mass of the building was 2709 tons, the yielding acceleration is evaluated approximately 3.8 m/sec².

Subsequently, a nonlinear inelastic dynamic time history analysis is performed, using a sample of 16 near fault ground motion records from Aquila and Norcia earthquakes in Italy, to obtain the displacement time history of each record, which will be used to determine the damage limit states achieved according to “T. Rossetto, A. Elnashai” vulnerability relationships.

ISD _{max%} (%) limits for HRC-scale				
HRC damage state	All	N-D MRF	Infilled MRF	Shear-walls
None	0.00	0.00	0.00	0.00
Slight	0.13	0.32	0.05	0.26
Light	0.19	0.43	0.08	0.34
Moderate	0.56	1.02	0.30	0.72
Extensive	1.63	2.41	1.15	1.54
Part. Coll.	3.34	4.27	2.80	2.56
Collapse	>4.78	>5.68	>4.36	>3.31

Table 7.1. Threshold values of ISD_{max%} defining the HRC-scale damage limit states for general RC structures (All), non-ductile MRF, Infilled MRF and shear wall structures.

Hence, the existing building was strengthened by a certain number of shear walls in order to make the ratio of shear wall in the one principal direction (Y) of the building to the floor area (A_w/A_f) about 3% in each floor to check the enhancement or improvement of the building seismic response taking into account reducing the existed shear walls and core reinforcement according to the new Chilean code assumptions and provisions.

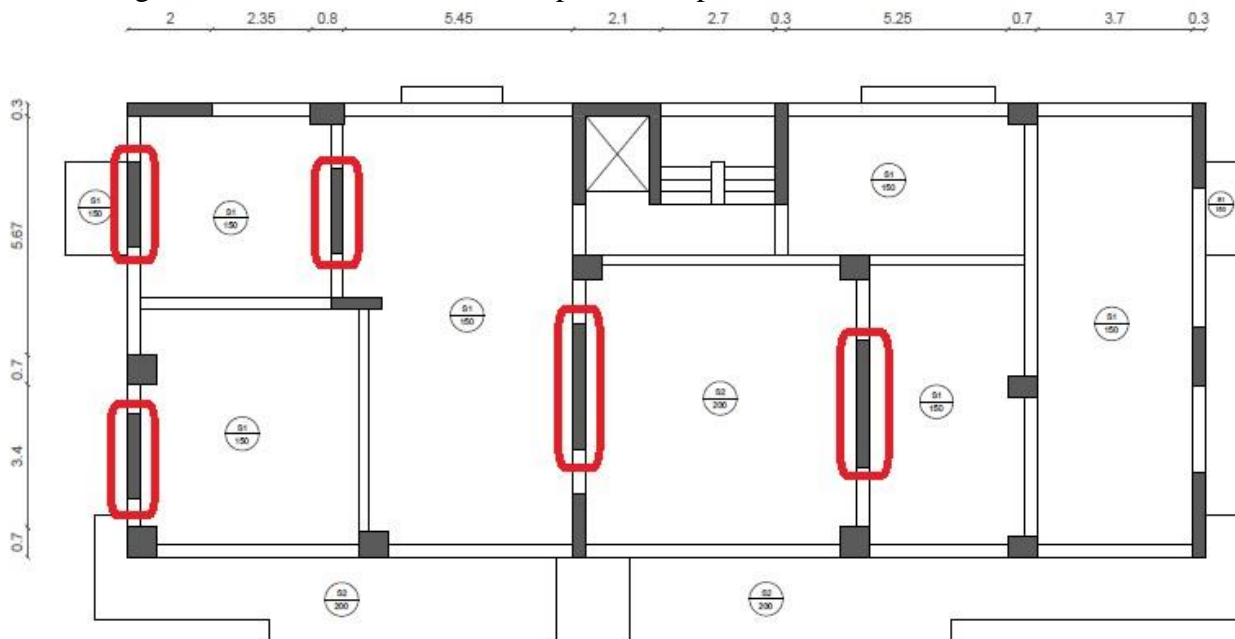


Figure 7.4 Plan View of the Strengthened Building

Five shear walls were introduced in the Y-direction with total area of 3.5 m², with minimum required light reinforcement in longitudinal and transversal directions which consists of 10mm diameter bars spaced at 20 cm ($\rho_v = 0.39\%$) and 8mm diameter bars spaced at 20 cm ($\rho_t = 0.25\%$), respectively. Horizontal web bars are typically placed outside of vertical bars and anchored at the wall edge with 90-degree hooks as shown in the figure below.

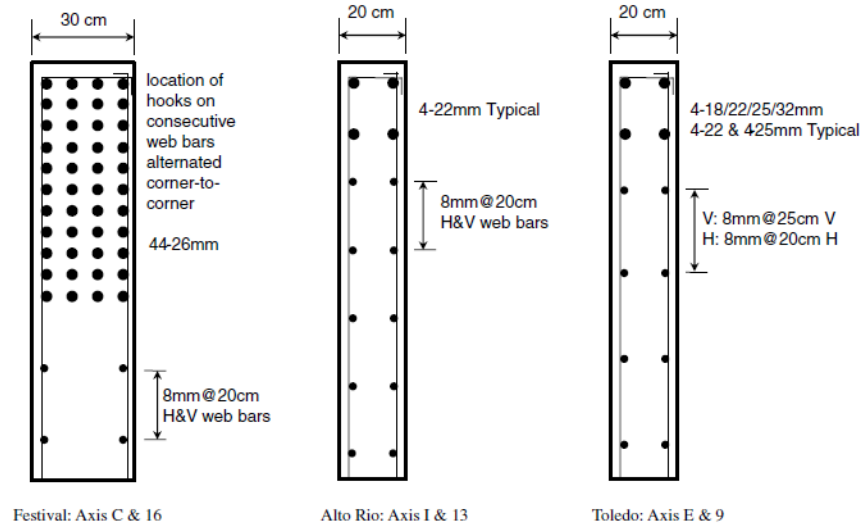


Figure 7.5 Typical wall boundaries: (a) Festival; (b) Alto Río; (c) Toledo.

For the strengthened building, the fundamental period of the structure from eigenvalue analysis is 0.56 sec.

Moreover, a static non-linear pushover analysis is performed, in order to compare the yield displacement after strengthening with the original one. The results have shown the displacement after strengthening is 6.4 cm while it was 15 cm for the original building.

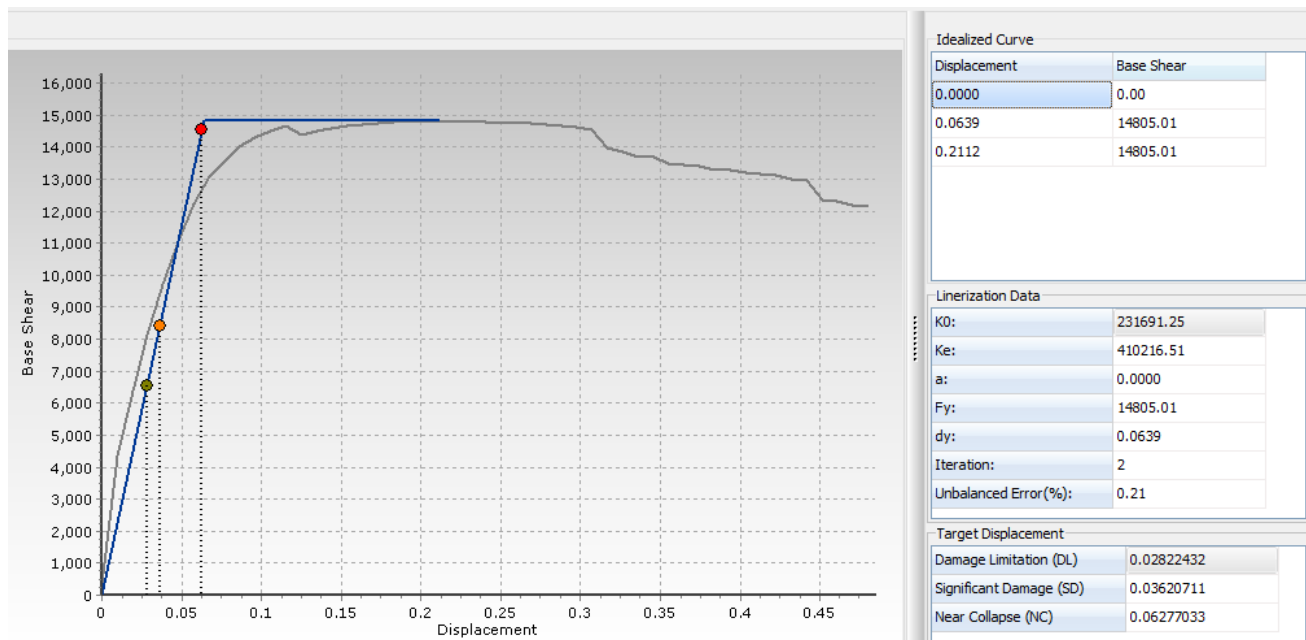


Figure 7.6 Pushover capacity curve in Y-direction.



7.2. Conclusions

Results of seismological studies have shown that Aquila and Norcia events were a normal faulting earthquakes (or dip-slip), where all the recording stations lie on the projection of rupture plan, which are characterized by forward directivity phenomenon.

Generally the intensity of the forward directivity velocity pulse depends on the rupture process and on the geometrical configuration of the fault and the site, the rupture propagation towards the site, the direction of slip on the fault is aligned with the site, the propagation velocity of rupture is almost as large as the shear wave velocity, and on the fraction of the fault rupture surface that lies between the hypocenter and the site. Also, the moment magnitude value is directly proportionally affecting the amplitude of the velocity pulse and consequently the damage limit states.

As noticed from the earthquake records, Although Aquila records have higher moment magnitude value of 6.3 Mw than most of Norcia records which are series of events of 6.0, 5.4, 5.9 and 6.5 Mw respectively, the damage limit state reached was Moderate, while the damage limit states reached by Norcia earthquake varied from Moderate to Extensive.

After investigating all the records, it was found that the moment magnitude value isn't the predominant affecting factor on the damage, other factors are more significant such as the acceleration time history density and amplitude.

At that point it is interesting to introduce an index of the velocity time history, the energy flux which is the time interval of the squared ground velocity. This index is a measure of the energy contained in the ground motion and in the case of a directivity velocity pulse this measure takes abruptly large values at the beginning of the ground motion duration.

And after reviewing all the previous results presented in chapter 6 we can conclude that:

1. The index of velocity time history (energy flux) is an appropriate measure of the intensity of the earthquake, as the records which reached the highest damage limit states as illustrated in tables 7.1 and 7.2 respectively, had the highest energy flux indices regardless the moment magnitude value and the acceleration time history amplitude values as shown in the following figures.

Aquila in X Direction for original building			
Record	Disp. (m)	Drift (Disp./Height)%	Damage State
	Original	Original	Original
AQA_DATA1	0.11	0.47	Moderate
AQG_DATA1	-0.16	-0.67	Moderate
AQK_DATA1	-0.21	-0.89	Moderate
AQV_DATA1	-0.13	-0.53	Moderate
AQA_DATA2	0.12	0.49	Moderate
AQG_DATA2	-0.15	-0.64	Moderate
AQK_DATA2	-0.20	-0.84	Moderate
AQV_DATA2	-0.18	-0.77	Moderate

Norcia in X Direction for original building			
Record	Disp. (m)	Drift (Disp./Height)%	Damage State
	Original	Original	Original
ACC_DATA1	-0.28	-1.15	Extensive
AMT_DATA1	-0.12	-0.52	Moderate
T1201_DATA1	-0.33	-1.38	Extensive
NRC_DATA1	0.34	1.41	Extensive
ACC_DATA2	0.22	0.90	Moderate
AMT_DATA2	0.09	0.37	Moderate
T1201_DATA2	-0.17	-0.70	Moderate
NRC_DATA2	-0.31	-1.28	Extensive

Table 7.2 Aquila earthquake damage limit states

Table 7.3 Norcia earthquake damage limit states

As observed in the below figures all the Aquila records have moderate damage state, with energy flux and acceleration amplitude ranges between 400~500 cm²/s and 300~400 cm/s² respectively, except for AQK that has energy flux of 1400 cm²/s, which is the station with the strongest pulse like signal in FN direction as it's the more far station form the epicenter than the others.

While for Norcia records the damage limit states reached were moderate and extensive, As the energy flux for the moderate damage state ranges between 400~500 cm²/s, and for the extensive damage state ranges between 1500~3000 cm²/s. All the records have approximately the same acceleration amplitude of 400 cm/s².

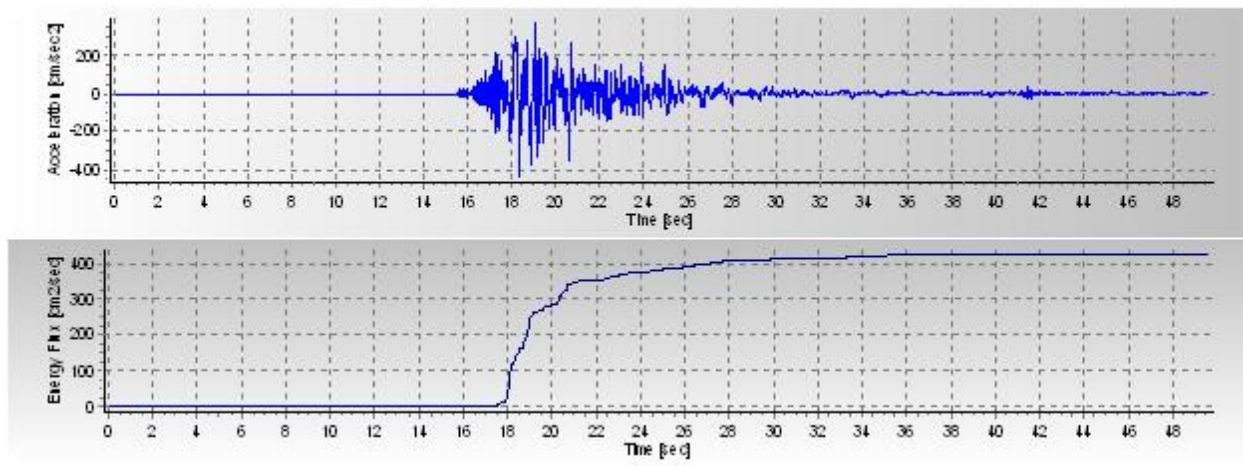


Figure 7.7 Acceleration time history and energy flux for Aquila AQA-DATA 1 record (Moderate).

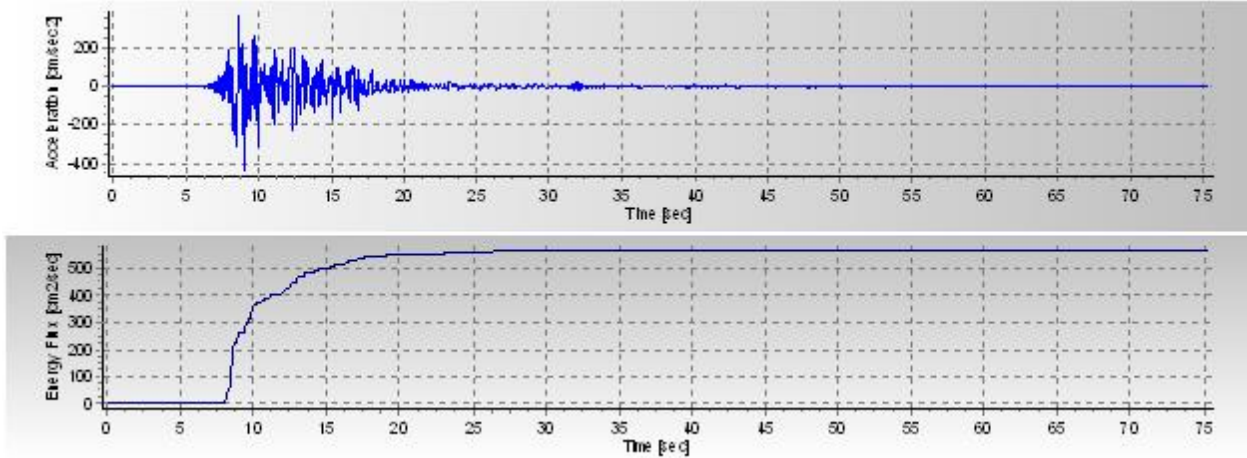


Figure 7.8 Acceleration time history and energy flux for Aquila AQG-DATA 1 record (Moderate).

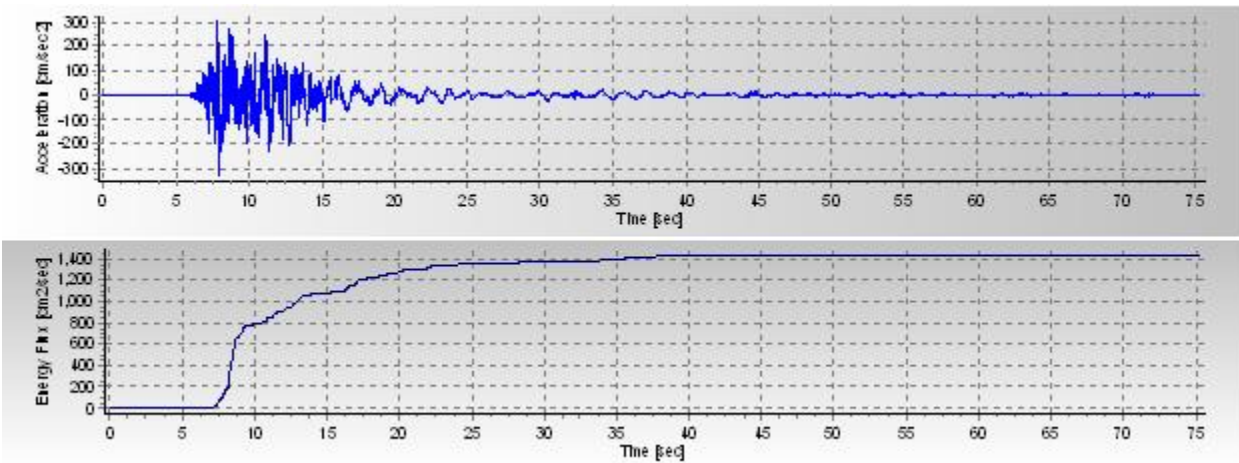


Figure 7.9 Acceleration time history and energy flux for Aquila AQK-DATA 1 record (Moderate).

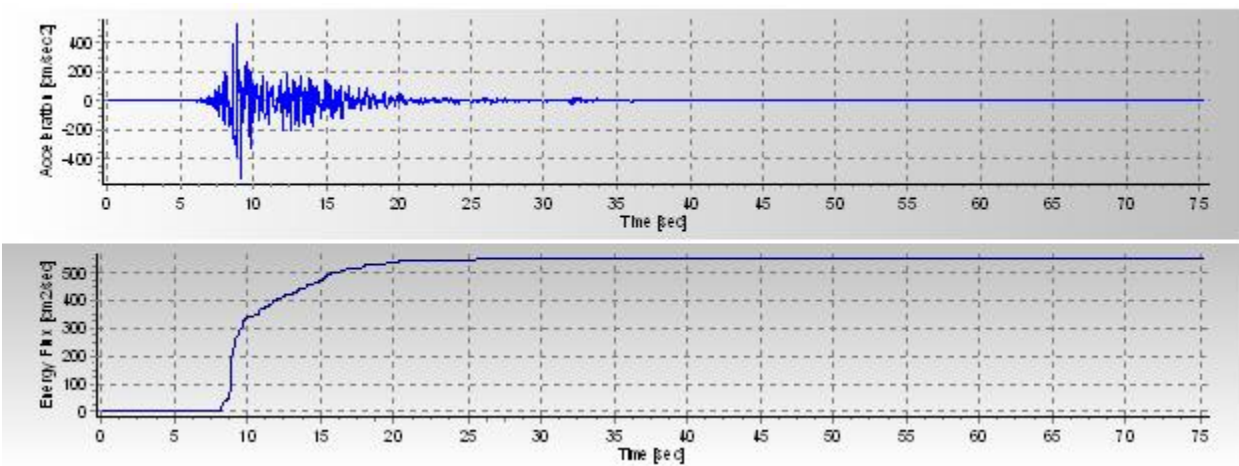


Figure 7.10 Acceleration time history and energy flux for Aquila AQV-DATA 1 record (Moderate).

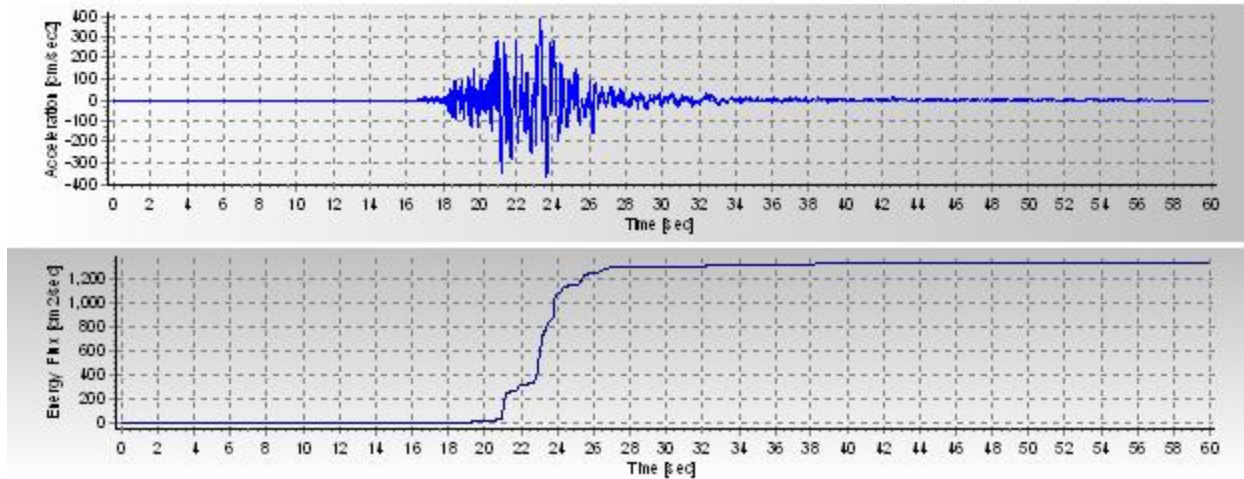


Figure 7.11 Acceleration time history and energy flux for Norcia ACC-DATA 1 record (Extensive).

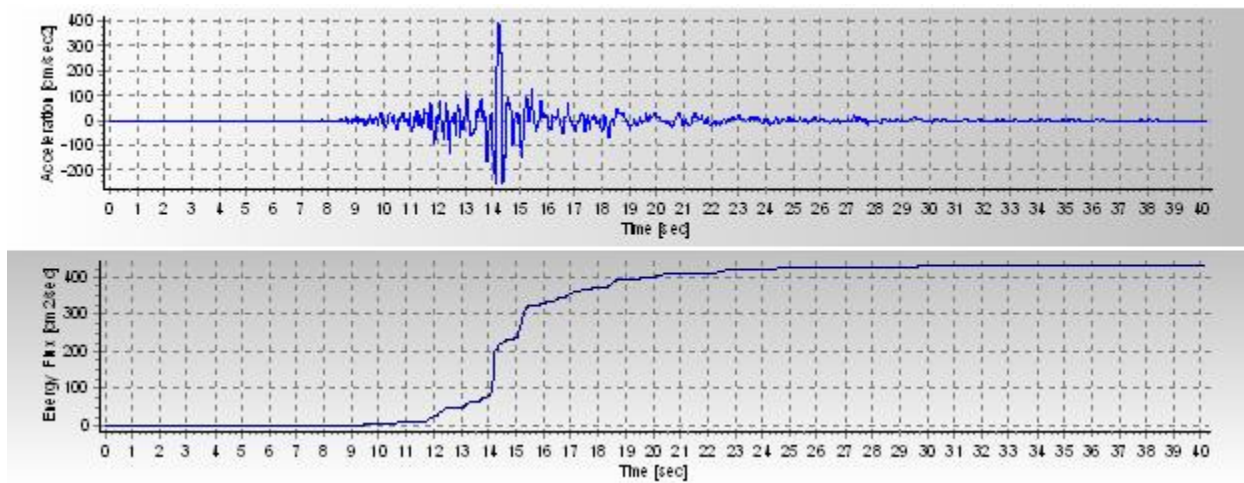


Figure 7.12 Acceleration time history and energy flux for Norcia AMT-DATA 1 record (Moderate).

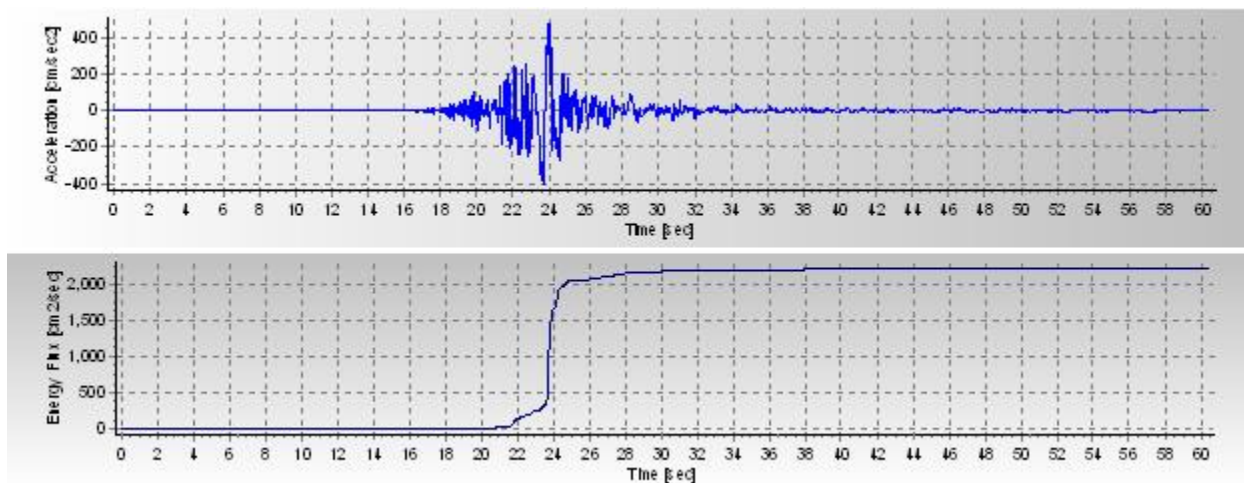


Figure 7.13 Acceleration time history and energy flux for Norcia T1201-DATA 1 record (Extensive).

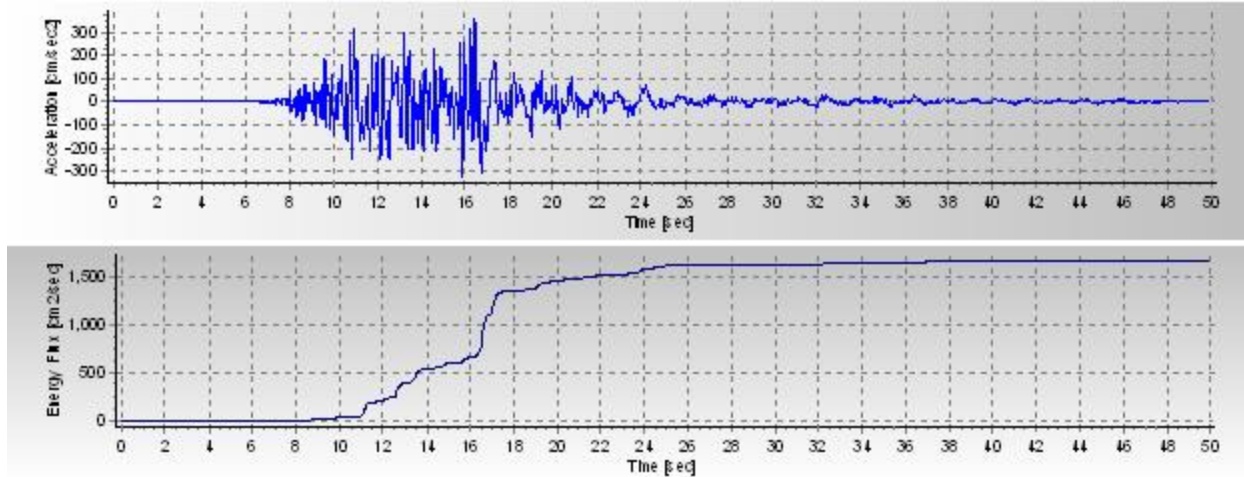


Figure 7.14 Acceleration time history and energy flux for Norcia NRC-DATA 1 record (Extensive).

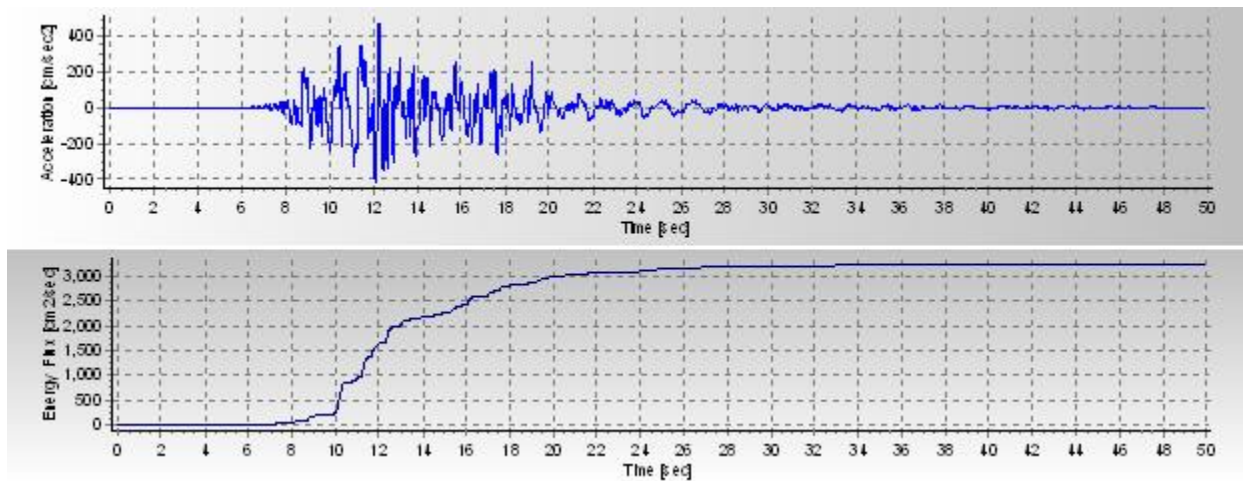


Figure 7.15 Acceleration time history and energy flux for Norcia NRC-DATA 2 record (Extensive).

2. After strengthening the building in Y-Direction according to the new Chilean code of practice provisions (NCh433.Of96; INN 1996) with the minimum required longitudinal and transversal reinforcement which are 10mm diameter bars spaced at 20 cm ($\rho_v = 0.39\%$) and 8mm diameter bars spaced at 20 cm ($\rho_t = 0.25\%$) respectively, and making the ratio of shear walls in that direction (Y) of the building to the floor area (A_w/A_f) about 3% in each floor, and exposing the building to the same earthquake records previously mentioned performing nonlinear inelastic dynamic time history analyses, it is found out that the building behavior in terms of damage limit states is improved as illustrated in the following tables 7.3 and 7.4 respectively. For Aquila records the behavior is improved from moderate to light damage state, and for Norcia records the behavior is improved from extensive-moderate to moderate-light damage states. After the study above this practice is considered to be an appropriate solution for resisting earthquake loads as it is economic, safe and effective solution.



Aquila in Y Direction for original building & strengthened building							
Record	Displacement(m)		Drift (Disp./height)%		Damage State		Percentage of improvement (%)
	Original	Strengthened	Original	Strengthened	Original	Strengthened	
AQA_DATA1	-0.11	-0.09	-0.46	-0.39	Moderate	Light	19.7%
AQG_DATA1	-0.17	0.09	-0.72	0.38	Moderate	Light	88.6%
AQK_DATA1	-0.20	-0.15	-0.84	-0.62	Moderate	Moderate	35.5%
AQV_DATA1	-0.11	-0.12	-0.44	-0.48	Moderate	Light	8.5%
AQA_DATA2	-0.14	-0.08	-0.58	-0.34	Moderate	Light	74.3%
AQG_DATA2	-0.16	-0.06	-0.68	-0.24	Moderate	Slight	181.8%
AQK_DATA2	-0.16	-0.10	-0.66	-0.43	Moderate	Light	52.3%
AQV_DATA2	-0.20	-0.11	-0.85	-0.47	Moderate	Light	81.2 %

Table 7.4 Aquila earthquake damage limit states & percentage of improvement for original and strengthened building.

Norcia in Y Direction for original building & strengthened building							
Record	Displacement(m)		Drift (Disp./height)%		Damage State		Percentage of improvement (%)
	Original	Strengthened	Original	Strengthened	Original	Strengthened	
ACC_DATA1	-0.28	-0.19	-1.15	-0.79	Extensive	Moderate	46.3%
AMT_DATA1	-0.14	-0.10	-0.57	-0.43	Moderate	Light	32.2%
T1201_DATA1	-0.34	-0.33	-1.43	-1.39	Extensive	Extensive	2.3%
NRC_DATA1	-0.24	0.15	-0.99	0.64	Extensive	Moderate	54.6 %
ACC_DATA2	-0.17	-0.16	-0.71	-0.68	Moderate	Moderate	4.5%
AMT_DATA2	-0.12	-0.12	-0.48	-0.52	Moderate	Light	7.6%
T1201_DATA2	0.18	-0.14	0.76	-0.57	Moderate	Light	34.2%
NRC_DATA2	-0.27	-0.16	-1.11	-0.66	Extensive	Moderate	67.9%

Table 7.5 Norcia earthquake damage limit states & percentage of improvement for original and strengthened building.

As observed in the previous tables, the behavior improved for most of the records except for (T1201_DATA1) and (ACC_DATA2) records, as the predominant pulse period is almost twice the structure elastic period. Therefore when the structure behaves inelastically, its period gets closer to the pulse period and a high response amplification is obtained “resonance might occur” as illustrated in the following figures.

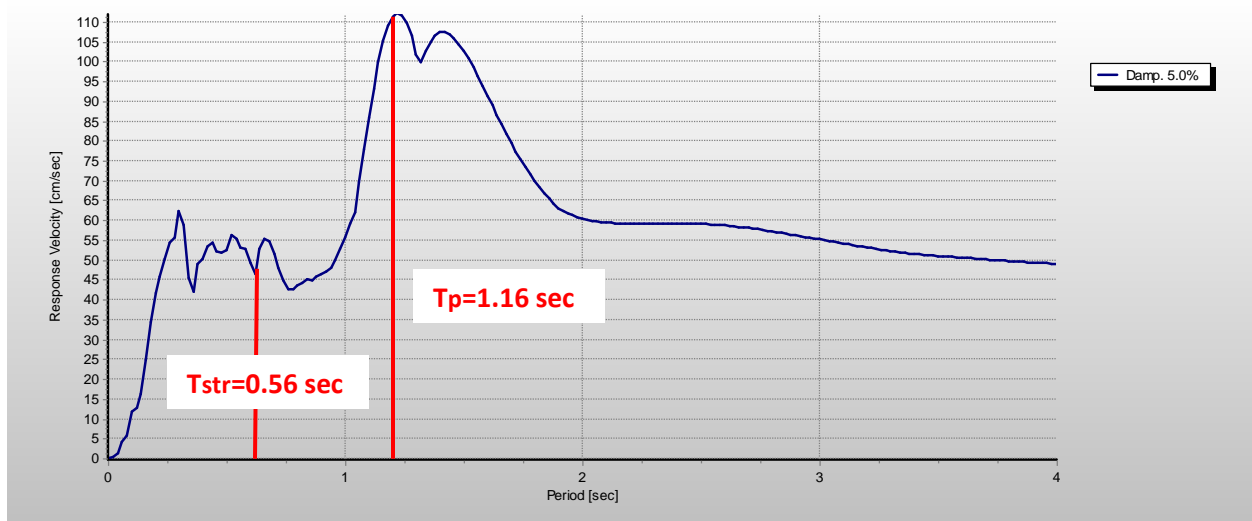


Figure 7.16 Velocity response spectrum for ACC-DATA2

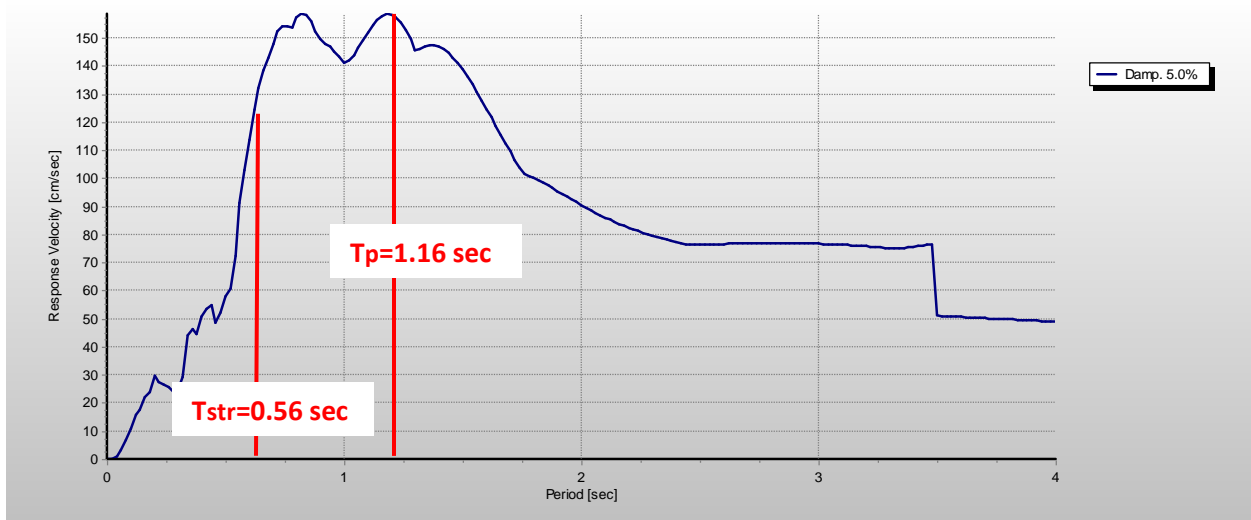


Figure 7.17 Velocity response spectrum for T1201-DATA1



REFERENCES

- 1) Effects of Near-Field Ground Motion on Building Structures, Babak Alavi and Helmut Krawinkler, Stanford University.
- 2) Relation of Pulse Period with Near-Fault Strong Motion Parameters, V. Kardoutsou, P. Mimoglou, I. Taflampas and I. N. Psycharis.
- 3) Response of Structures to Near-Fault Ground Motion, A. Ghobarah.
- 4) Identification of near-fault earthquake record characteristics, Ch. A. Maniatakis, I.M. Taflampas and C.C. Spyrakos, 2008.
- 5) Derivation of vulnerability functions for European-type RC structures based on observational data, T. Rossetto, A. Elnashai.
- 6) Fundamentals of Earthquake Engineering From Source to Fragility, Amr S. Elnashai.
- 7) Near-source seismic demand and pulse-like records: A discussion for L'Aquila earthquake, Eugenio Chioccarelli and Iunio Iervolino.
- 8) Preliminary study on strong motion data of the 2016 central Italy seismic sequence v6, Iunio Iervolino, Georgios Baltzopoulos, Eugenio Chioccarelli, Akiko Suzuki.
- 9) Second summary report on the ML 6.0 Amatrice earthquake of august 24, 2016 (central Italy), INGV Working Group on the Amatrice Earthquake.
- 10) Summary report on the 30 October, 2016 earthquake in central Italy Mw 6.5, INGV Working Group on Central Italy Earthquake.
- 11) Damage and Implications for Seismic Design of RC Structural Wall Buildings, John W. Wallace, Leonardo M. Massone, Patricio Bonelli, Jeff Dragovich, René Lagos, Carl Lüders, and Jack Moehle.
- 12) The Collapse of the Alto Río Building during the 27 February 2010 Maule, Chile Earthquake, Cheng Song, Santiago Pujol, and Andrés Lepage.
- 13) Response of Reinforced Concrete Buildings in Concepción during the Maule Earthquake, Benjamín Westenenk, Juan Carlos de la Llera, Juan José Besa, Rosita Jünemann, Jack Moehle, Carl Lüders, José Antonio Inaudi, Kenneth J. Elwood, and Shyh-Jiann Hwang.
- 14) Seismic Design and Construction Practices for RC Structural Wall Buildings, Leonardo M. Massone, Patricio Bonelli, René Lagos, Carl Lüders, Jack Moehle, and John W. Wallace.
- 15) Damage Assessment and Seismic Intensity Analysis of the 2010 (Mw 8.8) Maule Earthquake, Maximiliano Astroza, Sergio Ruiz, and Rodrigo Astroza.
- 16) Comparison of U.S. and Chilean Building Code Requirements and Seismic Design Practice 1985–2010, NEHRP Consultants Joint Venture, A partnership of the Applied Technology Council and the Consortium of Universities for Research in Earthquake Engineering.